THE FABRICATION AND MICROSTRUCTURAL EVOLUTION, AT ELEVATED TEMPERATURES, OF SYALON CERAMICS.

by

S M WINDER

A thesis submitted for the degree of PhD to

The University of Warwick

Department of Physics

September 1985

CONTENTS

Contents contd.

Contents contd.

Contents contd.

DECLARATION

This dissertation is submitted to the University of Warwick in support of my application for admission to the degree of Doctor of Philosophy. It is an account of my work performed principally in the Department of Physics, University of Warwick, during the period October 1980 to November 1983. All of the work reported is a result of my own independent research, under the general supervision of M H Lewis, unless specifically stated otherwise. No part of this thesis has been previously submitted to this or any other university in a degree thesis.

J. Winder

SEPTEMBER 1985

S M WINDER

ACKNOWLEDGEMENT

I acknowledge the help, advice and guidance provided by Dr. M H Lewis, G Smith and S York of the Ceramics Research Group, University of Warwick. I am also grateful to the staff in the workshops and laboratories of the Department of Physics, for technical support and use of facilities.

I wish to thank Dr. A Nicholls of the Department of Metallurgy and Materials, University of Birmingham, for the use of the EELS analysis system, and M Thornton of Alcan Research Laboratories, Banbury, for use of the image processor.

Many thanks are due to Dr. E G Butler, Dr. R J Lumby and Dr. A Szweda of Lucas-Cookson-Syalon Ltd., for provision of material and financial support.

Finally, I would like to thank Miss T A Culley for help in preparation of this thesis and moral support during the past two years.

TABLES

Tables contd.

FIGURES

Figures contd.

Figures contd.

Figures contd.

ABSTRACT

A number of experimental grade Syalon Ceramics, pressureless sintered materials prepared from the system Y-Si-Al-O-N, were prepared at Lucas-Cookson Syalon Ltd. (Birmingham). Different series of ceramics were composed with α-Si_3N_4 powder provided by different manufacturers, and each series contained alloys of varying (effective) AlN content.

Microstructural characterisation of selected alloys was completed using the techniques of optical microscopy, x-ray diffractometry, electron microscopy with x-ray microanalysis, and energy loss spectroscopy. For 'as-sintered' ceramics, the results indicate a trend in microstructural parameters with (effective) AlN content, such that the mean Al_2O_3 substitution level in the β' $Si_{6-z}Al_zO_zN_{8-z}$ (major) phase, and the N/O ratio of the inter-β' (minor) glassy phase, both increase with increased AlN addition. A linear relationship between increasing (Y + O) content in the 'as mixed' alloy composition and increasing glass volume fraction in the microstructure, formed under given sintering conditions, was demonstrated.

Passive oxidation occurred during heat-treatment in air, in the temperature range 1100-1500°C, and formation of β-$Y_2Si_2O_7$ crystals on the scale surface was noted.

Two crystalline phases, $Y_3Al_5O_{12}$ (YAG) and α-$Y_2Si_2O_7$ (yttrium disilicate), were produced during devitrification of the intergranular phase, in the temperature interval 1100-1500°C. The volume ratio $Y_3Al_5O_{12}$: $Y_2Si_2O_7$, in the heat-treated microstructures, was found to increase as heat-treatment temperature and glass nitrogen content increased.

Creep tests were performed in the temperature range 1100-1300°C and enhanced creep resistance was demonstrated for materials of lower intergranular phase content, in which nitrogen levels are higher. Morphological changes occurring in the sub-surface and bulk of the ceramics, due to oxidation and crystallisation reactions, were found to cause a time dependent transient in creep behaviour.

CHAPTER 1.- The development of Syalon Ceramics

The technological advance of recent history has generated a requirement for improved materials performance to enable full exploitation of the new hardware both under development and already available. The Syalon Ceramic research programme was created to develop the potential of easily fabricated silicon nitride-based ceramic alloys to meet the demands of elevated temperature engineering application. This thesis is based on some of the work completed in the Syalon Ceramic programme.

In this chapter the demand for new materials will be demonstrated and early candidate ceramics identified. The suitability of silicon nitride-based ceramics for use at elevated temperatures and the resulting development of Syalon Ceramics will then be discussed. Finally, the objectives of the work reported in this thesis will be presented.

1.1 Ceramics for engineering application at elevated temperature

1.1.1 The demand for ceramics

Four basic demand areas have been identified[1] where increased performance could be gained by substitution of ceramic components for traditional ones - see Figure 1.1. The case for such substitution in some of these applications will now be discussed.

(a) Gas turbine components

Rotors produced from nickel-based 'superalloys' have been highly developed for use in gas turbine engines for aircraft, but the stage has now been reached where further developments with these materials can only yield small performance improvements. An increase in operating temperature of gas turbines is expected to increase performance and efficiency thereby decreasing fuel costs and pollution. Various components within gas turbines need to be replaced to obtain a significant increase in operating temperature and various ceramic materials have been proposed as possible contenders. Attractive properties exhibited by ceramics are:-

High resistance to thermal shocking,
High creep resistance at elevated temperatures,
High oxidation and corrosion resistance,
High abrasion resistance,

Low density,

Low thermal expansion coefficient.

As well as the obvious benefits derived from the use of ceramic components, it should also be noted that their use would liberate turbine manufacturers from the constraints of using strategically sensitive materials (eg. Ni, Cr, Co) since ceramic component elements are generally available (eg. Si, Al, O, N, C). Government sponsored work in the U.S.A. has indicated that ceramic-based Advanced Gas Turbine Engines (A.G.T's) could prove to be high power, high efficiency, low weight units for powering automobiles and trucks[1], and Daimler-Benz of Germany have indicated a commitment to provide a ceramic A.G.T. for a commercial automobile by 1990[3].

FIGURE 1.1 - Potential high temperature applications of silicon nitride-based ceramics

After reference [1] and reference [2] (marked).

- A Heat Engines
  - Gas turbine components,
  - Diesel and Adiabatic diesel components,
  - Turbo chargers,
  - Bearings (and seals)[2],
  - Heat exchangers.
- B Industrial Heat Conversion
  - Industrial heat exchangers,
  - Burner vapourisers,
  - Valves,
  - Drawing dies.
- C Metal Working
  - Tool bits[2],
  - Dies,
  - Welding nozzles, shrouds, location pins[2],
  - Molten metal handling[2].
- D Military
  - Radomes,
  - Gun barrel liners.

(b) Diesel engine components

Components operating under high stress and wear conditions in the high temperature environment of the diesel engine are obvious targets for substitution by ceramics. There is potential for

complete elimination of the cooling system to enable the running of an adiabatic diesel engine[4] and tests in the U.S.A. using ceramic piston caps in such an engine have demonstrated the "lowest specific fuel consumption for any vehicular engine".

(c) Turbochargers

Ceramic turbocharger rotors are probably the most developed application of ceramics in heat engines, and the most likely ceramic candidate to appear first in production vehicles[4]. Ford have produced a rotor with ~60% of the mass of a conventional metal component thus presenting less mass inertia to be overcome during acceleration and deceleration, thereby decreasing 'turbo lag'.

(d) Heat exchangers

Utilisation of dirty fuels, such as coal, in gas turbines for electricity generation, requires that heat input to the cycle working fluid occurs through a heat exchanger. Ceramic heat exchangers are expected to increase the working temperature of the working fluid enabling higher cycle efficiencies[5].

1.1.2 Ceramic contenders for substitution of traditional materials

Currently there are many ceramics available to the design engineer and it is important that the operating conditions are well defined prior to selection of a material suitable for a given application. It is also important to note that, often, some re-design is necessary to enable utilisation of ceramics, and direct substitution is therefore not always possible[9]. The behaviour of a ceramic component during operation will depend upon the way in which it was manufactured, different fabrication methods leading to families of ceramics based on a given oxide, nitride, carbide or combination of these. It is possible, therefore, to span a wide range of properties and combination of properties by employing ceramic materials, however the general properties of major ceramic families will now be briefly surveyed, see also Table 1.1.

(a) Aluminium oxide-based ceramics

The melting point of alumina (Al_2O_3) is ~2045°C and ceramics of high alumina content can be used at temperatures approaching this limit, since oxidation resistance is not a problem. Fabrication of complex shapes is possible and corrosion resistance is good, thus alumina in various forms has found widespread application. The use of alumina in heat engine application is limited by its thermal shock resistance,

TABLE 1.1 - Properties representative of the various ceramic families

Material	Al_2O_3 (99.8%)	SiC	Si_3N_4	
Kyocera grade	A480	SC201	SN220	
Density ($g.cm^{-3}$)	3.9	3.1	3.2	
Hardness (HR_A)	17.6 GPa*	94	91	
Flexural strength (MPa)	313	490	590	σ
Elastic modulus (GPa)	372	392	294	E
Poissons ratio	0.19	0.16	0.28	μ
Linear thermal expansion coefficient x 10^{-6} (K^{-1}), 40 - 800°C	7.8	4.2	3.2	α
Thermal conductivity ($W.m^{-1}.K^{-1}$), 20°C	29.3	67.0	16.7	
Recommended temperature ceiling (°C)	1750	1400	1200	
R (°C) **	87	250	452	
K_{IC} ($MPa.m^{-\frac{1}{2}}$) ***	~2	~3	~4	

Data for Kyocera grades obtained from Kyocera sales catalogue CAT/3T8304TDM.

* VPN_{500g}

** Analytical thermal stress resistance parameter[6]:-

$$R = \frac{\sigma.(1 - \mu)}{\alpha E}$$

*** Not evaluated specifically for the Kyocera grades but for similar members of each respective ceramic family[7].

which is low in comparison to silicon nitride-based material, creep resistance at elevated temperatures is also relatively low, as are strength and fracture toughness.

(b) Silicon nitride-based ceramics

Intrinsic to silicon nitride (Si_3N_4) is a combination of attractive properties such as high thermal shock resistance, high toughness, high strength, high corrosion resistance*, high erosion resistance and low coefficient of friction**. Thus silicon nitride-based ceramics were identified early as candidates with most promise for development for use in A.G.T's. The ensuing programme led to a wide range of silicon nitride - based materials whose maximum working temperature is variable, generally depending upon the presence of oxide/oxynitride grain boundary phases which are artefacts of the various fabrication procedures. Promising test results have been obtained from various static and dynamic silicon nitride-based components used in A.G.T's, diesel and petrol engines, and spin-off applications such as cutting tools, dies, nozzles etc. are being successfully developed. The crystal chemistry and development of the silicon nitride-based ceramic family is reviewed in section 1.2.

(c) Silicon carbide-based ceramics

Of the various silicon carbide-based ceramics hot-pressed silicon carbide (HP.SiC) with 2% Al_2O_3 addition has the highest flexural strength, but, as with silicon nitride-based ceramics, the presence of a grain boundary phase causes a drop off in strength at elevated temperatures. Sintered silicon carbide (S.SiC), however, is of higher purity and has a far superior high strength retension - see Figure 1.2. Fracture at elevated temperatures is predominantly transgranular and there is less sub-critical crack growth occurrence than in silicon nitride-based ceramics, where intergranular fracture occurs due to the secondary phases present. Since silicon carbide ceramics are usually of higher purity and closer to theoretical density than silicon nitride ceramics they exhibit superior oxidation resistance and creep resistance, their toughness and thermal shock resistance are, however, intrinsically lower. Two crystallographic forms of silicon carbide are available, α-SiC is hexagonal and obtainable in the sintered condition enabling low cost components to be fabricated, the β - form is cubic and generally available in the hot-pressed condition***. Various α-SiC heat engine and heat exchanger components have been fabricated and tested successfully, and silicon carbide ceramics may be seen as a cheaper alternative

* Acid / Alkali.

** Si_3N_4/Si_3N_4

*** A multitude of Hexagonal/Rhombohedral α-form polytypes are available, in which structural variations occur due to changes in the stacking sequence.

to silicon nitride ceramics for certain uses, especially where thermal shock resistance is a lower priority.

FIGURE 1.2 - The flexural strength of silicon carbide materials[6]

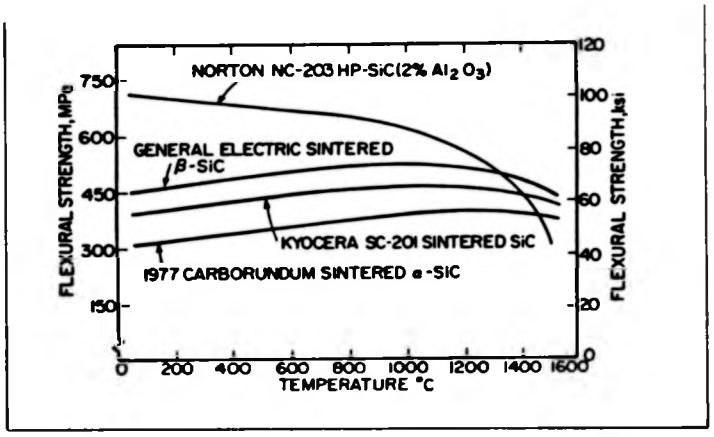

1.2 Silicon nitride-based materials and the development of Syalon Ceramics

In this section the structure and synthesis of Si_3N_4 will be briefly discussed, followed by a brief consideration of the fabrication of, and resulting microstructure in, silicon nitride-based materials.

1.2.1 Structure and synthesis of Si_3N_4

(a) Crystal structure

Silicon nitride is not found in natural occurrence but may be artificially synthesised in two distinct crystallographic forms:- α-Si_3N_4 and β-Si_3N_4. 'Idealised' and 'Actual' structures of α- and β- Si_3N_4 are presented in Figure 1.3[10] in which rotation by 180° of layers A and B yield layers C and D respectively.

The 'Ideal' α-structure is obtained by stacking of Si-N layers in an ABCDABCD... sequence producing a tetramolecular hexagonal unit cell of dimensions a = 7.753 Å, c = 5.618 Å[11]. The 'Ideal' β-structure is obtained by stacking of Si-N layers ABAB... to form a cell of dimensions a = 7.606 Å, b = 2.909 Å containing two Si_3N_4 molecules with Si-N bond lengths 1.71-1.76 Å. Thus it is readily seen that large

FIGURE 1.3 - (Opposite) Idealised and Actual Si-N layers in α- and β- Si_3N_4 (basal projections)[10]

- 'Idealised' SiN layers are represented in **c** and **d** .
- 'Actual', distorted, layers are represented in **a** and **b** .
- Section **b** is rotated by 180°, with respect to undistorted section **d** , to facilitate its comparison with section **a** .
- 'Ideal' α has SiN layers ABAB... stacked, ie. section **c** stacked.
- 'Ideal' β has SiN layers ABCD... stacked, ie. sections **c** , **d** stacked.
- 'Actual' α has **a** stacked.
- 'Actual' β has **a** stacked on a 180°rotation of **b** .

continuous channels running parallel with the c-axis in the β-structure are terminated in the α-structure, by a c-glide plane relating layers B and C, and replaced by large closed interstices.

The 'Actual' β-structure is almost identical to the 'Ideal', - compare Figure 1.3a and 1.3c, but the 'Actual' α-structure is distorted with reference to the 'Ideal' in that the N atoms around the two large interstices are pulled in towards their centres;- compare Figure 1.3a and 1.3d. Thus the β-structure is somewhat less strained than the lower density α-structure.

FIGURE 1.3 - Idealised and Actual Si-N layers in α - and β- Si_3N_4 (basal projections)

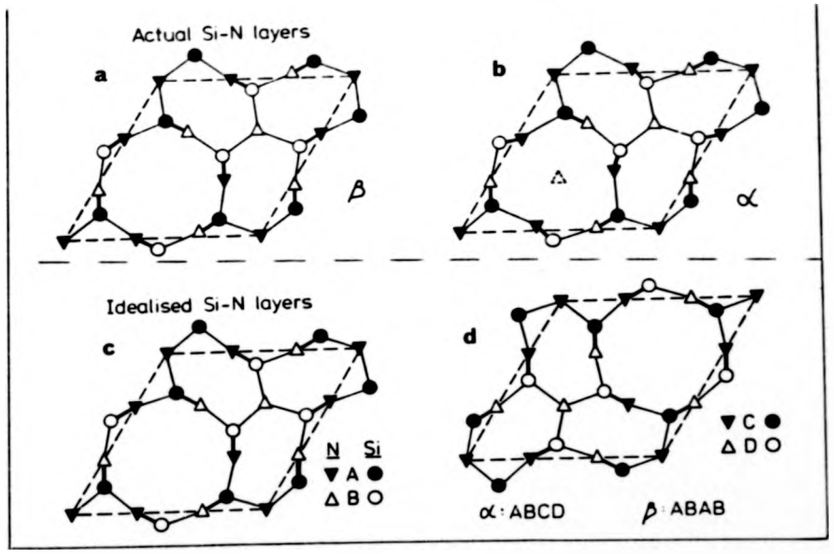

(b) Synthesis of Si_3N_4 powder

There are a variety of techniques by which Si_3N_4 may be produced, and it is a general observation that vapour phase reactions favour formation of the α-structure while liquid phase reactions favour β-Si_3N_4 formation. The most popular methods applied by manufacturers will now be briefly considered.

(1) Nitridation of silicon powder - Typically a silicon powder bed (or compact) is heated, under a nitrogen, nitrogen + hydrogen or ammonia overpressure, to temperatures between 1300°C and 1500°C. Predominantly

α-Si_3N_4 is obtained, but increasing the temperature above 1450°C leads to a significant increase in the abundance of β-Si_3N_4.

The exothermic reaction $3Si + 2N_2 \longrightarrow Si_3N_4$ is applicable, and it has been suggested[12] that combination of silicon with molecular nitrogen presents a steric hindrance leading to formation of α-Si_3N_4, while combination with dissociated nitrogen leads to the simpler β-Si_3N_4 structure.

After milling, to reduce the powder particle size, and chemical treatment, to remove impurities, the resulting product is suitable for generating dense ceramics, a typical powder analysis is given in Table 1.2.

TABLE 1.2 - Typical analysis of Starck LC10 grade Si_3N_4 powder[13]

% phases present			impurities present					BET	FSSS
β-Si_3N_4	free Si	SiO_2*	O%	C%	Fe%	Al%	Ca%		
3	<0.1	2.8	1.5	0.1	0.03	0.08	0.02	5	0.5

* calculated

BET specific area $m^2.g^{-1}$

FSSS grain size μm

(2) Carbothermic reduction of silica - Since silica and carbon may be obtained in the pure, finely divided, state at a lower cost than silicon, this technique of silicon nitride production may become favourable when further developed. Flow of nitrogen gas over a powder bed, containing excess carbon, at temperatures up to 1500°C leads to the reaction:-

$$3SiO_2 + 6C + 2N_2 \longrightarrow Si_3N_4 + 6CO$$

A post-production heat-treatment at 700°C is required to remove residual carbon, the final powder contains $\sim 5\%$ β-Si_3N_4 and may be considered of high purity apart from a relatively large carbon content of $\sim 2\%$[14].

(3) Chemical Vapour Deposition (CVD) - By varying reaction conditions this technique allows production of amorphous silicon nitride, however, some crystallisation to α-Si_3N_4 may occur during purification treatment. The product of vapour phase reaction is usually of high purity but manufacture is a relatively high cost process.

eg. $3SiCl_4 + 4NH_3 \rightarrow Si_3N_4 + 12HCl$

or $3SiH_4 + 4NH_3 \rightarrow Si_3N_4 + 6H_2$

1.2.2 Fabrication of silicon nitride ceramics

If silicon nitride-based ceramics are to be fully utilised in advanced technological roles there is a requirement to mass produce complex shapes, of near-theoretical density, at low cost. The low self diffusivity intrinsic to pure Si_3N_4 prevented success in early fabrication attempts. At temperatures high enough to achieve the necessary atomic mobility thermal decomposition led to high weight losses and production of weak and porous materials. It is now known that thermal decomposition of silicon nitride can be suppressed by the use of high nitrogen overpressures - see Figure 1.4, and application of 5GPa at 1600°C has produced ceramics of ~95% theoretical density[16], however, the chemical purity of this material was not assured[17].

Commerical production of pure Si_3N_4 is therefore not a viable process, and use of sintering additive 'impurities' is a necessity.

FIGURE 1.4 - The region of sinterability of Si_3N_4 as a function of nitrogen temperature and pressure, in equilibrium with Si vapour pressure[15]

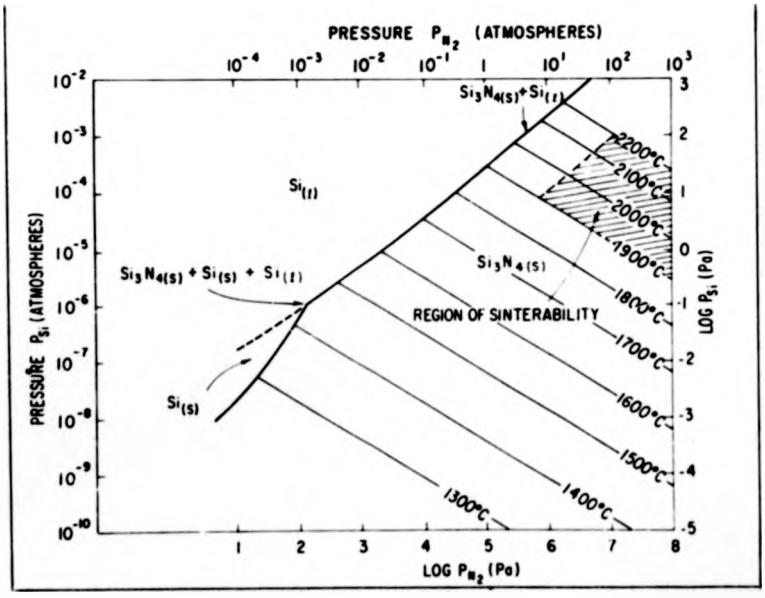

(a) Hot-pressing with densification aids

An addition of 1-2% MgO to Si_3N_4 powder was found to enable fabrication of strong ceramics with near-theoretical density[18].

Further work suggested that densification was enhanced by the presence of oxygen, combined as amorphous SiO_2, on the surface of the α-Si_3N_4 source powder[19]. It was proposed that reaction between MgO and SiO_2 causes liquid formation at the fabrication temperature[20], and the residual glass was identified in the ceramic microstructure using TEM[21]. This led to the proposal that the sintering mechanism was that of dissolution of α-Si_3N_4 into the liquid silicate phase and reprecipitation of β-Si_3N_4 (see also Chapter 2).

Thus, hot-pressing with densification aids enabled batch production of strong ceramic material, but it is a costly process capable only of producing components of simple shape and low dimensional tolerance.

(b) Reaction Bonded Silicon Nitride

Another approach to the problem of densification of silicon nitride components involves the nitridation of a pressed silicon compact in a similar manner to that previously described (section 1.2.1 (b)). The Reaction Bonded Silicon Nitride (RBSN) so produced is composed mainly of α-Si_3N_4 with some β-Si_3N_4, free silicon and a large volume of porosity. A variety of complex shapes may be cheaply produced using traditional ceramic shaping techniques such as slip casting, isostatic pressing and, more recently, extrusion and injection moulding. A further development of this approach is the concept of Sintered RBSN (SRBSN)[22], which may lead to the mass production of cheap dense silicon nitride components of complex shape.

(c) Pressureless Sintered Silicon Nitride (SSN)

To produce a Hot-Pressed Silicon Nitride (HPSN) ceramic both pressure and heat are applied to a powder compact. In the technique of pressureless sintering provision of energy in the sole form of heat leads to consolidation and densification of the powder compact. The driving force for both techniques is the same, reduction of interfacial energy in the compact, and densification occurs by the same process of sintering. Successful pressureless sintering therefore requires higher temperatures than hot-pressing, thermal decomposition of Si_3N_4 being suppressed by use of the powder bed method, in which green compacts are embedded in a powder of similar composition and heated under a nitrogen atmosphere[23].

The choice of densification aids was made from hot-pressing experience where use of metal oxides (M_xO_y), eg. MgO, SiO_2, Y_2O_3, Al_2O_3, BeO and others had proven successful, and use of fine powders

(~0.5μm) providing large driving forces and small diffusion distances, had improved sinterability*.

Post-sinter heat-treatment designed to de-vitrify the remnant intergranular glass in the microstructure of SSN, was found to improve high-temperature performance[24] and further development in this direction is widely reported in the literature[25],[26],[27]. In terms of performance/cost ratio SSN may be seen to lie between high strength, high cost HPSN and relatively low cost, low performance RBSN, and is therefore considered uncompetitive for many applications.

(d) Hot Isostatic Pressing (HIP)

Isostatic application of pressure (~200MPa) via a gas at temperatures of ~1700°C has been found to enable production of fully dense silicon nitride components of complex shape[28],[29]. The process may be applied to powders, green compacts or to pre-sintered SSN or RBSN[30] components, which have not reached full theoretical density. At present the high cost penalty of this technique makes it uncompetitive for most applications, but since it enables production of high performance capability, complex shape components, it is expected to find use in high technology manufacture eg. production of turbine blades.

1.2.3 The development of Syalon Ceramics

(a) HPSiAlON ceramics

During the 1970's it was recognised[31],[32] that the basic β-Si_3N_4 structure could accomodate Al^{3+} and O^{2-} in direct substitution for Si^{4+} and N^{3-} to form β' Si-Al-O-N solid solutions. Maximum substitution of Al^{3+} was found to yield the most nearly single phase material, and such compositions were identified[33] with the formula $Si_{6-z}Al_zO_zN_{8-z}$ ($z \lesssim 4$). The previous use of impurity elements to enhance densification of silicon nitride-based systems[18] led to the development of hot-pressed M-Si-Al-O-N systems**, exhibiting superior performance to HPSN at elevated temperatures[34],[35]. A 'refractory grain boundary approach' was advanced[36] in which the amount of densification aid was optimised rather than minimised, and use of Y_2O_3 was found to enable formation of refractory grain boundary phases with promise for service at elevated temperatures. The same limitations conferred on HPSN apply to HPSiAlON,- inability to produce complex shapes and high component cost.

* NB. The competing processes of sintering and thermal decomposition are both affected by reducing α-Si_3N_4 particle size, as is the amount of SiO_2 present.

** M = Metal cation.

(b) Pressureless sintered Syalon Ceramics

Following the development pattern of silicon nitride materials, investigation of M-Si-Al-O-N ceramic systems (in which M represents a metal ion) led to the production of pressureless-sintered MSiAlON ceramics. Various densification additives eg. MgO, Sc_2O_3 and CeO_2 have been, and are being, assessed, but the most widely applied is Y_2O_3, - producing ceramics in the system YSiAlON. Such materials produced by Lucas Cookson Syalon Ltd. (Birmingham), have been given the tradename Syalon Ceramics, and are the subject of the investigation reported in this thesis. A typical property specification for a Syalon Ceramic alloy is presented as Table 1.3.

TABLE 1.3 - Properties typical of Syalon Ceramic
(at room temperature unless stated otherwise)

Property	Value
Density	3.24 $g.cm^{-3}$
Hardness	18 GPa
Elastic Modulus (E)	300 GPa
Poissons Ratio (μ)	0.28
Thermal expansion coefficient (0-1000°C)	3.2 x 10^{-6} K^{-1}
Thermal conductivity	20-25 $W.m^{-1}.K^{-1}$
Porosity	0.01 %
z in $Si_{6-z}Al_zO_zN_{8-z}$	0.2 (to 1.2)
Volume fraction of intergranular glass	10 %

* After reference [37].

Nb. Syalon Ceramics may be produced from a range of compositions, leading to property variation, the table is meant to serve only as an approximate guide.

Compare with Table 1.1.

In the 'as sintered' condition the β' SiAlON grains of size ~ 2μm are surrounded by a matrix of yttrium aluminium silicate glass[38] which may crystallise, often to Yttrogarnet ($Y_3Al_5O_{12}$),** on further heat-treatment (-see Chapter 3). Long term heat-treatment of such ceramics has been found to cause the Yttrogarnet (YAG) phase to become disconnected and granular,[27] thereby enhancing high temperature mechanical performance. The driving force for this phenomena is the consequential reduction in β'/YAG interfacial energy and the root of the performance

** Yttrium Aluminium Garnet (YAG).

improvement is the reduced ionic mobility along β'/YAG boundaries[27]. The high temperature performance of these ceramics is found to be superior to that of HPSiAlON and the relatively low performance glass-matrix Syalon Ceramics have already been exploited in a cutting tool role[26].

1.3 Thesis plan and objectives of the research programme

The broad objectives of the research programme were:-

1. To discern the relationships between Syalon Ceramic 'as mixed' composition and the resulting microstructural parameters derived during sintering.

2. To define the character of crystallisation occurring in the intergranular phase of Syalon Ceramics, of varying composition, at various temperature levels in the devitrification regime.

3. To relate the crystallisation behaviour to intergranular phase composition and identify heat-treatment parameters likely to produce high nucleation densities.

4. To ascertain the high temperature creep-performance of various ceramic alloys with the aim of identifying materials which show most promise for engineering use.

Following the general introduction of Chapter 1 there are six further chapters in this thesis:-

Chapter 2 - is a review of sintering behaviour, and details concerning the fabrication and likely densification mechanisms of Syalon Ceramics are considered.

Chapter 3 - is presented in two main sections in which the microstructural evolution of silicon nitride ceramics at elevated temperatures and the creep behaviour at elevated temperatures, are reviewed. Emphasis is placed on the properties of the intergranular phase and how these affect the ceramic composite.

Chapter 4 - details the characterisation of microstructures present in various ceramic alloys and the results presented form the

basis of this thesis, upon which the objectives of the research programme are realised.

Chapter 5 - is a presentation of results obtained from a heat-treatment programme in which the devitrification of the intergranular phase was studied.

Chapter 6 - is a consideration of the data obtained from high temperature creep experiments performed on Syalon Ceramic specimens.

Chapter 7 - is a statement of conclusions, derived from the work reported in this thesis and recommendations for future work are suggested.

Although each chapter was originally meant to be 'self-contained' some cross-reference between chapters was inevitable and aids an understanding of the work presented.

CHAPTER 2.- The mechanism and detail of Syalon Ceramic fabrication

This chapter is presented in two main sections. In the first section the densification behaviour of silicon nitride ceramics is considered, and mechanisms of sintering applicable to Syalon Ceramic compacts are discussed. Compositional data and the various aspects of fabrication are detailed in the second main section.

2.1. Sintering mechanisms and the densification of silicon nitride ceramics

2.1.1 The Kingery Model

During the densification of silicon nitride ceramics the reaction of surface SiO_2 with oxide additives forms an oxynitride liquid which promotes both shrinkage and the $\alpha \rightarrow \beta$ phase transformation, as earlier described in Section 1.1.2. Such 'liquid phase sintering' has traditionally been interpreted by reference to the theoretically derived Kingery Model[39] in which three, possibly overlapping, stages of densification are discerned:-

Stage 1. - Primary particle rearrangement

Immediately upon formation of the liquid phase, the remaining solid particles rearrange causing shrinkage to an extent dependent upon their mobility. Influencing factors relate to both the particles (eg. size, shape, surface roughness and distribution) and to the liquid (eg. amount present, viscosity and wetting characteristics for the particles). Shrinkage kinetics, driven by capillary forces are described by the relation:-

$$\Delta V/V_o \propto t^{1+y}$$

Stage 2. - Secondary particle rearrangement by solution, diffusion and re-precipitation

Assuming solubility of the particles in the liquid phase, densification kinetics are described by the relation:-

$$\Delta V/V_o \propto t^{1/n}$$

which was derived using the 'contact flattening' approach in which dissolution of particles at highly stressed contact points and re-precipitation after transport, due to lower solubility in less stressed regions, is the assumed mechanism.

Time laws for densification by this mechanism have been verified experimentally[40],

where, n = 3 is identified with a solution or precipitation rate controlling step,

and n = 5 describes rate control by diffusion through the liquid (assuming non-spherical particles).

FIGURE 2.1

Kingery Model plot for liquid phase sintering (schematic)

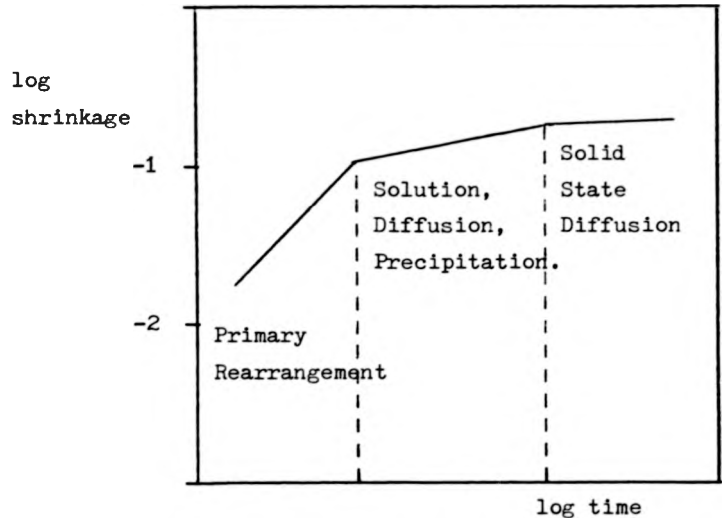

Stage 3 - Solid state diffusion

Liquid phase sintering effectively ceases and elimination of closed porosity occurs through bulk diffusion. In the case of silicon nitride based ceramics any contribution, of this type, to shrinkage is unlikely without the application of high pressure.

2.1.2 The liquid sintering medium

The Kingery Model requires an appreciable presence of liquid capable of completely wetting and expressing solubility for the solid particles present. To explain the densification kinetics experimentally observed for silicon nitride based ceramics, therefore, requires a consideration of the likely composition and properties of the liquid sintering medium.

The liquid regions present during sintering must be at least as extensive as those of the glasses derived from them, and observed in the final microstructure of as-sintered ceramics, thus it seems reasonable to assume that their compositions are similar. The temperatures of initial liquid formation observed with additions of various metal oxides to silicon nitride containing 4W% surface SiO_2 are usually significantly lower than the lowest solidus temperature in the corresponding M_xO_y-SiO_2 system, consider Table 2.1.

TABLE 2.1 - Liquid formation temperature for Si_3N_4 powder with 5W% addition of metal oxide[40]

M_xO_y	Li_2O	MgO	Y_2O_3	CeO_2	ZrO_2	Al_2O_3
Liquid formation (°C)	1050	1390	1440	1470	1590	1470
M_xO_y-SiO_2 solidus (°C)	1030	1543	1660	1560	1640	1595

This effect has been explained by noting the action of nitrogen present in the liquid which is observed to lower the eutectic temperature while increasing viscosity[41]. Other elements present as impurities also have an effect in decreasing the eutectic temperature[42]. The particular oxide or mixture of oxides selected for use as densification aid changes liquid properties, eg. with a constant atomic ratio MSiAlON glasses (and liquids) produced with Y_2O_3 are found to be more viscous than those produced with MgO. The effect of Al_2O_3 addition to MSiO(N) glasses is to reduce the lowest liquidus temperature of the binary Y_2O_3- SiO_2 eutectic (~1660°C) to the ternary Y_2O_3-SiO_2-Al_2O_3 eutectic ($\lesssim$ 1400°C)- see Figure 2.2.

2.1.3 Densification of Si_3N_4-based ceramics

SSN produced with 5W% MgO or 7W% Y_2O_3 additive exhibits densification behaviour which has been related to sintering liquid properties[40]:-

With MgO addition, primary rearrangement is found to provide ~50% of the total shrinkage required for full densification, and the secondary rearrangement kinetics are characterised by n = 3 behaviour indicating β precipitation as the rate controlling step. Thus the $\alpha \rightarrow \beta$ transformation is accompanied by material transport, achieving over 90% of full densification with only partial transformation.

PLEASE FOLD OUT

FIGURE 2.2 - The Y-Si-Al-O system and related binary phase diagrams

All details redrawn in 'equivalent' terms from data in the literature[43].

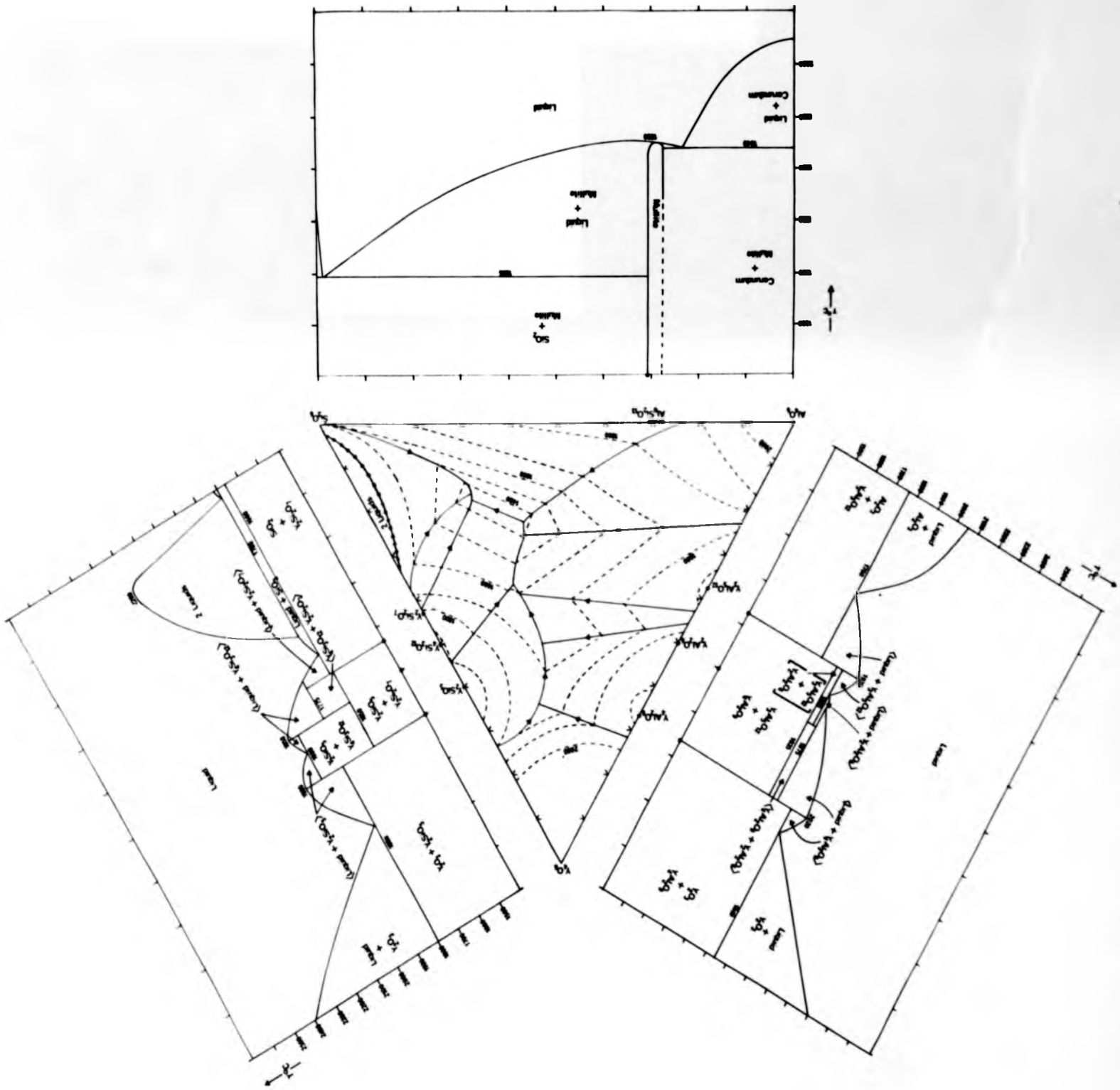

By comparison the Y_2O_3 addition generates a lower volume of more viscous liquid. Only 25% of full densification is achieved during primary rearrangement and the decreased diffusivity leads to n = 5 behaviour in the secondary rearrangement stage, where densification rate is governed by diffusion.

For the case of β' SiAlON ceramics, densified with either MgO or Y_2O_3, the effect of Al_2O_3 in producing large volumes of low viscosity liquid leads to production of almost fully dense ceramic with an n = 3 second stage characteristic.

In each case the activation energy for sintering, ie. β (or β') formation, was found to be $\sim$405 kJ.mol^{-1} which is similar to the Si-N bond dissociation energy (435 ± 38 kJ.mol^{-1}) and this suggests that the $\alpha \rightarrow \beta$ transformation is a reconstructive one. Thus, the anisotropic α-Si_3N_4 is dissolved and reprecipitated in the β form, as experimentally observed[21].

2.1.4 Further development of the densification model

Despite the apparent success of the Kingery Model in explaining observed densification kinetics in Si_3N_4 based ceramic systems, recent reviews have challenged certain aspects of this approach. The Kingery densification equations were derived on the basis of the 'contact flattening' model in which only limited driving force is available due to the rapid decay of contact stress with increased contact area[44]. For systems of continuous particle size distribution, a shape accomodated Ostwald ripening mechanism, in which small particles are dissolved and re-precipitated onto larger particles, due to differences in specific surface energy of curved surfaces, may provide a major contribution to shrinkage.

Chemical reactions may occur during liquid phase sintering, and these can cause a decrease in free energy of the system an order of magnitude greater than the geometrical changes so far considered. Thus, when differences in phase or chemical composition exist between dissolved and re-precipitated material, this driving force may become available for initiation or acceleration of solution - precipitation mechanisms. It should be noted, however, that these phenomena do not provide the driving force for densification, which is due solely to the decrease in interfacial energy[45].

2.1.5 Sintering mechanisms applicable to Si_3N_4 ceramics

Primary rearrangement begins at the temperature of initial silicate liquid formation and the kinetics of this stage are thus compositionally dependent. For green compacts produced from fine α-Si_3N_4 powder this process is envisaged to occur as a simultaneous interaction of many particles by a viscous flow mechanism. There is considerable overlap between this and the next stage of sintering.

Secondary rearrangement by solution and re-precipitation occurs, the driving force for densification being the decrease in interfacial energy which occurs when lathy α-Si_3N_4 grains are replaced by β-Si_3N_4 exhibiting a lower shape anisotropy. Thus, the observed $\alpha \rightarrow \beta$ transformation may be considered to provide a large acceleration to sintering kinetics even though any difference in free energy between the α and β phases is only small[12], β phase being less strained and more symmetrically bonded. Growth of β grains at the expense of α particles might be envisaged to occur by three possible mechanisms:-

(1) Initially, contact flattening may lead to dissolution of α and re-precipitation of the slightly more stable β phase, the transformation occuring due to the fact that upon reconstruction nitrogen is presented in dissolved ionic form rather than the sterically hindering molecular form[12].
During this stage, precipitation of β phase occurs either on α particle free surfaces or at α-α contact points, the major mode depending upon liquid viscosity. There is also the possibility for growth onto the small amount of β grains already present, see Table 1.2, or onto any other particles, as well as seperate homogeneous nucleation in the liquid. Increase in contact area rapidly decays contact stresses and this stage ends.

(2) Directional grain growth may occur, with preferential α solution at non-faceted lath ends and re-precipitation causing directional growth of a lower aspect ratio along the β hexagonal layer structure in the $\langle 0001 \rangle$ direction.
In the case of β' SiAlON formation there is an extra chemical driving force which may accelerate

* (Opposite)

21R polytypoid in the SiAlON compositional plane, (see Figure 2.6) has a 21 layer repeat stacking sequence of Rhombohedral symmetry (Ramsdell notation), it is used in preference to the AlN component in the fabrication of Syalon Ceramics (see Section 2.2.2).

grain growth, the driving force increasing as the Al_2O_3 substitution level increases in the β'_{ss}.

(3) Once the β (or β') grains have exceeded the size of the α particles, growth by Ostwald ripening may increase the β fraction. Shape accomodated Ostwald ripening will also lead to further grain growth at the expense of small β grains.

It should be emphasised that grain growth and rearrangement occur coincidentally and continuously allowing pore filling and hence shrinkage.

The conclusions available from a recent study[46], of densification and crystalline phase evolution observed in Syalon Ceramics sintered at various temperatures, are also relevant:-

(1) Densification is promoted by the presence of impurity ions, eg. Fe^{3+} and Ca^{2+}, which lower the liquidus temperature.

(2) Although high Si_3N_4 surface area promotes sintering at lower temperatures, with use of very fine source powders, decomposition can become a problem as low as 1750°C, leading to inhomogeneity and low density.

(3) Increasing the 21R polytypoid addition* retards densification at sintering temperatures up to 1500°C but at higher temperatures leads to increased bulk density.

(4) After 5 hrs. at 1300°C, no trace of polytypoid and a large fraction of YAG are identified in compacts by use of X-Ray Diffractometry (XRD). A solid state reaction was proposed but is not commensurate with the observed enhancement of the β' fraction which necessitates the formation of a liquid phase.

(5) The temperature range compatible with intermediate YAG persists to ~1500°C or 1600°C in ceramics with low or high amounts of 21R addition, respectively.

(6) Whereas the fully densified product of an alloy with low 21R addition contains β' and glass only; the presence of 'B-phase' (Y_2SiAlO_5N) is identified in the as-sintered billets of alloys containing large polytypoid additions. This implies a high nitrogen concentration in the intergranular material upon

* (Opposite)

21R polytypoid in the SiAlON compositional plane, (see Figure 2.6) has a 21 layer repeat stacking sequence of Rhombohedral symmetry (Ramsdell notation), it is used in preference to the AlN component in the fabrication of Syalon Ceramics (see Section 2.2.2).

grain growth, the driving force increasing as the Al_2O_3 substitution level increases in the β'_{ss}.

(3) Once the β (or β') grains have exceeded the size of the α particles, growth by Ostwald ripening may increase the β fraction. Shape accomodated Ostwald ripening will also lead to further grain growth at the expense of small β grains.

It should be emphasised that grain growth and rearrangement occur coincidentally and continuously allowing pore filling and hence shrinkage.

The conclusions available from a recent study[46], of densification and crystalline phase evolution observed in Syalon Ceramics sintered at various temperatures, are also relevant:-

(1) Densification is promoted by the presence of impurity ions, eg. Fe^{3+} and Ca^{2+}, which lower the liquidus temperature.

(2) Although high Si_3N_4 surface area promotes sintering at lower temperatures, with use of very fine source powders, decomposition can become a problem as low as 1750°C, leading to inhomogeneity and low density.

(3) Increasing the 21R polytypoid addition* retards densification at sintering temperatures up to 1500°C but at higher temperatures leads to increased bulk density.

(4) After 5 hrs. at 1300°C, no trace of polytypoid and a large fraction of YAG are identified in compacts by use of X-Ray Diffractometry (XRD). A solid state reaction was proposed but is not commensurate with the observed enhancement of the β' fraction which necessitates the formation of a liquid phase.

(5) The temperature range compatible with intermediate YAG persists to ~1500°C or 1600°C in ceramics with low or high amounts of 21R addition, respectively.

(6) Whereas the fully densified product of an alloy with low 21R addition contains β' and glass only; the presence of 'B-phase' (Y_2SiAlO_5N) is identified in the as-sintered billets of alloys containing large polytypoid additions. This implies a high nitrogen concentration in the intergranular material upon

completion of the $\alpha \rightarrow \beta'$ transformation.

(7) Large additions of 21R (>10w/o with Starck LC10 Si_3N_4) may lead to formation of α' phase.

Taking available[46] measurements of bulk density and crystalline phase analysis, it is possible (assuming a conservative sintering system) to construct curves representing % shrinkage and fraction of α-Si_3N_4 transformed to β' SiAlON, as a function of temperature - see Figure 2.3. By comparing the curves it may be seen that Syalon Ceramic with a 2w/o 21R addition attains 50% of total densification ($\rho_x - \rho_o / \rho_x \approx 30\%$) at $\sim$1400°C with negligible $\alpha \rightarrow \beta'$ conversion. Increasing the 21R addition to 6w/o requires an increase in temperature to 1500°C to achieve the same degree of densification and the $\alpha \rightarrow \beta'$ conversion is well advanced resulting in a β' content of $\sim$50%. Ceramics prepared with 4w/o and 8w/o 21R addition also fit this trend, but results are not included for the sake of brevity. Similarly, results from alloys prepared with different Si_3N_4 source powders confirm the effect, but it should be noted that higher temperatures are necessary to obtain densification from a Si_3N_4 powder provided by a different manufacturer to H.C. Starck Ltd.

These results indicate that the primary rearrangement stage of sintering accounts for a large proportion of total densification, at low temperatures, in alloys prepared with low 21R contents. However, increasing the 21R content decreases the importance of the low temperature step and $\alpha \rightarrow \beta'$ conversion, at higher temperatures, accounts for the dominant densification mode.

2.2. Fabrication of Syalon Ceramics

2.2.1 The method of fabrication

Billets of experimental grade Syalon Ceramic alloys were produced at Lucas - Cookson Syalon Ltd by the same process, and in the same hardware, as used for fabrication of commercial grades:-

(a) Milling

The component powders* were weighed and mixed to a total mass of 1.4 kg and, after pouring into spherical polyethylene pots, 5.5 kg of alumina milling media were added. The remaining volume of the 5 l. capacity pots was filled with isopropanol and after sealing and placing on a mill they were continuously rotated for 72 hrs.

* see 2.2.2

FIGURE 2.3 - The densification behaviour of Syalon Ceramics

Constructed assuming conservation of the sintering system and using data[46] obtained from sintered Syalon Ceramics produced from LC.10 Si_3N_4 powder (H.C. Starck Ltd).

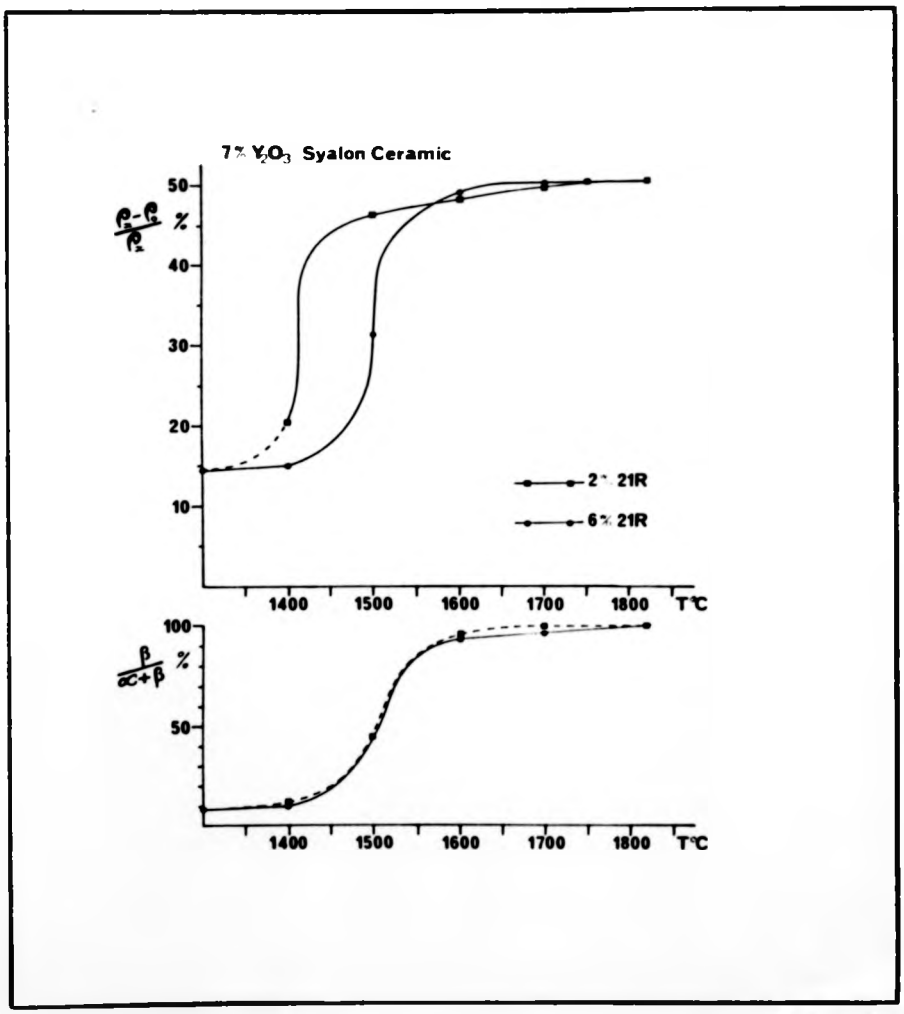

% Shrinkage = $\Delta V/V = (V_o - V_x)/V_o$, assuming constant mass = $(\rho_x - \rho_o)/\rho_x$

ρ_o = density of green compact ≈ 1.6 g.cm^{-3}.

Up to 1750°C samples sintered for 5 hrs.

>1750°C samples sintered for 2 hrs.

(b) Drying of the milled powders

After milling the resultant slurry was washed, with isopropanol, through a 90μm sieve to seperate out the alumina media. It was then dried, either under vacuum in a commercial stainless-steel pan drying apparatus, or in open trays at ~80°C in a ventilated oven. When dry the powders were sieved through a 1mm mesh and stored in sealed pots. The weight of media lost to the powder in the form of Al_2O_3 contamination was determined by difference before and after milling.

(c) Pressing of green compacts

Powder loads of ~120 - 150g were tamped into rubber bags and isostatically pressed at 138 $MN.m^{-2}$ to a green density of 1.6 $g.cm^{-3}$. After de-bagging and engraving with identification numbers, each billet was coated with a slurry (50% BN, 50% SiO_2 plus collodion binder in methyl-pentane solvent) designed to suppress surface reaction and decomposition during sintering.

(d) Sintering

After carefully purging the resistance heated, graphite lined, furnace, billets were sintered under static nitrogen with a pressure relief valve setting $2kN.m^{-2}$ above ambient atmospheric pressure. A typical sintering profile is presented as Figure 2.4 and the details pertaining to individual alloys is provided below it.

2.2.2 Compositional balance and Syalon Ceramics

To produce a 'balanced' SiAlON composition, ie. one that lies along the β' line defined by $Si_{6-z}Al_zO_zN_{8-z}$ as presented in Figure 2.5, it is necessary to add Al_2O_3 to Si_3N_4, and also some AlN to compensate for the surface SiO_2 contaminant. Using this principle nominally single phase β' SiAlON ceramics may be produced by hot pressing, the components of the sintering liquid being largely removed into solid solution leaving grain boundaries which contain only segregated ions within a width of the same order of the β' lattice spacing[34].

Pressureless sintered Syalon Ceramics are fabricated with much larger liquid volumes, the resultant microstructure consisting of β' SiAlON grains enveloped in a residual glass phase. The source materials used in production of these ceramics will next be considered:-

(a) Silicon nitride

Fine silicon nitridation product α-Si_3N_4 powders available commercially, eg. Norton Ltd (USA) and H.C. Starck Ltd (Berlin), were selected,

FIGURE 2.4

Schematic of sintering profile for Syalon Ceramics.

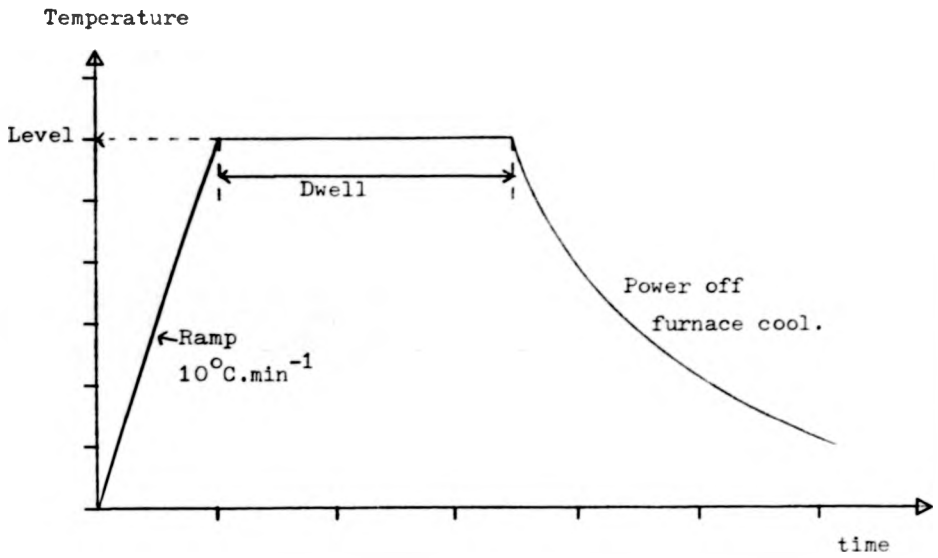

Sinter details;

Alloy	Level	Dwell
N-2, N-4, N-6, N-8	1840°C	1 hr
N-5	1780°C 1860°C	1 hr 1 hr
S-0, S-11.5	1850°C	1 hr
S-10.75A	1750°C	5 hr
S-10.75B	1700°C	5 hr

occasionally pure SiO_2 (BDH) additions were made to supplement that on the Si_3N_4 surface in adjusting liquid composition and volume.

(b) Alumina

Al_2O_3 contamination as a by-product of the milling process was controlled to within 4-5% of the total mill charge. Occasionally pure Al_2O_3 powder (Linde B) was added to adjust composition.

(c) Aluminium nitride

Commercial AlN has a variable contaminant surface oxide level, a high free aluminium content and is readily hydrolysed, thus its use has now been superceded by addition of one, or more, of the Polytypoid phases (usually 21R) - see Figure 2.5. Polytypoid grains may be considered as variants of the AlN (wurtzite) structure and are produced by reaction of AlN, Al_2O_3 and Si_3N_4 under a nitrogen atmosphere. The product lathy crystals, typical of the gaseous formation process, are similar in size and shape to the α-Si_3N_4 grains previously described.

(d) Yttria

Standard powder of high purity (Rare Earth Products Ltd.) was used.

FIGURE 2.5

The % Janecke prism representation of the Y-Si-Al-O-N system

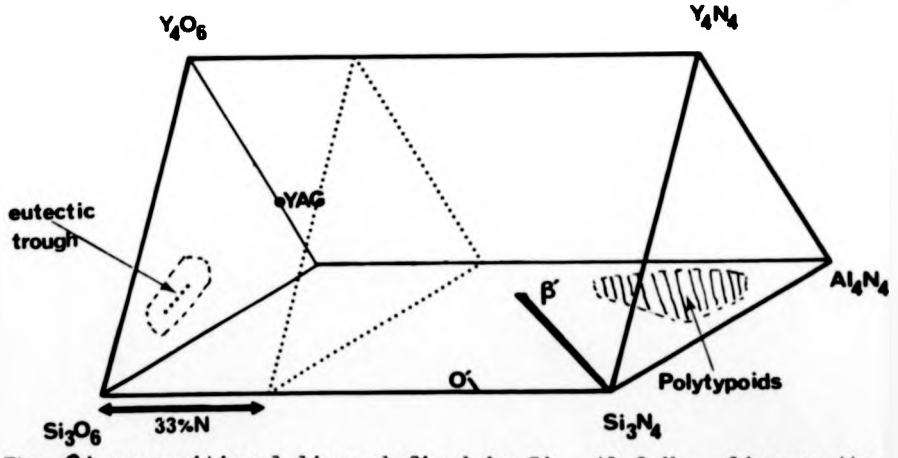

The β' compositional line, defined by $Si_{6-z}Al_zO_zN_{8-z}$ lies on the base plane and the eutectic region of the Si_3O_6 - Al_4O_6 - Y_4O_6 ternary oxide diagram is indicated.

(e) Syalon Ceramic alloy composition

The compositions of various Syalon Ceramic alloy powder mixes are presented in Table 2.2.

'Model 1' is a calculation used to predict the expected β' substitution level, z, in $Si_{6-z}Al_zO_zN_{8-z}$. The model assumes that each alloy contains only β' and an intergranular glassy matrix of Al_2O_3 - SiO_2 - Y_2O_3 ternary eutectic composition, that all yttrium ions reside in this phase and that the system is a conservative one during sintering. It may be seen (Table 2.2) that the model predicts an increase in z with 21R addition, for the proposed compositions.

'Model 1A' is a calculation of the 'potential liquid forming component' composition for each alloy, ignoring the presence of Si_3N_4 (but not its associated surface SiO_2), the results are presented in Table 2.3 and displayed as normal projections in Figures 2.6 and 2.7. In comparison to the ternary oxide eutectic composition all the calculated compositions are relatively rich in aluminium and nitrogen and poor in silicon and oxygen. From Figure 2.7 it may be seen that all projected compositions melt below 1800°C, especially S-0, also any nitrogen addition and the presence of impurities are expected to lower all liquidus temperatures further. However, as discussed previously, it is known that reactions occur at much lower temperatures (~1300°C) implying the formation of a near-eutectic composition oxynitride liquid and some YAG ($Y_3Al_5O_{12}$). Formation of YAG may occur by direct reaction of Al_2O_3 with Y_2O_3 or possibly by reaction of Al_2O_3, Y_2O_3 and polytypoid which would result in creation of some high z β'. Either reaction would result in some depletion of excess Al^{3+} and Y^{3+} and hence relative enrichment of Si^{4+} in the sintering liquid. Further changes of liquid composition occur upon dissolution of α -Si_3N_4 which must begin soon after initial liquid formation, since a rise in the fraction of β (or β'), as observed, requires this. Model 1A predicts that the nitrogen content of the sintering liquid and hence final intergranular glass must increase with 21R addition for the proposed compositions.

The increased nitrogen and aluminium levels present in the sintering liquid, on addition of 21R, are expected to retard the onset of densification to higher temperatures, as observed, the Al^{3+} causing a rise in liquidus and the N^{3-} increasing viscosity (see Figure 2.3). However the increase in z, derived from 21R addition, must increase the driving force for the $\alpha \rightarrow \beta'$ transformation, thereby increasing densification rates at higher sintering temperatures,

TABLE 2.2

Alloy	As mixed alloy composition					$\frac{O}{O+N}$	$\frac{Al}{Al+Si}$	Model 1
	a% Si	a% Al	a% Y	a% O	a% N	a%	a%	β'_z *
N-2	38.046	3.155	1.129	7.973	49.697	13.83	7.66	0.253
N-4	37.405	3.871	1.129	8.166	49.430	14.18	9.38	0.373
N-5	37.084	4.229	1.129	8.262	49.296	14.35	10.24	0.432
N-6	36.763	4.587	1.130	8.358	49.162	14.53	11.09	0.490
N-8	36.120	5.304	1.130	8.551	48.894	14.89	12.81	0.606
S-0	38.594	2.209	1.308	8.741	49.148	15.10	5.41	0.060
S-11.5	35.850	5.736	1.171	7.609	49.634	13.29	13.79	0.612
S-10.75	35.605	5.880	1.238	8.056	49.221	14.07	14.17	0.675

As mixed compositions of Syalon Ceramic alloys.

* z in formula $Si_{6-z}Al_zO_zN_{8-z}$ calculated assuming no losses on sintering and formation of eutectic ternary oxide glass of composition;
10.43 a% Al, 18.52 a% Si, 7.34 a% Y, 63.70 a% O.

TABLE 2.3

Alloy	a/o Si	a/o Al	a/o Y	a/o O	a/o N	a/o $\frac{O}{O+N}$	a/o $\frac{Al}{Al+Si}$	
N-2	8.909	22.347	7.912	56.082	4.750	0.922	0.715	
N-4	8.325	24.642	7.065	51.486	8.483	0.859	0.747	
N-5	8.077	25.615	6.706	49.538	10.065	0.831	0.760	
N-6	7.853	26.493	6.382	47.778	11.494	0.806	0.771	
N-8	7.465	28.018	5.820	44.725	13.973	0.762	0.790	
S-0	12.371	15.799	9.355	62.474	0	1	0.561	
S-11.5	7.804	28.873	5.694	37.976	19.654	0.659	0.787	
S-10.75	7.251	28.869	6.078	39.556	18.245	0.684	0.799	
Ternary Eutectic	18.52	10.43	7.34	63.70	0	1	0.36	(for comparison)

Calculated composition of initial liquid forming component.

Model 1A calculation assumes no losses on sintering, no other phases are formed and ignores the presence of Si_3N_4.

when the necessary diffusivity is attained, as also observed.

On cooling after densification further β' precipitation may occur, the final microstructural state for most compositions being that of β' and intergranular oxynitride glass.

The relationship between sintering behaviour and ceramic composition has now been partly demonstrated and the first objective of this research programme will be further developed in Chapter 4.

FIGURE 2.6 - Projection of the possible liquid forming component onto the isothermal phase diagram for the system Si_3N_4 - AlN - Al_2O_3 - SiO_2 at 1760°C

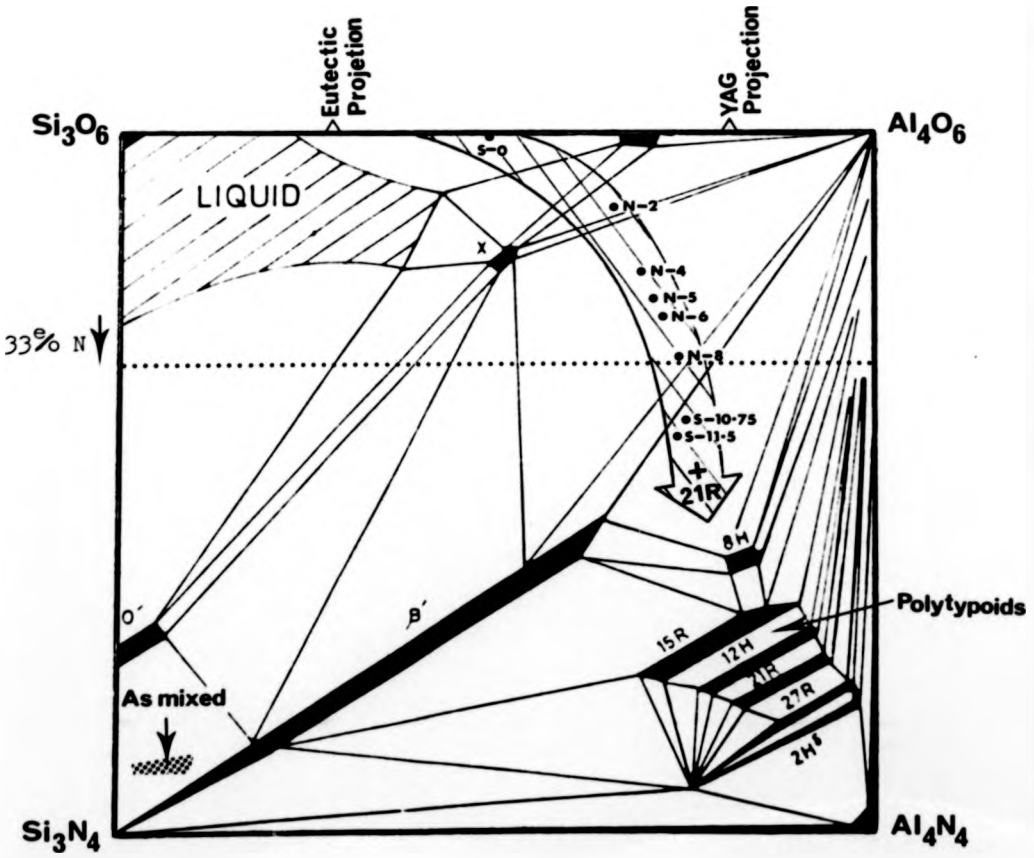

The results of calculation using Model 1A, displayed in Table 2.3, are plotted on the base plane of the Janecke prism, shown in Figure 2.5, by using projection normal to this plane. Phase relationship detail is taken from the literature [26].

FIGURE 2.7 - Projection of the possible liquid forming component onto the ternary oxide face of the Janecke prism

Addition of 21R leads to Al and N enrichment thereby restricting the volume of liquid phase formed.

Alloy	% Si	% Al	% Y
N-2	28.2	53.0	18.8
N-4	26.0	57.6	16.5
N-5	25.0	59.4	15.6
N-6	24.2	61.1	14.7
N-8	22.7	64.0	13.3
S-0	39.6	37.9	22.5
S-11.5	23.1	64.2	12.7
S-10.75	21.6	64.7	13.6

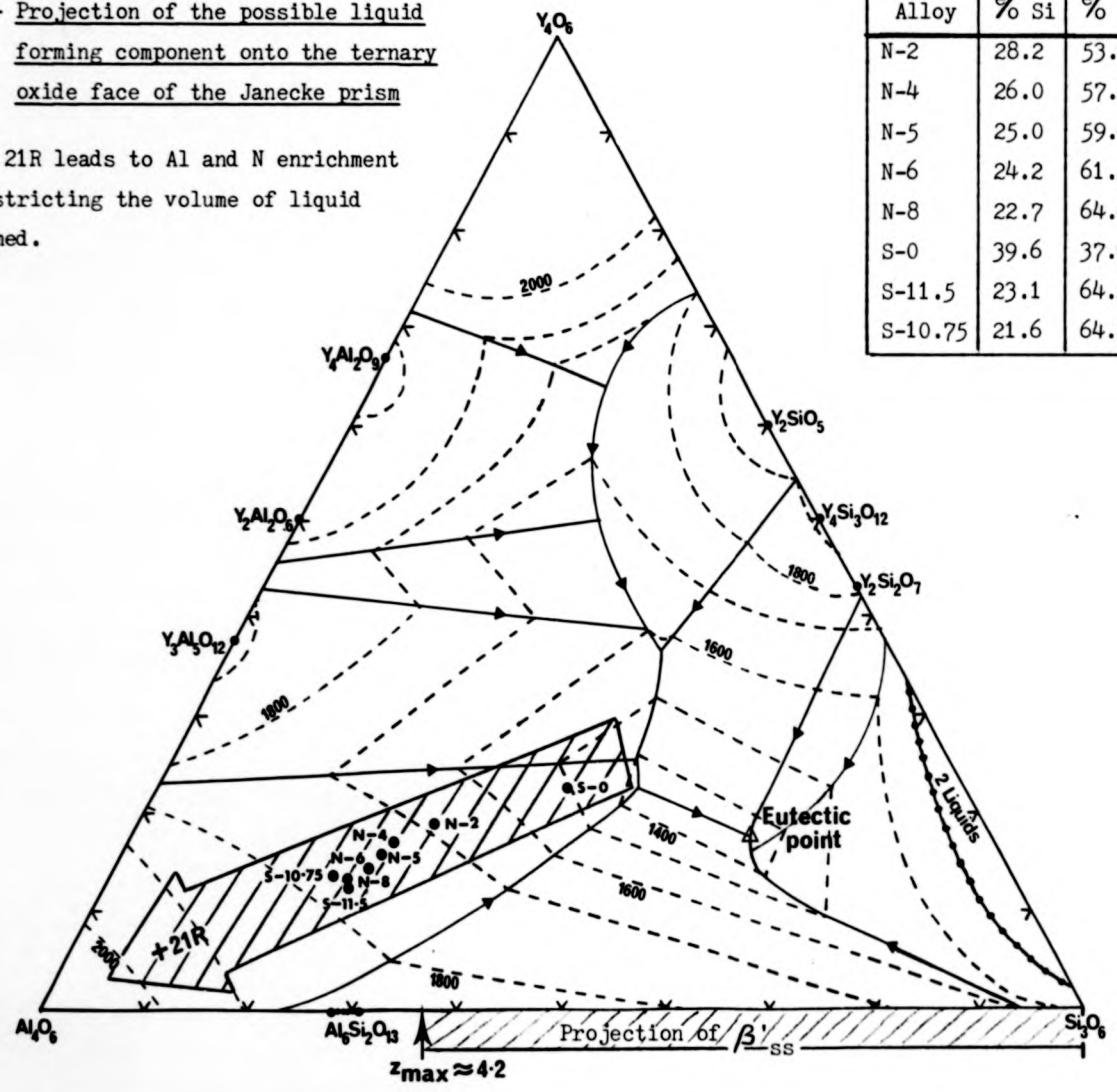

CHAPTER 3 - Behaviour of silicon nitride-based ceramics at elevated temperatures

This chapter is divided into two main sections in which the effect of elevated temperature on microstructural evolution of silicon nitride-based ceramics and creep deformation are reviewed. Since the properties of these materials are largely determined by the character of the intergranular phase some emphasis is placed upon definition of its structure/composition and resultant behaviour.

3.1 Microstructural evolution at elevated temperatures

In this sub-section the properties of Y-Si-Al-O-N bulk and intergranular glasses will be considered prior to examination of enviromental reactions occurring at the ceramic/atmosphere interface during heat-treatment.

3.1.1 Bulk effects

As previously discussed, fabrication of silicon nitride ceramics with metal oxide (M_xO_y) additives leads to formation of a composite material, the residue of the M-Si-Al-O-N sintering liquid remaining in the final microstructure as an oxynitride glass. The properties of this β' intergranular phase then determine the limit to high temperature use of the materials. Crystallisation of the glass to more refractory phases has been suggested[25] as a way of improving material properties at elevated temperatures, the products of this devitrification being compositionally dependent. Investigation of 'in situ' intergranular glass composition and properties is difficult, due to the presence of the β' phase, thus a review of studies made on bulk oxynitride glasses, of similar composition, is relevant.

(a) Glass formation and composition in the Y-Si-Al-O-N system

FIGURE 3.1
Y-Si-Al-O-N system glass forming region at 1700°C

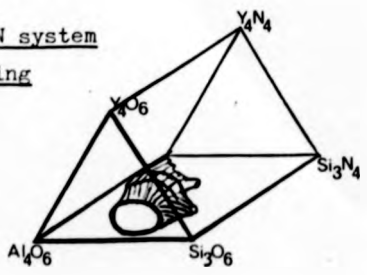

Figure 3.1 is a presentation of the glass forming region in the Y-Si-Al-O-N system at 1700°C for cooling rates of 200°C.min^{-1} [41]. Although liquids may be formed outside the indicated volume they tend to devitrify on cooling, and

since the post-sinter cooling rates of Syalon Ceramics are expected to be lower then $200^{o}C.min^{-1}$ the relevant glass forming region is expected to be slightly smaller resulting in a smaller range of intergranular glass compositions. With increasing substitution of oxygen by nitrogen to ~10 %N the range of glass forming compositions widens. Further increases in nitrogen content cause a contraction and simultaneous shift to more aluminium rich compositions. The compositions of glasses so far studied contain nitrogen in the range $0 \rightarrow 15\%$ with reported[47] formation of glass with a limiting composition $Y_{15}Si_{15}Al_{10}O_{45}N_{15}$ (ie. ~33% N).

(b) Glass structure

The structure of inorganic oxide (M_xO_y) glasses is usually discussed with reference to the Random Network Theory[48] in which the M^+ ion coordination number and M-O bond length are considered to be very similar to those in a corresponding crystalline species, providing short range order. Slight variations in M-O-M bond angles (~10%) prevent long range ordering and result in formation of a random network. Three classes of oxide may be identified:-

(1) Network forming oxides; which can form continuous three-dimensional networks eg. SiO_2,

(2) Network modifying oxides; which cannot form continuous three-dimensional networks eg. Na_2O,

(3) Intermediate oxides; which cannot form a glass alone but may take part in the network of another glass former eg. Al_2O_3.

The role that a given oxide is expected to play in a glass structure may be characterised by reference to the ionic field strength, F, of the cation:-

$$F = z/r^2$$

where, z = valency and r = ionic radius of the cation.

F may be considered a measure of the cations ability to attract electrons and form a covalent bond with the O^- ion, thereby structuring a network. Thus oxides characterised by high values of F may be considered as network formers, low values of F imply a modifying oxide and intermediate values and intermediate oxide, see Table 3.1.

Addition of a modifying oxide to an SiO_2 random network results in a structural change such that non-bridging oxygen ions are formed and the modifying cations rest in interstices producing electroneutrality.

Upon addition of the intermediate oxide Al_2O_3 to vitreous

SiO_2 both Al^{3+} and Si^{4+} play a role in the network and charge balance may be maintained by the presence of an extra cationic charge on an alkali metal ion accomodated in an interstice. Glasses formed in the SiO_2-Al_2O_3-Y_2O_3 system may be described by this model with Y_2O_3 playing a modifying role.

TABLE 3.1 - The structural role in glass of selected cations

Ion	r(Å)	$F = z/r^2$	Structural role in glass
B^{3+}	0.20	75.0	
Si^{4+}	0.41	23.8	Network formers
Ge^{4+}	0.53	14.2	
Al^{3+}	0.50	12.0	Intermediates
Ti^{4+}	0.68	8.7	
Mg^{2+}	0.65	4.7	
Y^{3+}	0.89	3.8	Modifiers
Ca^{2+}	0.99	2.0	

FIGURE 3.2 - The effect of nitrogen addition to an SiO_2 random network

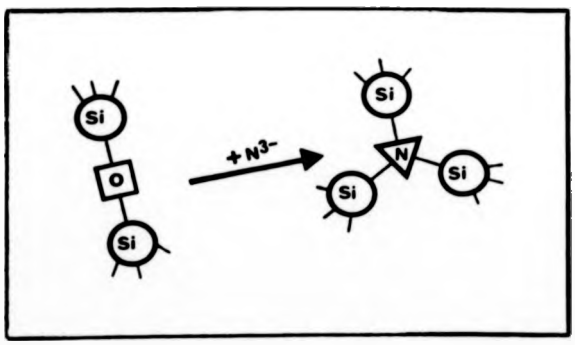

- see text below.

Oxynitride glasses may be considered using the Random Network Model (RNM). Infrared spectroscopy data[49] suggests that such glasses contain primarily Si-O and Si-N bonds with very few Al-N bonds, which implies that N^{3-} ions enter the network by linking to the Si^{4+} cations. This is expected to lead to a more highly cross-linked structure than found in pure oxide glasses since each N^{3-} ion must link three Si^{4+} ions (cf. O^{2-} links two Si^{4+} ions) as shown in Figure 3.2.

A schematic two-dimensional representation of the Si-M-O-N network may then be shown as illustrated in Figure 3.3, addition of Al^{3+} ions further complicating the structure as described above for oxide glasses.

FIGURE 3.3 - A two-dimensional representation of the Si-M-O-N glass network

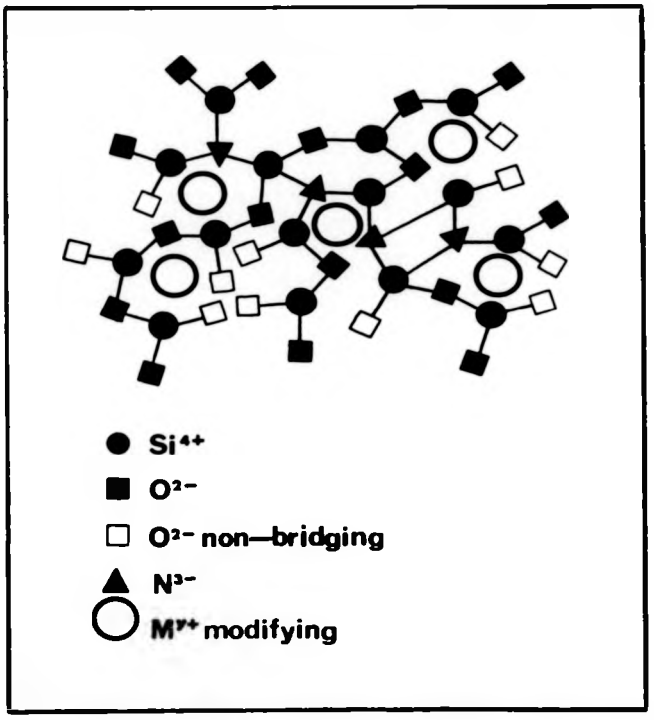

One approach[50] to characterising the network structure of silicate glasses defines the following quantities:-

R = average number of oxygen ions per network forming ion,

Y = average number of bridging oxygens per polyhedron,

X = average number of non-bridging oxygens per polyhedron.

For simple silicates, with a network of tetrahedral units and Si^{4+} as the only network forming ion, the structure is characterised by the equations:-

$$R = O/\text{network former} = {}^{a}\!/\!_{o}\ O/{}^{a}\!/\!_{o}\ Si,$$

$$Y = 8 - 2R,$$

$$X = 2R - 4.$$

The quantity Y determines the 'degree of internal coherence of the network' and allows comparison of expected physical properties (eg. a higher

value for Y implies higher viscosity due to increased bridging of the network). A value of R in the range 2.25-2.75 may indicate formation of a glass network as determined empirically for a number of multicomponent oxide glass compositions[51].

Application of this approach to oxynitride glasses is possible[51] using the structure described in Figure 3.3, where tetrahedral units, of O^{2-} and N^{3-} ions surrounding an Si^{4+} ion, link randomly in a highly cross-linked network. Modified network parameters for Y SiAlON glasses, with $\frac{2}{3}$ of Al^{3+} ions situated in the network* and $\frac{1}{3}$ occupying modifying sites, may be defined as follows:-

$$R' = (\text{a\% O} + \text{a\% N}) / (\text{a\% Si} + \tfrac{2}{3}.\text{a\% Al}),$$

$$Y' = 8 - 2R',$$

$$X' = 2R' - 4.$$

from which, the following is evident:-

(1) Since $2N^{3-}$ substitute for $3O^{2-}$ in the network, a higher a% N implies a lower value of (a% O + a% N) which produces an increase in Y'.

(2) An increase in network forming ions, especially Si^{4+}, and corresponding decrease in modifying ion content leads to an increase in Y'.

Thus, for a given temperature, this quantitative structural model predicts an increasing viscosity with nitrogen content in agreement with experimental observation. Values of Y', for bulk oxynitride glasses currently prepared, fall in the range 2.1-3.7, for Y'<2 a glass composition will not form three-dimensional links, instead the tetrahedral units form chains. Values of R' lie in the range ~ 2.0-2.96.

(c) Properties of bulk oxynitride glasses

Various physical and electrical property data are available in the literature for a range of oxynitride glass compositions[52], [53],[54],[55],[40],[41] and only trends will be considered here. It is generally agreed that, for MSiON and MSiAlON glasses, an increase in the N/O ratio leads to an increase in ease of glass formation, viscosity (η), glass transition temperature (T_g), density (ρ), hardness, fracture toughness, refractive index and dark colouration. Such an increase also leads to a decrease in eutectic (liquidus) temperature (T_E), and thermal expansion coefficient. All of these property changes are consistent with the qualitative model of N^{3-} substituting for O^{2-} in the glass network, increasing the amount of cross-linking within the structure.

* $\frac{2}{3}$ Al^{3+} empirically found to give best fit.

(d) Crystallisation of silicate glasses

Comprehensive treatment of classical nucleation and crystal growth theory are available in the literature[56],[57],[58],[59], and the equations describing the kinetics of these processes will not be derived here but are presented in Figure 3.4 together with typical temperature-rate curves defined by them. All symbols used in the equations, and in the following discussion, are presented below the figure.

During the cooling of silicate melts, glasses may be formed if the accompanying increase in viscosity reduces ionic mobility to a value below that necessary to enable the structural rearrangement associated with crystal lattice formation. Thus silicate glasses are highly viscous, although addition of modifying oxides weakens the network structure increasing the ease of structural rearrangement.

Re-heating of such glasses, to temperatures in the range above the glass transition temperature, T_g, where atomic mobility is enhanced, allows formation of unstable crystal 'embryos' which may become stable crystal nuclei on exceeding a size denoted by the critical radius $r^* = (2\sigma) / (\Delta f_v)$ corresponding to a maximum change in free energy ΔF^*.

The Homogeneous Nucleation rate, I, depends upon the degree of undercooling, ΔT, below the equilibrium melting temperature, T_m. For small values of undercooling the first exponential term in the equation for I dominates and I increases rapidly due to the change in Δf_v with temperature. At lower temperatures (larger undercooling) I is dominated by the second exponential term, which describes the rate at which atoms move across the glass/crystal interface. Thus a maximum nucleation rate is observed at an intermediate temperature, T_I.

Heterogeneous nucleation may be catalysed at the glass free-surface, at defects (porosity etc.) or other pre-existing surfaces. If the interfacial energy between the crystallising phase and the heterogeneity is lower than that between the crystallising phase and mother glass, σ, then the free energy for nucleation, ΔF^*, is reduced. Since the volume free energy term, Δf_v, and activation energy for diffusion, Q, are not changed, the general shape of the nucleation curve remains unchanged. Thus the effect of heterogeneous nucleation is to reduce the degree of undercooling necessary for nucleation and the curve is shifted to higher temperatures where crystal growth is favoured.

The crystal growth rate, U, accelerates with increased undercooling, ΔT, from a value of zero at T_m, due to amplification of the bulk free energy of crystallisation, ΔG. However, the associated

FIGURE 3.4

Typical relationship between Nucleation rate, I, and Crystal Growth rate, U.

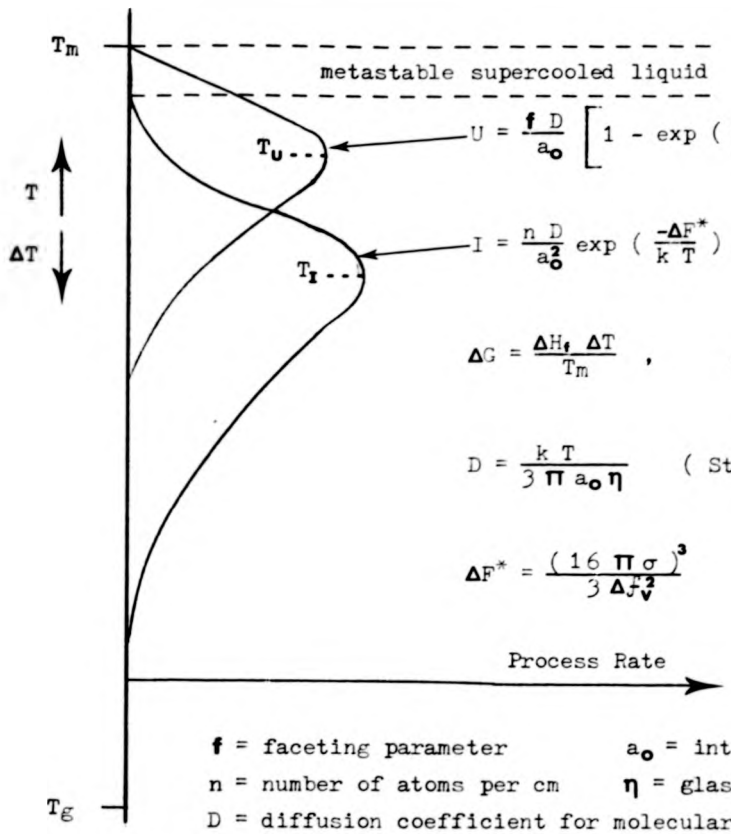

f = faceting parameter a_o = interatomic distance

n = number of atoms per cm η = glass viscosity

D = diffusion coefficient for molecular transport across the glass/crystal interface

Q = activation energy for molecular transport across the glass/crystal interface

T_m = equilibrium melting temperature

ΔT = degree of undercooling

ΔF^* = change in free energy on forming a spherical crystal nucleus in the glass

ΔG = bulk free energy of crystallisation

ΔH_f = heat of fusion

Δf_v = change in free energy per unit volume due to the glass to crystal transformation

σ = energy per unit area between the glass and crystal phases

increase in viscosity exerts a dominating influence at temperatures below a temperature, T_U, and this results in a decreased growth rate at larger undercoolings. Two factors may be important to crystal growth:-

(1) the rate of glass to crystal transformation,

(2) the rate at which latent heat, produced on transformation, can flow from the glass/crystal interface.

Since I and U are low in viscous silicate melts, crystal growth must be an almost isothermal process. However residual glass ions not participating in the crystal structure may be segregated at the transformation boundary causing a change from interface controlled growth to diffusion control, decreasing the already slow growth rate. Under these conditions cellular transformation mechanisms may come into operation.

(e) Crystallisation products of bulk oxynitride glasses

The heat treatment, to affect crystallisation, of bulk oxynitride glasses is more difficult than that of their plain oxide analogues. Heating of high N/O ratio glasses in oxidising atmospheres is observed to lead to vigorous frothing[60],[61], which is most probably due to evolution of nitrogen, and thus protective nitrogen atmospheres are required. Decreased ionic diffusivity, due to increased T_g and viscosity, retard nucleation and growth, and, in combination with this effect, the lower eutectic temperature, T_E, leads to a decrease in the range of undercooling (between T_g and T_E), in which nucleation and growth may occur.

In a study of crystallisation of bulk Y-Si-Al-O-N glasses using XRD and Differential Thermal Analysis (DTA) temperatures above 1000°C were found to lead to devitrification[62]. Isothermal heat-treatments at 1000°C, 1100°C and 1200°C showed a general trend to formation of $Y_2Si_2O_7$ as the predominant crystalline phase at longer times and higher temperatures. Mixtures of up to five crystalline species were identified at intermediate temperatures including yttrium silicate, yttrium aluminium silicates and nitrogen apatite ($Y_{10}Si_6O_{24}N_2$). The formation of $Y_2Si_2O_7$ as the ultimate crystalline species implies enrichment of nitrogen in the residual glass, crystallisation nucleating initially on the specimen surface and then in the bulk as a second stage process.

In another study a glass of composition $Si_{15}Al_{10}Y_{15}O_{45}N_{15}$ devitrified at 1100°C to 'B phase' (Y_2SiAlO_5N) which lies on the solid solution line intermediate of N-α-Wollastonite ($Y_2Si_2O_4N_2$) and YAP* ($Y_2Al_2O_6$). After heating a relatively YN rich specimen for 15hrs. at

* (YAP) Yttrium Aluminium Perovskite.

1250°C XRD indicated crystallisation of $Y_2Si_2O_7$ as the major phase with minor amounts of YAG ($Y_3Al_5O_{12}$)[55].

ZrO_2 has been used as a nucleating agent in Y-Si-Al-O-N bulk glasses and crystallisation products identified after heat-treatment at 1100°C for various times included YAG, $Y_2Si_2O_7$ and Y_2SiO_5[63].

(f) Crystallisation of the intergranular oxynitride glass in Si_3N_4-based ceramics

Further complications may arise during heat-treatment of β-Si_3N_4 (or β') and glass composites:-

(1) Constraint provided by the rigid β or β' skeleton may allow the confined glass pockets to experience hydrostatic stresses derived by volume change upon crystallisation. The associated strain energy may then retard or completely suppress crystallisation, especially in the smaller glass pockets, thereby modifying behaviour such that four grain pockets and other large glass pools become favoured nucleation sites with limited growth into the smaller three-grain junctions[64].

(2) There is the possibility of chemical interaction between the β or β' phase and the surrounding matrix in regard of Si, Al, O and N atoms.

(3) Any impurities present, eg. Fe and Ca, introduced either as part of component powders or accidentally during fabrication, must become highly concentrated in the intergranular glass, thereby affecting its crystallising behaviour[42].

Thus, although crystallisation studies in bulk M-Si-Al-O-N glasses are recognised as useful, their relevance to behaviour of Syalon Ceramic intergranular glass may be limited.

In one investigation of HPSN two materials were studied[65] using TEM/EDAX techniques, one with 5w% Y_2O_3 + 2w% Al_2O_3 and the other with 5w% Y_2O_3 + 5w% Al_2O_3 as sintering aids. Amorphous phase of projected near-eutectic trough composition with Fe, Ca, Cr and other impurities was identified. Also reported, was the existence of a crystalline yttrium nitrogen mellilite phase ($Y_2Si_3O_3N_4$) which was found to exhibit solubility for Al^{3+} to the extent 44% Si_3N_4, 49% Y_2O_3, 7% Al_2O_3. The presence of the amorphous phase at almost all β'-β' and β'-mellilite boundaries, in the form of a layer as thin as 2nm, was demonstrated using dark field and lattice imaging techniques.

An earlier study of Syalon Ceramics[38] identified devitrification of a near-eutectic composition glass, to YAG ($Y_3Al_5O_{12}$), after heat treatments at 1400°C for 5 hrs. Some solution of silicon in the YAG was demonstrated and re-distribution of the β'/matrix compositional balance, with Al_2O_3 substitution being decreased from $z \approx 0.44$ to $z \simeq 0.40$, was reported. The latter effect was also noted in a seperate study[66] and ascribed to epitaxial crystallisation of β-Si_3N_4, from the initially glassy matrix phase, onto the existing β' grains. Since cored β'/β grains have not been observed, the process must occur at a rate comparable with that for diffusion, leading to homogeneity, within the β' grains.

3.1.2 Surface effects

The importance of this section lies not in the immediate effects of atmospheric interaction with the ceramic surface, but in the bulk compositional changes induced by diffusion through the inter-β' channels.

(a) Heat treatment of Si_3N_4 ceramics under oxidising conditions

Oxidation of materials may occur in an 'active' manner, characterised by specimen weight loss due to loss of material to the surroundings (usually by generation of gaseous oxidation products), or in a 'passive manner in which specimen weight gain is experienced by formation of a solid oxide product.

Passive oxide scales may be termed 'protective' if they impede the oxidation reaction by presenting a diffusion barrier between the reacting species, or 'non-protective' if the reacting gas can easily reach the substrate through pores, cracks etc. The formation of such scales has been extensively modelled and a comprehensive review is available in the literature[67].

(1) Initial reaction at the Si_3N_4/atmosphere interface

Under normal oxidation conditions Si_3N_4-based ceramics are observed to undergo 'passive' oxidation and the initial reaction with β'-SiAlON phase has been described[68]:-

$$Si_{6-z}Al_zO_zN_{8-z} + (6 - \tfrac{3}{4}z)\,O_2 \rightarrow (6-z)\,SiO_2 + z/2\,Al_2O_3 + (8-z)/z\,N_2\uparrow$$

The aluminosilicate layer so formed may be considered 'protective', necessitating inward oxygen diffusion for further reaction, but nitrogen bubbles forming at the oxide scale/substrate interface may lead to

local areas of non-protective scale. Any intergranular phase cross-sectioned in the reacting ceramic surface must be preferentially oxidised and will decrease the viscosity of the aluminosilicate layer.

(2) Further reaction involving β' boundary transport

A diffusion gradient is set up between the initially formed silica rich surface layer and the bulk intergranular phase resulting in migration of cations from the bulk to the scale, either along β'/β' boundaries in HPSiAlON or through the matrix glass phase in bi-phase ceramics[69],[70],[71]. Concurrent inward diffusion of oxygen, and possibly outward diffusion of nitrogen*, also occurs, but the cation out diffusion is usually considered rate controlling and further oxidation is generally described by parabolic kinetics as represented by the classical diffusion equation:-

$$w^2 = (\Delta w/s)^2 = kt + C$$

$$\text{where } k = k_o.\exp(-E_a/RT)$$

in which, w = weight gain at time t,

Δw = change in weight,

s = specimen surface area,

k = parabolic rate constant,

C = a constant, accounting for the effect of an initial non-parabolic stage,

k_o = a constant,

E_a = activation energy.

(Low values of activation energy have been taken to imply rate control by inward migration of oxygen, and high values to imply rate control by cation out-diffusion.)

The cationic diffusion gradient is usually maintained by formation of crystal silicate phases in the oxide scale.

(3) Effect of crystal species at β' boundaries

Non-parabolic behaviour may result from degradation of oxynitride phases, which form at intermediate temperatures (~1000°C), and poor oxidation resistance, with linear kinetics, is exhibited by materials containing any of the quaternary compounds:-

$Y_{10}Si_7O_{23}N_4$, $YSiO_2N$, $Y_4Si_2O_7N_2$ and $Si_3Y_2O_3N_4$[72],[73].

Compositions hot-pressed in the compatibility field Si_3N_4 - Si_2N_2O - $Y_2Si_2O_7$ of the Si_3N_4 - Y_2O_3 - SiO_2 system, in which formation of such oxynitride phases is avoided, show relatively good oxidation resistance.

* It has been suggested that N^{3-} diffusion may accompany cation diffusion from the bulk maintaining charge balance[70].

Formation of O' phase (Si_2N_2O with some aluminium substitution) has been observed[27], produced by partial reaction between β' and intergranular glass depleted in yttrium and aluminium by oxidation. This effect has also been noted in precrystallised β'/YAG composites, degradation of YAG occurring by formation of a diffusion couple with the SiO_2 rich surface oxide scale resulting in formation of a near-eutectic glass at temperatures exceeding ~1300°C. Such subscale reactions lead to generation of a β'/O' composite layer which may extend to thicknesses of a few hundred μm after long heat-treatment (~1000hrs.) at ~1300°C. Enhanced oxidation resistance is displayed by materials sheathed with this O' containing protective layer, (N.B. the limiting temperature for use of HP Si_2N_2O / Y_2O_3 engineering ceramics has been defined as ~1600°C in air [74]).

(4) Oxide scale morphology

Variations in the composition and volume fraction of the intergranular phase, as well as temperature and time of oxidation, are expected to affect the composition and morphology of the oxide scale and thus change the oxidation rate. Recent work[75] considering the oxidation of HPSN prepared with Y_2O_3 and SiO_2 sintering additive has led to the following conclusions:-

(1) The ratio $\Sigma M_1/Y$ *, of the oxide glass, decreases as the oxidation temperature increases due to the relatively high yttrium diffusion coefficient in the intergranular phase.

(2) The oxide glass is highly viscous and crystallisation of $Y_2Si_2O_7$ occurs due to oversaturation of yttrium and its low mobility relative to that in the intergranular phase.

(3) The growth morphology of the $Y_2Si_2O_7$ varies with oxidation temperature, needle-like crystals forming in preference to plate-like crystals as temperature is decreased.

(4) Further crystallisation of $Y_2Si_2O_7$ may occur on slow cooling, the morphology may be either rhombohedral or, if the glass is more viscous and oversaturated in yttrium, dendritic.

At temperatures below ~1225°C Yttrialite (an impurity containing form of α-$Y_2Si_2O_7$) is the major phase detected, apart from βSi_3N_4. Above this temperature other forms of $Y_2Si_2O_7$ predominate. This observation

* M_1 = Metal cations derived from the intergranular phase, commonly Mg, Al, Fe, Ca etc..

is in agreement with previous data concerning the structure of $Y_2Si_2O_7$[76]:-

$$\alpha \xrightarrow{1225 + 10^{\circ}C} \beta \xrightarrow{1445 + 10^{\circ}C} \gamma \rightleftharpoons^{1575 + 10^{\circ}C} \delta$$

(hexagonal) (monoclinic)

(b) Heat treatment of Si_3N_4 under reducing atmospheres

Heat treatment at low oxygen partial pressure under an argon atmosphere was found to lead to disappearance of the intergranular glass phase and reduction of Si_2N_2O content in HPSN with MgO additive[77]. Subsequent heating in air produced an oxide rich in impurity and additive cations proving that they were not lost from the system during reducing heat-treatment. After heating under argon, the material was shown to be extremely friable due to the large porous volume at β-Si_3N_4 grain boundaries previously occupied by intergranular glass, and subsequent oxidation produced SiO_2 in the material due to reaction of gaseous oxygen with Si_3N_4 through the porous cavities. It was noted that a better description of the process may be 'active' oxidation of Si_3N_4 and Si_2N_2O under the prevailing heat-treatment conditions, the intergranular phase reacting more easily than these crystalline phases and therefore being removed more quickly.

3.2 Creep deformation of silicon nitride and its measurement

In this section creep mechanisms elucidated for high temperature sub-critical deformation of polycrystalline ceramics are briefly reviewed, and those applicable to HPSN and HPSiAlON materials discussed. Only material relevant to the creep of Syalon Ceramics is considered and for a full appreciation of creep processes the literature must be considered.

The various methods available for characterisation of creep behaviour are also considered, but, for the sake of brevity, the derivation of equations has not been included and may be found in the referenced works.

3.2.1 Creep deformation of silicon nitride ceramics at elevated temperature

Creep of a material may be defined as time-dependent plastic deformation which occurs, especially at elevated temperatures, upon application of loads producing stress very much lower than the fracture stress.

A comprehensive review[78] describing the various mechanisms postulated for creep of structural ceramics is available, and a more recent review[79] enables comparison of the theoretical creep mechanisms with experimental data gleaned from the literature. The reader is directed to these sources for reference.

Most high temperature creep mechanisms predict a steady state creep rate, and are described by the general equation for creep:-

$$\dot{\epsilon} = \frac{ADGb}{kT} \cdot \left(\frac{b}{d}\right)^m \cdot \left(\frac{\sigma}{G}\right)^n$$

in which $D = D_o.\exp(-Q/RT)$

where, A = a dimensionless constant,
D = the appropriate diffusion coefficient,
G = the shear modulus,
b = the Burgers vector,
d = the grain size,
m = the inverse grain size exponent,
n = the stress exponent,
D_o = a frequency factor,
Q = the activation energy for the diffusion process,
k, R and T have their usual meanings.

For polycrystalline materials identification of the rate-controlling creep mechanism is made by reference to the values of n, m and Q derived experimentally. Creep of silicon-nitride based materials is usually described by intergranular mechanisms and thus the state and properties of the grain boundaries becomes important:-

(1) Grain boundaries separated by viscous layers

If the viscous layer is thick, adjacent grains and boundary asperities offer no resistance to the shearing process and a Newtonian-viscous strain rate is recorded;

ie. $\dot{\epsilon} \propto \sigma^n$ where n = 1.

If the viscous layer is thin, boundary irregularities may lead to non-viscous behaviour, ie. n > 1.

(2) Grain boundaries with no second phase

Since elastic distortion of grains is insignificant in the case of Si_3N_4 ceramics, grain movement is described by diffusion controlled, or cavitation accomodated, grain boundary sliding mechanisms.

A study of HPSiAlON[34] ceramics showed that material fabricated with a small amount of residual glass phase crept with a stress exponent n = 1.5-1.6 and an activation energy Q = 496 $KJmol^{-1}$. Microstructural investigation led to identification of a boundary sliding mechanism, accomodated partially by diffusion and partially by cavitation at triple junction glassy-phase residues, in this material.

In the same study another HPSiAlON ceramic, fabricated with only segregated impurity ions at grain boundaries, exhibited creep characterised by n = 1 and activation energy varying in the range 296-455 $KJmol^{-1}$. A pre-oxidised specimen (1350°C/250hrs.) crept with n = 1 and Q = 830 $KJmol^{-1}$ and it was proposed that oxidation removed the segregated intergranular impurity ions to the oxide scale, changing the creep mechanism from one of grain boundary diffusion (Coble) to one of lattice diffusion (Herring-Nabarro) rate control.

In another study a series of HPSN ceramics fabricated with MgO additive was produced with variable grain boundary glass volumes[80]. Viscoelastic effects responsible for primary creep (and strain recovery upon unloading) were explained in terms of grain boundary sliding accomodated by elastic strain arising at asperities on β-Si_3N_4 grains. Again the effects of the oxidation reaction were noted, the continual removal of the intergranular glassy phase, to the scale, improving creep resistance. Thus, a truly steady state secondary creep stage was not observed, but values of stress exponent, n, were derived in the range $n \approx 0.9\text{-}2.0$, during "apparent steady state" creep. Compositions furthest from the ternary eutectic and therefore of lower glass content exhibited $n \lesssim 1$ diffusional creep behaviour, with very little cavitation, while specimens with higher glass contents exhibited $n \lesssim 2$ behaviour with large amounts of cavitation.

The equation:-

$$\varepsilon_{cav} = \left[\left(1 - \frac{V_1^2 \sigma t}{\eta}\right)^{-1/4} - 1\right]\frac{V_1}{3}$$

was presented, where, ε_{cav} = creep strain due to cavitational mechanism,

V_1 = volume of grain boundary liquid,

σ = applied stress,

η = liquid viscosity,

t = time,

from which it can be seen that the relation between cavitational strain

and applied stress cannot be expressed by a simple power law. Thus for materials dominated by both diffusional and cavitational creep, power law analysis of the apparent steady state condition, as a function of stress, would result in an apparent stress exponent, $n > 1$. This is consistent with experimental values which range between 1 and 3.

Also presented, assuming diffusion along viscous boundary phase, was the equation:-

$$\varepsilon_{diff} = \frac{8\Omega^{2/3}.CV_1\sigma t}{d^2}$$

where, ε_{diff} = creep strain due to diffusional mechanism,
Ω = Molar volume of the diffusing species,
C = Molar fraction of the diffusing species,
d = the grain size.

Combination of the equations for ε_{cav} and ε_{diff} enabled explanation of the experimental data and it was shown that cavitation creep dominates at high volume fraction of glass, large stresses, lower viscosities and long test periods. Thus a material can be dominated by diffusional creep at low stress levels and by cavitational creep at high stress levels.

3.2.2 The measurement of creep from ceramic specimens

Determination of true creep behaviour requires accurate application of stress with a uniform distribution. Testing at high temperatures in the uniaxial tensile mode has proven difficult due to problems in gripping of specimens and premature failure at specimen surface flaws.

The method of three- or four-point bending has often been used to assess the creep properties of ceramics[79] due to the ease of specimen preparation and load application. However the stress distribution generated during bending is inhomogeneous[81], Sub-critical Crack Growth (SCG) from flaws on the tensile face may lead to premature failure and analysis is limited by the assumption that the neutral axis lies at the centre of the beam under test[82] (this is only the case when the stress exponent, n = 1). Most of the measurements reported in this thesis were made by loading in the four-point bend mode.

A third method, enabling uniform application of load, is uniaxial compression, however the high compressive strength of ceramics

leads to inaccuracy in measurement of low creep strains. Some measurements of uniaxial compressive creep properties were obtained from selected ceramics and the results are reported in Chapter 6.

Experimental determination of creep parameters requires measurement of load point movement as a function of time and the calculation of stresses and strains from such data is dealt with next.

(a) Calculation of stresses and strains in four-point bend creep tests

Derivation of the relationships presented will not be discussed and is available elsewhere[82].

The stress in the outer fibre of a four-point bend specimen, σ_{max}, is found via the relation:-

$$\sigma_{max} = \frac{(L - a)\ (2n + 1)\ P}{nbh^2}$$

where, L = the span between the lower loading points (30mm),
a = the span between the upper loading points (15mm),
n = the stress exponent,
P = the applied load,
b = the specimen breadth ($\sim$3mm),
h = the specimen height ($\sim$3mm).

The strain in the outer fibre of a four-point bend specimen ε_{max}, is related to the load point deflection, Y_L, measured by the transducer, via the relation:-

$$\varepsilon_{max} = \frac{2h\ (n + 2)\ Y_L}{(L - a)\ [L + a\ (n + 1)]}$$

A knowledge of n is therefore necessary for determination of σ_{max} and ε_{max} and this is found via the relationship:-

$$\log \dot{Y}_L = n.\log P + C$$

Thus a plot of log $\dot{Y}_L$ versus log P leads to determination of n by measurement of the slope, subsequent calculation of σ_{max} and ε_{max} enables comparison of results with other data in the literature on a plot of $\ln \dot{\varepsilon}$ versus $\ln \sigma$.

(b) Calculation of stresses and strains in uniaxial compression creep tests

Direct determination of stress, σ , is possible via the relation:-

$$\sigma = Pg / ab$$

where, P = applied load,

g = acceleration due to gravity = 9.812 $m.s^{-2}$,

a = specimen width ($\sim$3mm),

b = specimen breadth ($\sim$3mm).

Determination of strain is made via the relation:-

$$\varepsilon = \Delta h / h$$

where, Δh = change in height of specimen,

h = original height of specimen ($\sim$5mm).

Compared with the experimental errors made in assessing creep rates and specimen dimensions, the change in stress, due to increase of specimen cross section with increasing strain and time, is negligible and can be ignored, eg. at $\varepsilon = -5\%$, $\Delta\sigma \approx -1.8\%$.

CHAPTER 4.- The microstructural characterisation of Syalon Ceramics

In order to characterise the microstructure of each ceramic alloy a progressive approach was employed. Initial analysis utilised the 'macro-sampling' techniques of density measurement, X-ray diffractometry, (XRD) and optical (light) microscopy in an effort to assess relative variations in the degree of densification, major phase content and relative homogeneity of the materials. Further investigation of selected ceramics, using electron optical apparatus equipped with an x-ray microanalysis facility, provided microanalytical data pertaining to the composition and distribution of both the major β' Si - Al - O - N phase and intergranular Y - Si - Al - O - N 'matrix' phases present. Some quantification of oxygen and nitrogen contents was possible using the technique of energy loss spectroscopy.

This chapter is presented in three parts, the first describes the experimental methods used in the microstructural characterisation, and the second is a presentation of results defining various aspects of the microstructural state of selected ceramic alloys in the 'as sintered' condition. The third section is a discussion relating all the results obtained on both macro- and micro- scales to the microstructure and its development in the various 'Syalon Ceramics' investigated. The characterisation of heat-treated ceramics is described in Chapter 5.

4.1. Experimental techniques employed in microstructural characterisation

4.1.1 Density measurement

Due to the small size of the samples supplied, it was only possible to determine approximate values for the density of selected ceramic alloys. An Archimedian technique was employed with de-ionised water, recently boiled and cooled to room temperature, as immersion fluid. Specimens of mass ~1g were polished to a 6μm finish, cleaned in an ultrasonic bath of acetone, dried and supported in a noose of Cu wire (of predetermined mass ~0.008g). Using an Oertling Model R20 balance, capable of determining masses to 0.1mg, the specimens were weighed firstly in air and secondly in the immersion fluid. To prevent errors arising due to the presence of bubbles, specimens were soaked in methanol and washed in de-ionised water prior

to wet weighing, thereby ensuring that all surfaces were fully wetted by the immersion fluid. The fluid level was adjusted, to an indent at the centre of the copper wire, for each determination of the wet weight, and the water temperature recorded so that a correction to the density of the immersion fluid could be applied from Table 4.1

Repeated measurements of density on seperate occasions showed that determinations on a given specimen were in agreement ± 1mg. However the density measurements cannot be claimed to be representative of whole billets since the density of only one sample from each billet was determined.

TABLE 4.1 - The density of pure water as a function of temperature

T °C	16	17	18	19	20	21
ρ g.cm^{-3}	0.9979	0.9977	0.9976	0.9974	0.9972	0.9970

(CRC Handbook)

Densities were calculated using the formula:-

$$\rho_{syalon} = \frac{W_a}{W_a - W_w} \cdot \rho_w$$

where, W_a = Weight of Syalon Ceramic specimen in air
= (dry weight of specimen + wire) - (dry weight of wire),

W_w = weight of Syalon Ceramic specimen in water
= (wet weight of specimen + wire) - (dry weight of wire) + $\left(\frac{\text{dry weight of wire} \cdot \rho_w}{2 \cdot \rho_{Cu}}\right)$,

$\rho_{Cu} \approx 8.9\ g.cm^{-3}$

4.1.2 X-ray diffractometry

A standard Philips horizontal scanning diffractometer Model PW 13800/00 was correctly aligned and used to characterise the Bragg diffraction of x-rays, generated in a copper target at 40kV and 35mA, by solid flat Syalon Ceramic specimens polished to a 6μm finish. A nickel filter was used to remove the Cu$K\beta$ contribution from the incident x-ray beam, leaving only $K\alpha_1$ and $K\alpha_2$ components of mean wavelength λ = 1.5405 Å. It would have been preferable to use a chromium target (generating x-rays of longer wavelength λ = 2.291 Å) which would expand the diffraction pattern obtained and, despite decreasing the range of $2\theta^{\circ}$ scanned, would allow greater resolution and accuracy in

the data obtained. However this facility was not available. A scan-speed of $0.25^{\circ}2\theta.min^{-1}$ was used and a chart trace of the diffraction pattern was recorded at $10mm.min^{-1}$ on a chart recorder.

Extensive treatments of the theory and application of x-ray Bragg diffraction are available in the literature[83], and the subject will not be reviewed here, however it should be noted that the geometrical properties of the x-ray spectrometer modify a pure diffraction maximum in three ways:-

(1) the maximum is rendered asymmetrical,

(2) the maximum is broadened,

(3) the maximum is shifted in position from its theoretical angle of deviation, $2\theta^{\circ}$, to a position $2\theta^{\circ} - \Delta 2\theta^{\circ}$.

The x-ray spectrometer is therefore a useful tool for qualitative work such as the identification of crystalline species present in a specimen, but quantitative work, eg. accurate determination of crystal lattice parameters, requires the use of other apparatus such as the Guinier diffraction camera.

Analysis of the diffraction patterns obtained from specimens of selected ceramic alloys enabled approximate determination of interplanar spacings, d_{hkl}, in the specimens via the Bragg equation:-

$$n\lambda = 2d \sin\theta$$

where, n = the order of a given diffraction maximum

λ = the x-ray wavelength = 1.5405 Å for CuK_{α} radiation

θ = the Bragg angle at which the maximum is observed

By reference to the standard ASTM powder diffraction data file (eg. see Table 4.2) the major phases present in each specimen were identified.

Each diffraction pattern contains information relating to the size of the diffracting crystals present in the polycrystalline specimen it was obtained from. Determination of the crystal size will now be briefly reviewed, more detailed treatments are available in the literature[83]. On interaction with a crystal lattice destructive interference between scattered x-rays occurs in all directions except those of the diffracted beams. However, since a reduction in crystal size leads to a reduction in the number of diffraction planes present, it may also lead to incomplete cancellation of all scattered rays, and thus the breadth of each maximum is caused to increase. For the technique of powder x-ray diffraction, Scherrer[84] first related the mean crystallite dimension, D, to pure x-ray diffraction broadening, β, by

TABLE 4.2

β-Si_3N_4 X-ray Diffraction Data, Card 9-259*

Hexagonal unit cell, a = 7.603
c = 2.909

d(Å)	I/I_o	hkl	$2\theta_{Cu\ K\alpha}$
6.63	18	100	13.34
3.82	20	110	23.27
3.31	85	200	26.91
2.668	100	101	33.08
2.492	100	210	36.01
2.312	10	111	38.92
2.180	35	201	41.38
1.904	6	220	47.72
1.892	6	211	48.05
1.827	20	310	49.87
1.753	70	301	52.13
1.593	20	221	57.83
1.548	10	311	59.68
1.512	35	320	61.25
1.455	35	002	63.93
1.437	20	410	64.82
1.358	4	112	69.11
1.341	14	321	70.11
1.330	18	202	70.78
1.317	18	500	71.59
1.283	85	411	73.79
1.268	20	330	74.81
1.255	85	212	75.72
1.244	4	420	76.51
1.200	10	501	79.86
1.183	16	510	81.25
1.155	18	222	83.65

* ASTM Powder Diffraction Data File.

the equation:-

$$D = \frac{K\lambda}{\beta \cos\theta_{hkl}}$$

where, K = a constant dependent upon crystallite shape and the manner in which D and β are defined ($K \approx 1$),

β = the pure breadth of a powder reflection free of broadening due to experimental effects, and by convention is measured in radians in terms of $\Delta 2\theta$ rather than $\Delta\theta$,

θ = the principle angle at which the reflection occurs.

Uncertainties in both K and β determine the accuracy with which the Scherrer equation may be applied. K is variable in the range $0.70 < K < 1.70$ and depends on such factors as:-

(1) the crystallite shape,
(2) the indices of the reflecting planes,
(3) the way in which β is defined,
(4) the definition of D (eg. D_{hkl} = the effective thickness perpendicular to the reflecting planes hkl).

Scherrer has shown[34] that if β is defined as the half-maximum line breadth and D is defined as D_{hkl} then $K \approx 0.9$ and there is little dependence of K on crystallite shape. If an appreciable portion of the specimen has crystallites of mean dimension $< 0.2\mu m$ it is possible to determine crystallite shape, eg. needle-like crystals with a needle axis coinciding with c are expected to show broad (hk0) reflections and sharp (001) and (0kC) reflections.

For spectrometer measurements at back-reflection angles for the case of a narrow source profile β may be defined by:-

$$\beta = B - b$$

where, B = the measured diffraction line breadth,

b = the breadth of a line produced under similar geometrical conditions by a material with crystallite dimensions in excess of those in the broadening range ($\gtrsim 0.3\mu m$).

For the purpose of this work $\beta_{\frac{1}{2}}$, the Scherrer half-maximum peak width was determined by reference to $b_{\frac{1}{2}}$ which was obtained from a Si standard (111) line $\theta = 14.21^{\circ}$, and $B_{\frac{1}{2}}$ obtained from the Si_3N_4 - Al_2O_3 solid solution lines (200) $\theta \approx 13.52^{\circ}$, (101) $\theta \approx 16.82^{\circ}$ and (210) $\theta \approx 18.02^{\circ}$. The radiation was filtered to remove K_β content and the $K\alpha_1$ and $K\alpha_2$ lines were unresolvable in each case, thus no correction was necessary to account for breadth effects so derived.

The Scherrer equation may therefore be re-written:-

$$D_{hkl} = \frac{0.9\lambda}{(B_{\frac{1}{2}} - b_{\frac{1}{2}}) \cos\theta_{hkl}}$$

Scherrer half maximum peak widths were determined from the XRD patterns of several Syalon Ceramic alloys by measurement using a graticule and eyepiece.

4.1.3 Optical Microscopy

Selected specimens were prepared by grinding flat with progressively finer grades of SiC granule coated paper and polishing to a 1μm finish with diamond paste on a Metaserv lapping machine. After cleaning in an ultrasonic bath of acetone, they were mounted on glass slides, with plasticene, using a mounting clamp to ensure that the polished surface to be investigated was aligned parallel to the microscope table. A Zeiss Ultraphot II Camera Microscope was used in the 'Luminar' (simple microscope) mode; with both Bright Field and Dark Field illumination provided by a high pressure, 200 Watt, Hg lamp (HBO 200), to obtain photomicrographs using the standard photohead - see Figure 4.1. Bright field reflection microscopy, dominated by effects arising at polishing scratches and pits, was found to be of little value, many features plainly visible with the naked eye being obscured. Dark field reflection microscopy, conducted using a mirror to reflect the beam from the standard light source at grazing incidence to the specimen surface, enabled production of photomicrographs in which effects arising at true microstructural features are visible.

Thin ($\lesssim$ 80μm thick) specimens were prepared, polished on both faces to a 1μm finish, and examined in the bright field transmission mode.

In order to calculate magnification factors a standard graticule calibrated in decrements of 0.1mm was imaged through the microscope system and photographed. When printing photomicrographs, measurements from a print of the graticule were used to determine magnification factors.

4.1.4 Imaging and x-ray microanalysis in the SEM

Various accounts of Scanning Electron Microscopy (SEM) and Energy Dispersive X-ray Microanalysis (EDAX), in terms of theory

FIGURE 4.1 - Schematic of illumination modes of the optical microscope

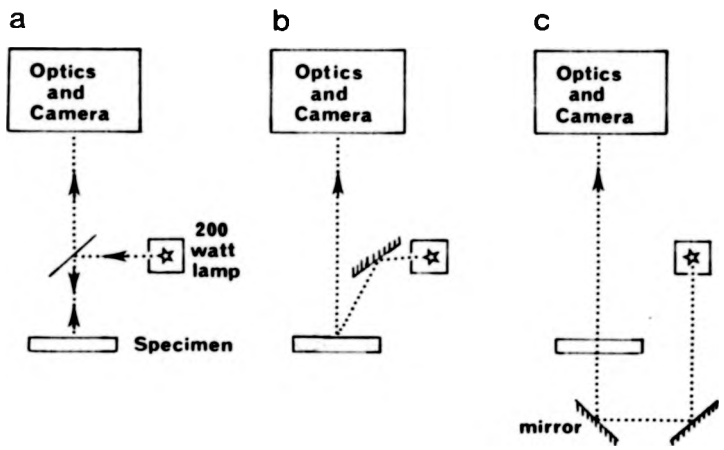

Bright field Reflection Microscopy.	Dark field Reflection Microscopy.	Bright field Transmission Microscopy.

and operating procedure are available in the literature[85],[86],[87] and such details will not be discussed here. The flat polished specimens, prepared to a 1μm finish and examined under the optical microscope, were mounted on aluminium studs using colloidal graphite 'Dag', and evenly coated under a vacuum of 10^{-5} Torr with a thin (~2Å) layer of carbon, to prevent the occurrence of charging effects under the electron beam.

A Cambridge S250 SEM equipped with a standard secondary electron detector and a solid state backscattered electron detector (K.E. Developments Ltd, Cambridge) was used to image the microstructure of selected ceramics. X-ray microanalysis was performed using and EDAX 9100 system and version 2.1 software capable of correction for atomic number absorption and fluorescence effects (ZAF correction). All microanalysis was performed under standard microscope conditions of:-

10kV accelerating voltage, specimen tilt angle of 45° to the electron beam, x-ray take-off angle of 39°, specimen working distance of 15mm and full scale range of 5000 counts.

Compositional analysis was expressed, on the microcomputer VDU, in terms of atomic percentage of each element detected and either saved on disk file or obtained in the form of a thermal printout. General imaging conditions used to obtain photomicrographs displaying high resolution and strong atomic number contrast were:-

10kV accelerating voltage, zero specimen tilt and 10mm working distance.

4.1.5 Imaging and x-ray microanalysis in the TEM

All aspects of theory and use of the Transmission Electron Microscope (TEM) are available in the literature[85],[88] and the reader is directed to these sources for reference. Samples were cut into slices of even thickness, ~300μm, using an annular diamond saw, and polished to a final thickness of 80-50μm with a 6μm finish on both faces using SiC granule coated grinding wheels and laps loaded with diamond paste. After cleaning in an ultrasonic bath of acetone, the thin slices were mounted on brass rings (~3mm diameter), using epoxy resin adhesive, and trimmed to fit the TEM specimen holder. Each specimen was ion milled on both faces in an 'Ion Tech' argon ion beam mill, at an angle of 45°, until punctured by the beam. After puncture

large areas of thin section were obtained for imaging in the TEM by reducing the incident argon ion beam angle to ~25° and reducing the accelerating voltage from ~5kV to ~3kV. To account for any effects of inhomogeneity a minimum of four samples from different parts of the sintered billets were prepared and explored in a Jeol 100C TEM. An EDAX 707B microanalysis system was employed to perform thin section analysis to define the composition of various microstructural features in the specimens. For each analysis standard conditions of:-

> 100kV accelerating voltage, specimen tilt angles of x = 45° and y = 27°, yielding an x-ray take-off angle of 45°,

were adopted with the analysed area adjusted to the eucentric position. Calibration of all spectra was performed by comparison with standard data - see Appendix 1.

4.1.6 Electron energy loss spectroscopy

Low fluorescence yield and collection efficiency at low Z makes x-ray microanalysis an insensitive technique for detection of oxygen or nitrogen. Although Wavelength Dispersive and Windowless Energy Dispersive x-ray detectors have been used in SEM based systems, they are not easily applicable to the transmission electron mode, and lack spatial resolution.

The relatively new technique of Electron Energy Loss Spectroscopy (EELS) allows light element analysis from areas as low as 50Å in diameter[89] in TEM based systems. The spectrometer records energy losses from the transmitted electron beam thus providing information about excitation processes occurring in the specimen. Full treatment of scattering kinematics are available elsewhere[90] and are not a prerequisite for consideration of the data to be presented. Basic explanation of the features of interest in an energy loss spectrum will be given, and the necessary experimental technique and treatment of results will be briefly discussed.

(a) Energy loss mechanisms

During an inelastic collision a fast electron transfers energy and momentum to the solid through which it is transmitted. Thus, measurement of the intensity of the inelastically scattered electrons as a function of energy loss and momentum transfer enables study of the

FIGURE 4.2 - Typical EELS spectrum

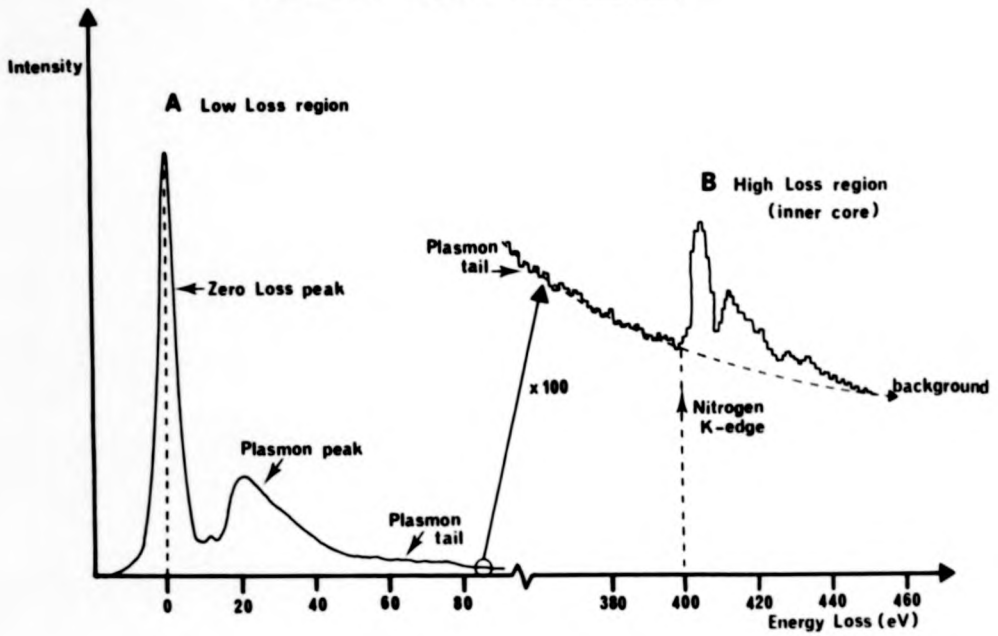

way in which the specimen absorbs that energy and momentum, leaving it in an excited state. The inelastic scattering creates a dynamic fluctuation in the electric charge density of the specimen, which may take several forms depending upon the class of specimen; through the free electron plasma of a conductor, or including the super-band gap valence electrons of a semiconductor or insulator. An electron density wave is formed, propogating through the medium, and this is the dominant feature of the low loss spectrum known as the Bulk Plasmon - see Figure 4.2A.

At higher energy losses the primary feature of the spectrum arises from inner core shell loss, where an electron is excited from an inner core, leaving a hole. Local chemical analysis may be derived by consideration of the total scattering cross-section and energy of the loss peak so derived - see Figure 4.2B. Fine structure on the peak immediately above the core edge provides information relating to the valence band to which the excited electron has been promoted. Small ($\sim$5eV) shifts of the core edge occur reflecting the local valence band chemistry, and $\sim$20eV above the edge Extended Energy Loss Fine Structure (EXELFS) may be related to scattering of the ejected electron by neighbouring atoms.

Spectra may be obtained in either the imaging or diffraction mode, the plasmon loss peak intensity being relatively higher and more asymmetric in the former. Use of thin specimens ($\lesssim$500Å at 100kV) is extremely important if multiple scattering events which reduce the signal/background ratio at the edges, are to be avoided.

(b) Experimental technique and treatment of results

Three Syalon ceramic TEM specimens were prepared as previously described (Section 4.1.5), except they were not carbon coated, and two samples of homogeneous bulk YSiAlON glasses were prepared as reference standards. Carbon coating was avoided to prevent interference from the film in the energy loss spectrum. Ceramics S-0, S-10.75A and S-10.75B were selected, and compositional details were presented earlier - see Table 2.2. The glasses were produced from 'Laboratory grade' SiO_2, Al_2O_3, AlN and Y_2O_3, pressed into green compacts, and melted in BN lined graphite crucibles under an ambient pressure nitrogen atmosphere in an R.F. tube furnace - see Table 4.3 for details. Glasses were air quenched by removing them from the furnace to cool. Each specimen was examined in a Philips TEM and analysed in the convergent beam diffraction mode using a Gatan energy loss spectrometer (courtesy of

University of Birmingham, Department of Metallurgy and Materials). Thus, for the case of the β' phase characteristic diffraction patterns were observed, and for the case of the intergranular matrix diffuse diffraction halos, characteristic of the glassy state, were observed prior to analysis.

In each case thin areas were selected for analysis to avoid multiple inelastic scattering. Inspection of the spectra so obtained (and presented in Section 4.2.6) enables determination of the N/O ratio for each area probed via the expression:-

$$N/O = \frac{A_N(\alpha, \Delta E)}{A_O(\alpha, \Delta E)} \cdot \frac{\sigma_O(\alpha, \Delta E)}{\sigma_N(\alpha, \Delta E)}$$

where, for a given acceptance angle, α, and energy after the edge, ΔE;-

$A_N(\alpha, \Delta E)$ and $A_O(\alpha, \Delta E)$ are the areas under the nitrogen K edge and oxygen K edge, after background subtraction, respectively.

$\sigma_N(\alpha, \Delta E)$ and $\sigma_O(\alpha, \Delta E)$ are the partial ionisation cross-sections for nitrogen and oxygen applicable under the experimental conditions.

For experimental conditions of 8.33 mrad acceptance angle and 40 eV energy window the ratio σ_O/σ_N = 585/1279 = 0.457 was obtained.

The N/O ratio for each glass, determined from the relevant EELS spectrum, was then combined with the data of Si-Al-Y analysis obtained from the TEM/EDAX system, and thus the complete elemental analysis, Si-Al-Y-O-N, was derived (assuming oxide stoichiometry).

Glass	1	2
^{w}/o SiO_2	45.774	39.637
Al_2O_3	14.578	/
Y_2O_3	34.580	45.209
AlN	5.061	15.154
^{a}/o Si	18.984	17.736
Al	10.202	9.940
Y	7.632	10.765
O	60.010	51.620
N	3.077	9.940
Melt Temp.	1650°C	1700°C
Melt time	45 mins	45 mins

TABLE 4.3

Compositional and fabrication details of 'standard' glasses prepared for EELS

4.2 Results of microstructural characterisation

In this section the results obtained using the techniques described in section 4.1 are presented and briefly discussed.

A full discussion relating all results is presented as section 4.3 in which the relationships between composition, fabrication method and final microstructure are recognised.

4.2.1 Density data

The density determined for various ceramic alloys was found to be $\sim$3.23-3.24 as presented in Table 4.4.

TABLE 4.4 - Density determined for selected Syalon Ceramic alloys

Alloy	S-0	N-2	N-4	N-6	N-8	S-11.5
Density $g.cm^{-3}$	3.240	3.229	3.226	3.241	3.236	3.244

If the porous volume is assumed negligible and ρ_g = 3.19 then, for a Syalon Ceramic of composite density ρ = 3.24 $g.cm^{-3}$, the volume fraction of glass present, of a given density, may be calculated, see Table 4.5. Bulk densities of YSiAlON glasses have been determined in the range 3.4-4.0 $g.cm^{-3}$ depending upon composition[91].

TABLE 4.5 - Volume fraction of glass calculated for Syalon Ceramic of composite density 3.24 $g.cm^{-3}$.

Glass density $g.cm^{-3}$	3.9	3.8	3.7	3.6	3.5
Glass volume %	7	8	10	12	16

The major factors influencing the precision of hydrostatic weighing have been outlined elsewhere[42], and for small specimens the sensitivity of the weighing balance has been identified[93] as the limiting factor in precision. The uncertainty in density, $\Delta\rho$, has been related to the uncertainty in weight, ΔW, by the relationship:-

$$\frac{2W_w^2}{(W_a - W_w)^2}\left(\frac{\Delta W}{W}\right)^2 = \frac{\Delta\rho^2}{\rho^2} \qquad [94]$$

and, since $W_w/W_a \approx 0.693$ for Syalon Ceramic, then $\frac{2W_w^2}{(W_a - W_w)^2} \approx 10.2$

and the relationship reduces to:-

$$\frac{\Delta\rho}{\rho} = 3.19\frac{\Delta W}{W}$$

Thus, for a specimen of mass 1g and uncertainty in weight of 1mg, the uncertainty in density is $\Delta\rho \approx 0.3\% \approx 0.01 g.cm^{-3}$ for Syalon ceramic. It can therefore be concluded that for all ceramics weighed, $\rho_{Syalon} \approx 3.24 \pm 0.01 g.cm^{-3}$ and the volume fraction of glass present lies in the range 7-16%.

4.2.2 Analysis of X-ray diffraction spectra

Measurements were taken from the diffraction spectra of various N-series and S-series Syalon Ceramic alloys, in the as-sintered state. The major crystalline phase identified from spectra was β'_{ss}, no glassy halo was evident but there were some extra reflections present, of low intensity, in the spectra of some alloys, and a small amount of α' in alloy S-11.5.

A list of interplanar (d_{hkl}) spacings determined from the β'_{ss} of alloy N-2 is presented in Table 4.6 alongside data (from the ASTM Index) for β-Si_3N_4 to facilitate comparison. The data presented was adjusted for zero shift by calculation of a zero shift correction, $\Delta\theta$, via the expression:-

$$\frac{\text{Sin}\ (\theta_{(500)} + \Delta\theta)}{\text{Sin}\ (\theta_{(200)} + \Delta\theta)} = 2.5000$$

and all calculations were performed with 10 significant figures to reduce rounding up errors.

For various N-series and S-series alloys the β'_{ss} cell parameters, a and c, were determined from the position of the (500) and (002) reflections, and are presented in Table 4.7. The intensity of the diffraction peaks, normalised to that of the (101) reflection, were obtained from the spectra of various alloys. Diffraction from all N-series alloys was identified with the I/I(101) data set presented in Table 4.6. Similarly a characteristic set of intensity data identified diffraction spectra obtained from S-series alloys, also presented in Table 4.6, with data for β-Si_3N_4 (ASTM Index) for comparison. The differences, for a given (hkl) reflection, between the diffraction intensity sets obtained from N-series and S-series alloys were repeatable, regardless of composition, for the diffraction and specimen conditions used. It should be noted that (h00) reflection intensities are

TABLE 4.6

Comparison of XRD data obtained with Card 9-259*

β-Si_3N_4 d(Å) *	β'_{ss}(N-2) d(Å)	hkl *	β-Si_3N_4 I/I(101)*	β'(Norton) I/I(101)	β'(Starck) I/I(101)
6.63	6.593	100	18	35	56
3.82	3.802	110	20	38	67
3.31	3.296	200	85	103	103
2.668	2.662	101	100	100	100
2.492	2.490	210	100	95	98
2.312	2.313	111	10	6	31
2.180	2.184	201	35	28	55
1.904	1.902	220	6	6	22
1.892	1.895	211	6	4	19
1.827	1.828	310	20	9	31
1.753	1.754	301	70	35	63
1.593	1.594	221	20	9	28
1.548	1.550	311	10	4	16
1.512	1.512	320	35	11	32
1.455	1.458	002	35	11	35
1.437	1.442	410	20	6	24
1.358	1.361	112	4	2	3
1.341	1.343	321	14	35	64
1.330	1.334	202	18	5	21
1.317	1.318	500	18	3	12
1.283	1.291	411	85	14	38
1.268	1.269	330	20	5	18
1.255	1.258	212	85	11	34

* ASTM Powder Diffraction Data File.

For alloy N-2 β'_{ss} Hexagonal unit cell, a = 7.610 from (500)
c = 2.917 from (002).

Observed peak intensities, normalised to that of (101), obtained from β'_{ss} of Norton source and Starck source materials should be compared to data from Card 9-259 of the ASTM Index.

affected in the same way for both Starck and Norton source alloys, ie. (100) and (200) are increased, (500) are decreased, but since the changes are not consistent the cause is unlikely to be morphological.

TABLE 4.7

β'_{ss} Hexagonal cell parameters and crystal sizes determined from XRD.

Alloy	a(Å)	c(Å)	Δ·•	D_{hkl} (μm) (200)	(101)	(210)
S-0	7.609	2.911	-0.034	>>0.3	>>0.3	>>0.3
N-2	7.610	2.917	-0.118	0.23	0.17	0.21
N-4	7.612	2.917	-0.141	0.16	0.14	0.17
N-5	7.613	2.918	-0.158	0.27	0.24	0.21
N-6	7.613	2.918	+0.058	0.33	0.28	0.33
N-8	7.618	2.918	-0.155	0.27	0.21	0.24
β-Si_3N_4*	7.606	2.909	/	/	/	/

* Card 9-259 ASTM Powder Diffraction Data File.

Other variations between Starck and Norton source alloys occur over the whole diffraction pattern ruling out an instrumental effect as the cause of the variations. For alloy S-0 the β'_{ss} crystal size, D_{hkl}, was determined as >>0.3μm from measurements of (200), (101) and (210) Scherrer half-line widths and reference to a silicon standard diffraction pattern. Thus the S-0 β'_{ss} diffraction spectrum was used as a standard to determine β'_{ss} crystal sizes of other Syalon ceramic alloys. The data, presented in Table 4.4, may be taken as evidence that a significant proportion of the β'_{ss} crystals in all alloys, other than S-0, are <0.3μm in dimension, and values should not be treated as absolute but relative. An error in D_{hkl} of ~ 25% is applicable by assessment of $B_{\frac{1}{2}} \pm 0.005^{o}$ and $b_{\frac{1}{2}} \pm 0.005^{o}$ 2θ.

Nb.peak broadening is unlikely to be caused by a range in the β'_{ss} since homogenisation of cored β' grains is expected to occur quickly[45].

4.2.3 Analysis of Optical Micrographs

A visual inspection of polished ceramic specimens, with the naked eye in reflected light, revealed a trend in colouration with 21R content from light grey alloy S-0 to dark grey alloy S-11.5. The presence of dark 'spots' was also noted in the case of alloy S-11.5.

Dark field optical microscopy revealed the presence of faint light patches on the polished surface of alloy S-0. Similar patches, $\sim$ 0.1-0.5μm diameter, were more easily observed on all N-series ceramics due to the increased contrast present - see Figure 4.3A. The alloys S-11.5, S-10.75A and S-10.75B, of high 21R content all exhibited the presence of bright 'specks', possibly associated with the presence of porosity - see Figure 4.3B.

Specimens prepared as cross-sections containing part of the billet external surface displayed the presence of layers running parallel to the surface, as seen in Figure 4.3B. An outer layer completely free of specks and therefore appearing dark is seen to extend $\sim$0.6mm into the billet, where there is an interface with a light layer which is seen to contain many large specks. These two layers account for a surface band $\sim$ 1.4mm thick beyond which bulk material is found.

4.2.4 Analysis of SEM/EDAX Results

(a) Imaging

A specimen of each ceramic alloy was examined in the back-scattered electron mode and photomicrographs obtained at low, medium and high magnification factors to facilitate comparison of the various microstructures.

In each case the major phase present, β', took the form of well-faceted grains embedded in a matrix, very much lighter in contrast and therefore very much higher in mean atomic number. Some β' grains sectioned normal to the c-axis appeared approximately hexagonal, others sectioned parallel to the c-axis displayed a high aspect ratio of mean value $\sim$8:1.

Consider Figure 4.4A, the β' grain size of alloy S-0, defined by minimal prism diameter, P, and therefore unaffected by the angle of the prism axis to the section, can be seen to be distributed over an approximately monomodal size range about a mean of 0.57μm. Some of the smaller grains appeared to have a rounded outline possibly due to dissolution in the sintering liquid as part of the Ostwald

Figure 4.3

Comparison of optical micrographs from Sialon Ceramics with variation in 21R polytypoid addition

A. alloy S-0 as sintered cross-section

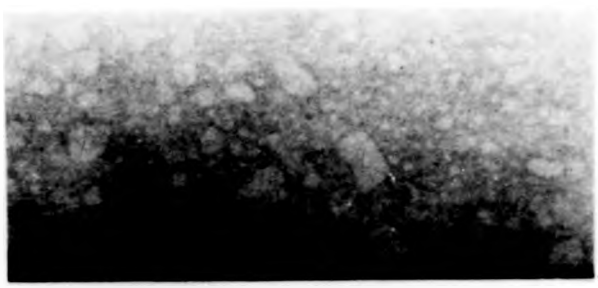

B. alloy S-10.75A as sintered cross-section

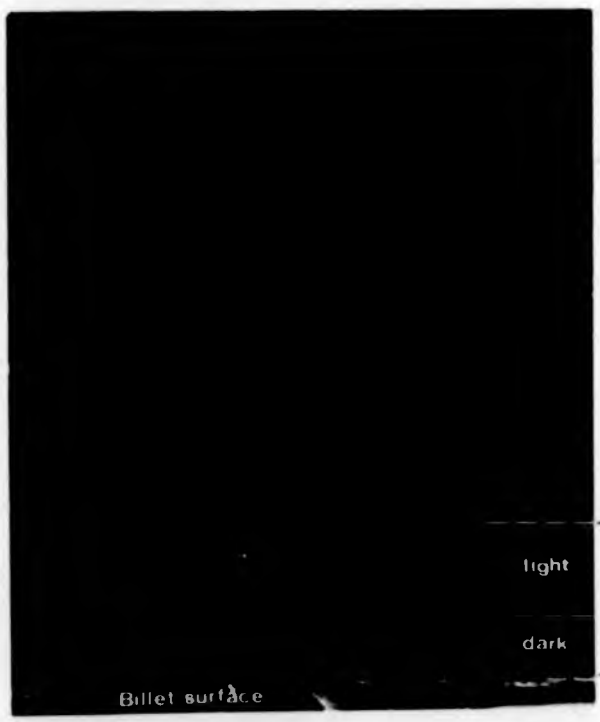

Figure 4.3

Comparison of optical micrographs from Sialon Ceramics with variation in 21R polytypoid addition

A. alloy S-0 as sintered cross-section

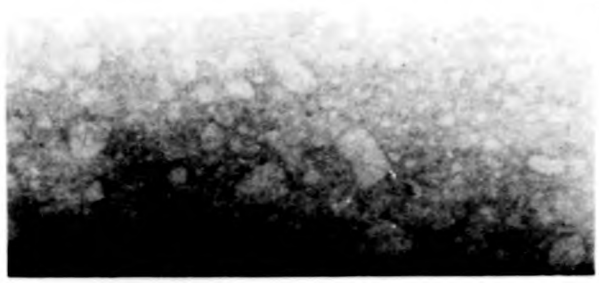

B. alloy S-10.75A as sintered cross-section

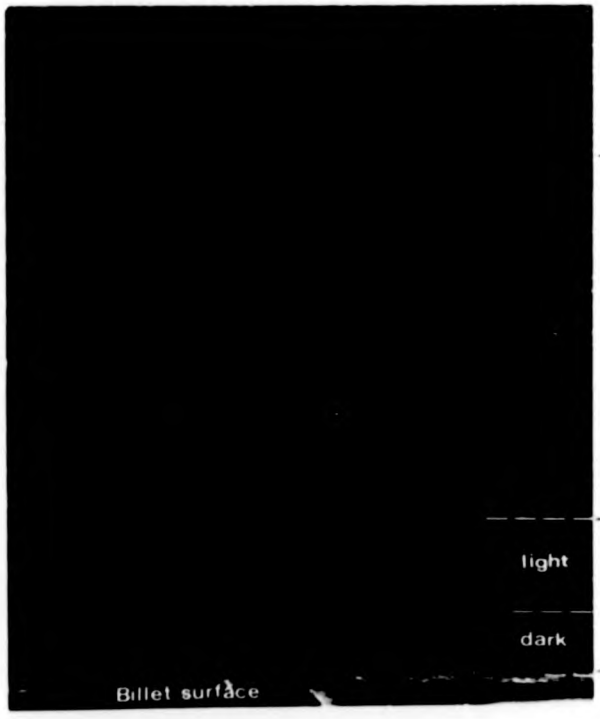

FIGURE 4.4 - β' grain size distributions in alloys S-0 and S-11.5

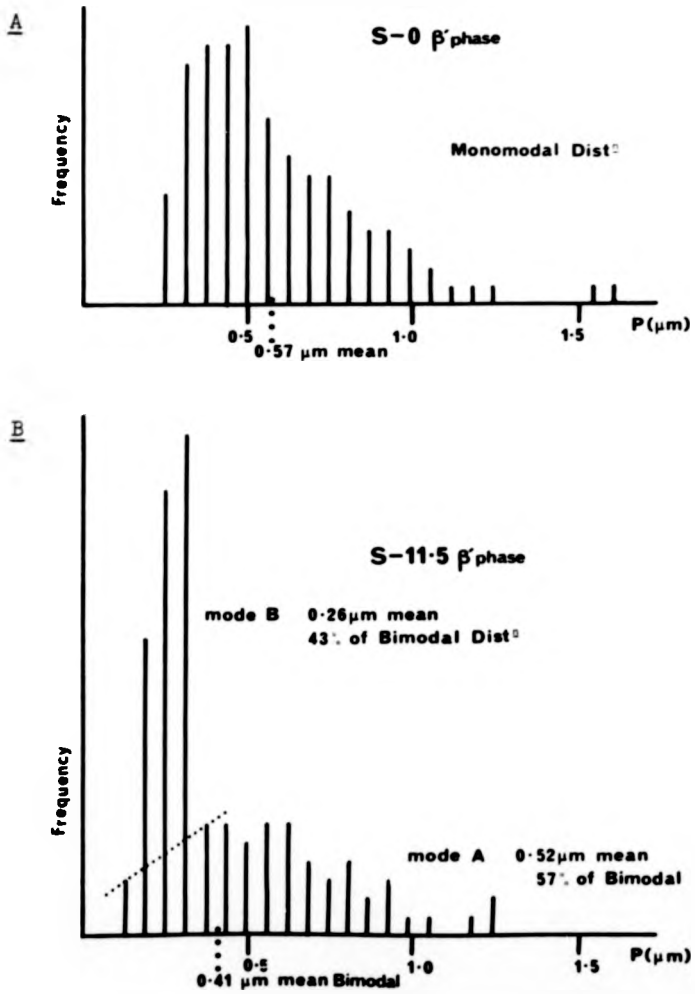

Histograms of frequency versus minimal prism diameter, P, determined using the back-scattered electron mode in the SEM and taking measurements from the micrographs.

ripening process. On a localised scale the ceramic may be described as fully dense with no porosity evident either in the β' or the intergranular matrix, however, in some places large pores are present.

In comparison the β' grains present in alloy S-11.5 - see Figure 4.4B, occur in an approximately bimodal size distribution, there being many small grains (0.26μm mean) situated at the boundaries of the larger (0.52μm mean) ones. This bimodal grain size distribution was found to be characteristic of all materials except S-0.

From selected alloys of varying 21R content back-scattered electron photomicrographs, of magnification factor 16.5k, were examined using an image processor (courtesy of Alcan Laboratories, Banbury) and an estimation of matrix phase area fraction, A%, was obtained - see Table 4.8 and Figure 4.5. It is readily seen that an increased oxygen content is associated with an enhanced glass volume, and by inference enhanced volume of sintering liquid. Alloy S-0 contains a significantly higher glass content than expected by extrapolation from data derived from other alloys due to its elevated yttrium content.

TABLE 4.8 - Intergranular glass volumes for various alloys (SEM/image processor)

Alloy	S-0	N-2	N-5	N-8	S-11.5
A°o	12.79	8.40	9.81	11.14	7.34

The relationship between glass O/N ratio and 21R addition, as calculated using Models 1A* and 2,** is presented in Figure 4.6.

Observation of the billet surface layers, described in the previous section, confirmed that the 'specks' relate to areas of enhanced porosity and it was found that the very outer layer, ~0.6mm thick, contained far less glass volume than the bulk of the material.

Backscattered electron images of ceramics S-10.75A and B are presented, for comparison, as Figure 4.7. The glass volume fraction of S-10.75A appears higher than that of S-10.75B and, since the total yttrium content of each ceramic is equal, this implies that the glass composition of S-10.75B must be richer in yttrium than the glass of S-10.75A. The mean β' grain size is seen to be greater in ceramic S-10.75A (sintered at 1750°C) than in S-10.75B (1700°C) and this effect is more easily appreciated with the human eye by consideration of photomicrographs obtained in the inverted backscattered mode, see Figure 4.8.

* see Section 2.2.1.e pg. 27

** see Section 4.2.5.b pg. 78, Model 2 is a calculation of β' and intergranular glass composition utilising data from TEM/EDAX.

FIGURE 4.5 - The relationship between O/N ratio and glass volume

Alloy	N-2	N-5	N-8	S-0	S-11·5
%Y as mixed	1·129	1·129	1·130	1·308	1·171

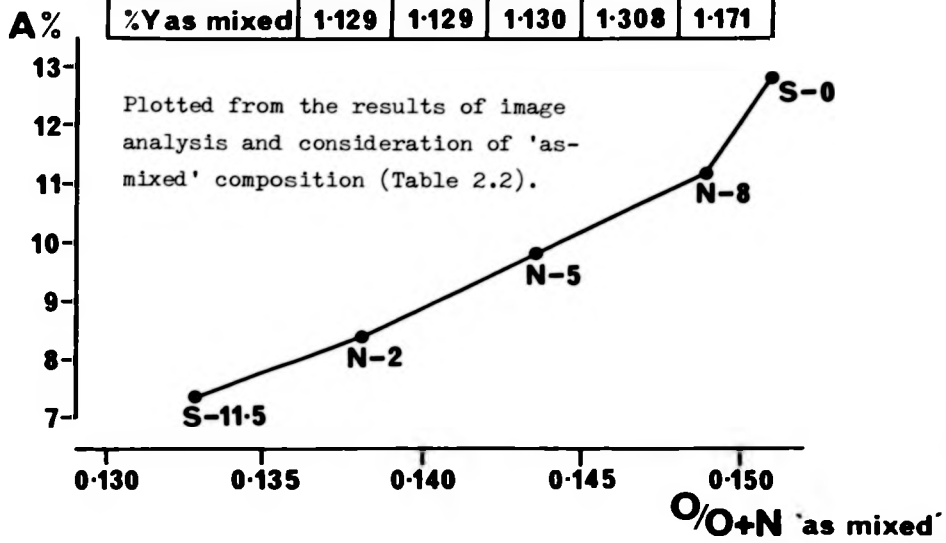

FIGURE 4.6 - The relationship between O/N ratio and 21R addition

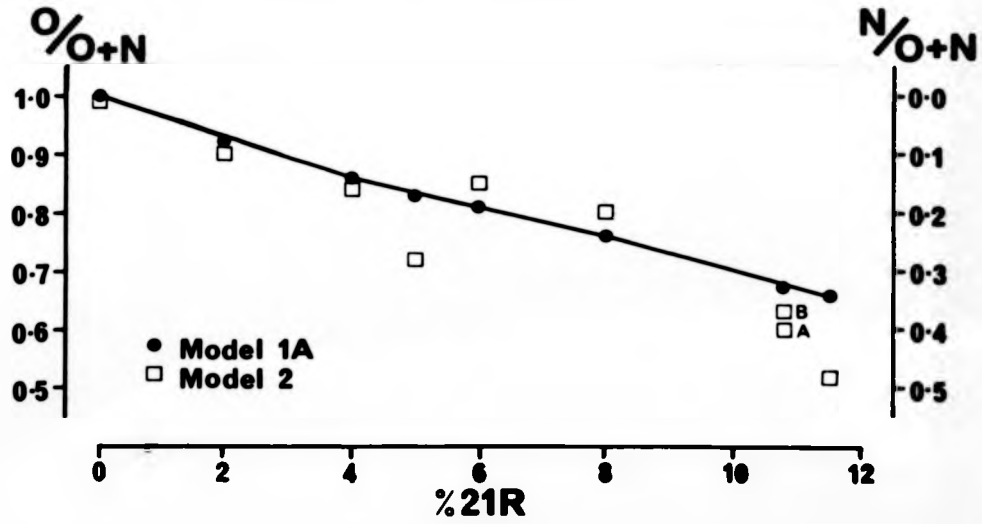

Model 1A is a calculation of the 'potential liquid forming component' composition - pg. 27.

Model 2 is a calculation of the intergranular glass Y-Si-Al-O-N composition using data of Y-Si-Al analysis (TEM/EDAX) and assuming a conservative system - pg. 78.

FIGURE 4.7 - Backscattered electron images

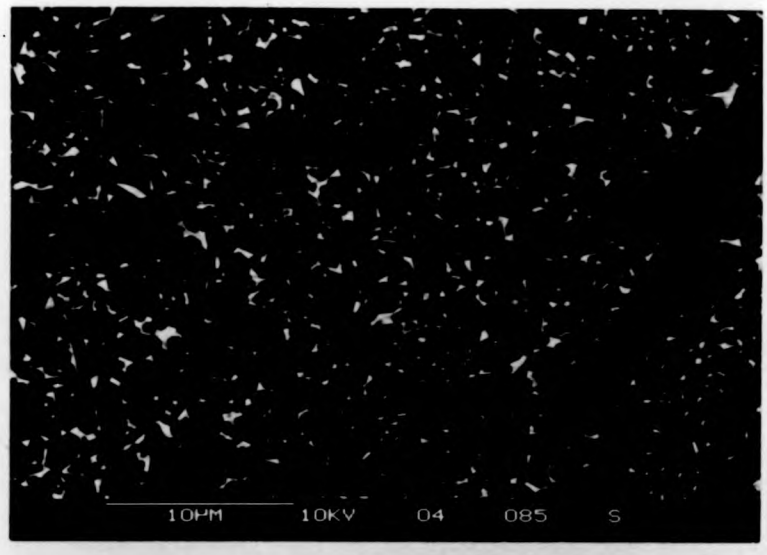

A S-10.75A

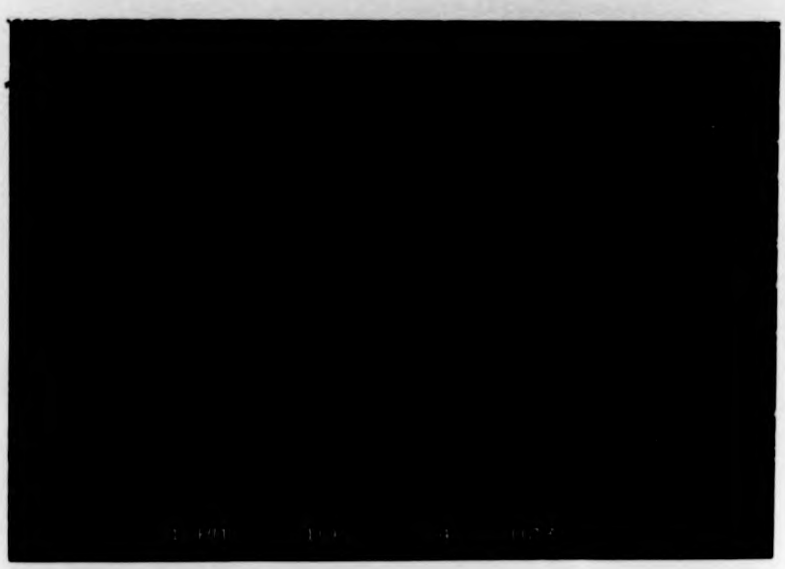

B S-10.75B

FIGURE 4.7 - Backscattered electron images

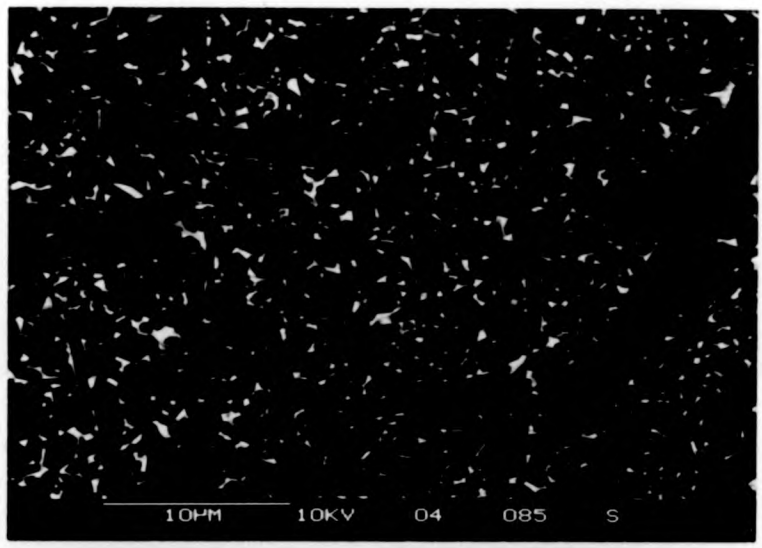

A S-10.75A

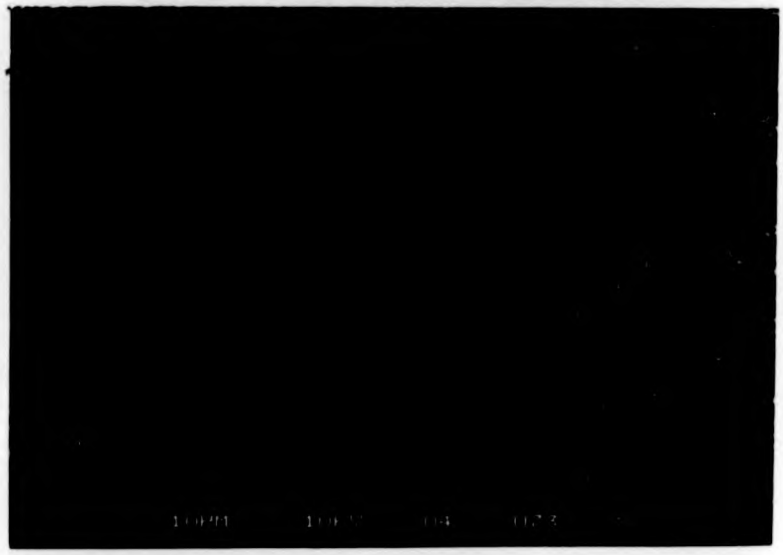

B S-10.75B

FIGURE 4.8 - Inverse mode backscattered electron images

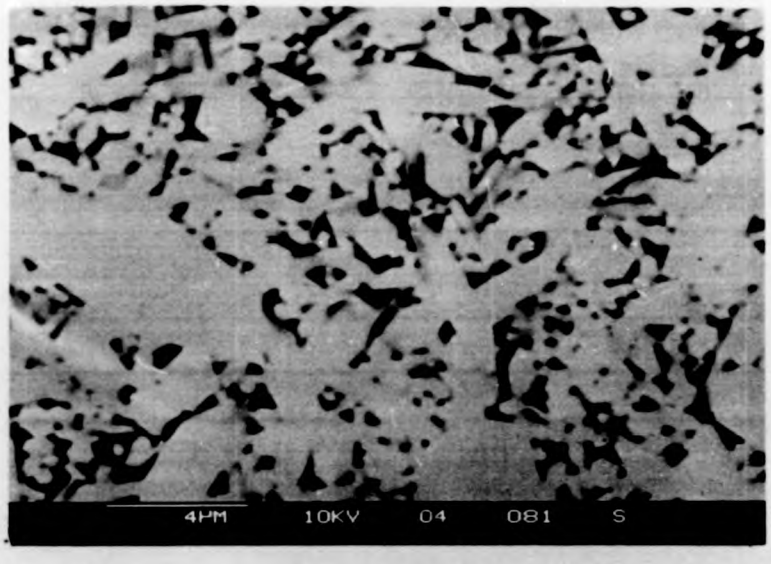

A S-10.75A

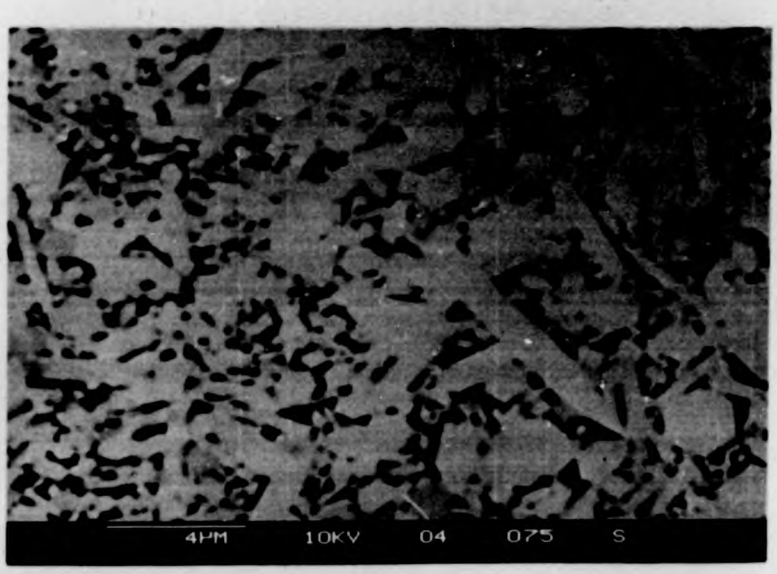

B S-10.75B

FIGURE 4.8 - Inverse mode backscattered electron images

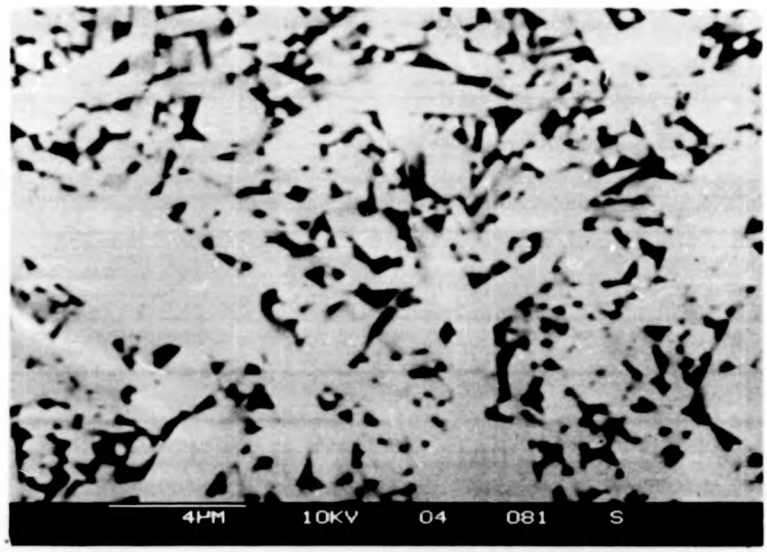

A S-10.75A

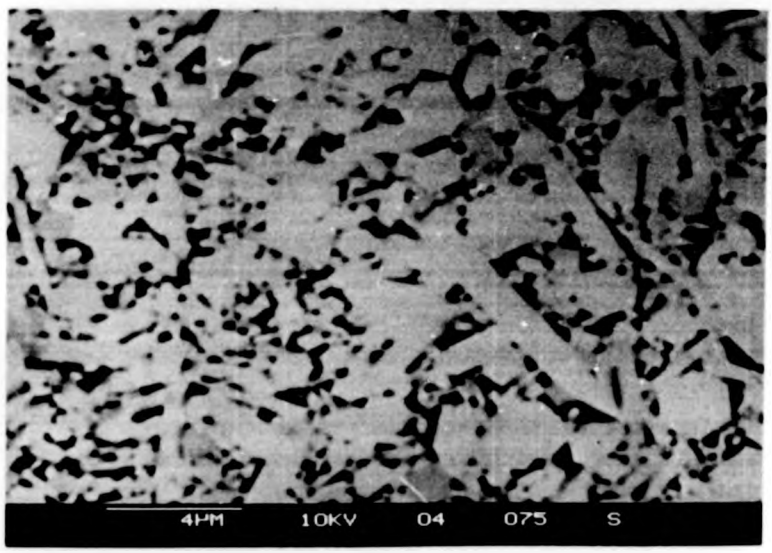

B S-10.75B

Occasional grains of lighter contrast than the general β' phase are apparent in Figures 4.7A and 4.7B (darker contrast in 4.8A and 4.8B). These grains are possibly α' phase in which the small yttrium solubility gives rise to a higher mean atomic number contrast than observed in β' phase. Such grains were observed in greater numbers in alloy S-11.5.

(b) X-ray microanalysis in the SEM

A normalising procedure was performed on all analyses as explained in Appendix 1.

Data was obtained from the β' phase of selected alloys, any analyses exhibiting a contribution from the YL lines, and therefore 'contaminated' due to fluorescence effects arising in the matrix phase, were discarded. The remaining analyses were recorded on magnetic disk in the 9100 microcomputer system and the value z of the β' composition $Si_{6-z}Al_zO_zN_{8-z}$ calculated. Further computation led to construction of a frequency/z histogram and identification of the mean z value, $\bar{z}$, and its associated standard error, e, which were displayed on the VDU and obtained in print-outs, see Figure 4.9.

It was only possible to obtain reliable data from β' grains with a minimal prism diameter $P \geqslant 0.5\mu m$, however, a linear increase in $\bar{z}$ with w/o 21R addition is clearly demonstrable for this data. No evidence of coring was found in any of the larger grains, and multiple analyses obtained from within each single grain were in almost exact agreement.

Some of the large matrix pools present in each ceramic were analysed and their composition ranges plotted on the equivalent ternary oxide diagram (assuming all cations balanced by the presence of O^{2-} ions). All data fields were found to be concentrated in the glass-forming region near the ternary eutectic line, as expected.

Many of the largest matrix pools present in each material exhibited very high atomic number contrast, even with respect to the glass phase. EDAX proved these pools to be rich in Fe and Si with minor amounts of Cr, V, Mn and other alloying elements common to steel. Other pools in N-series ceramics were found to be rich in Ti and Si.

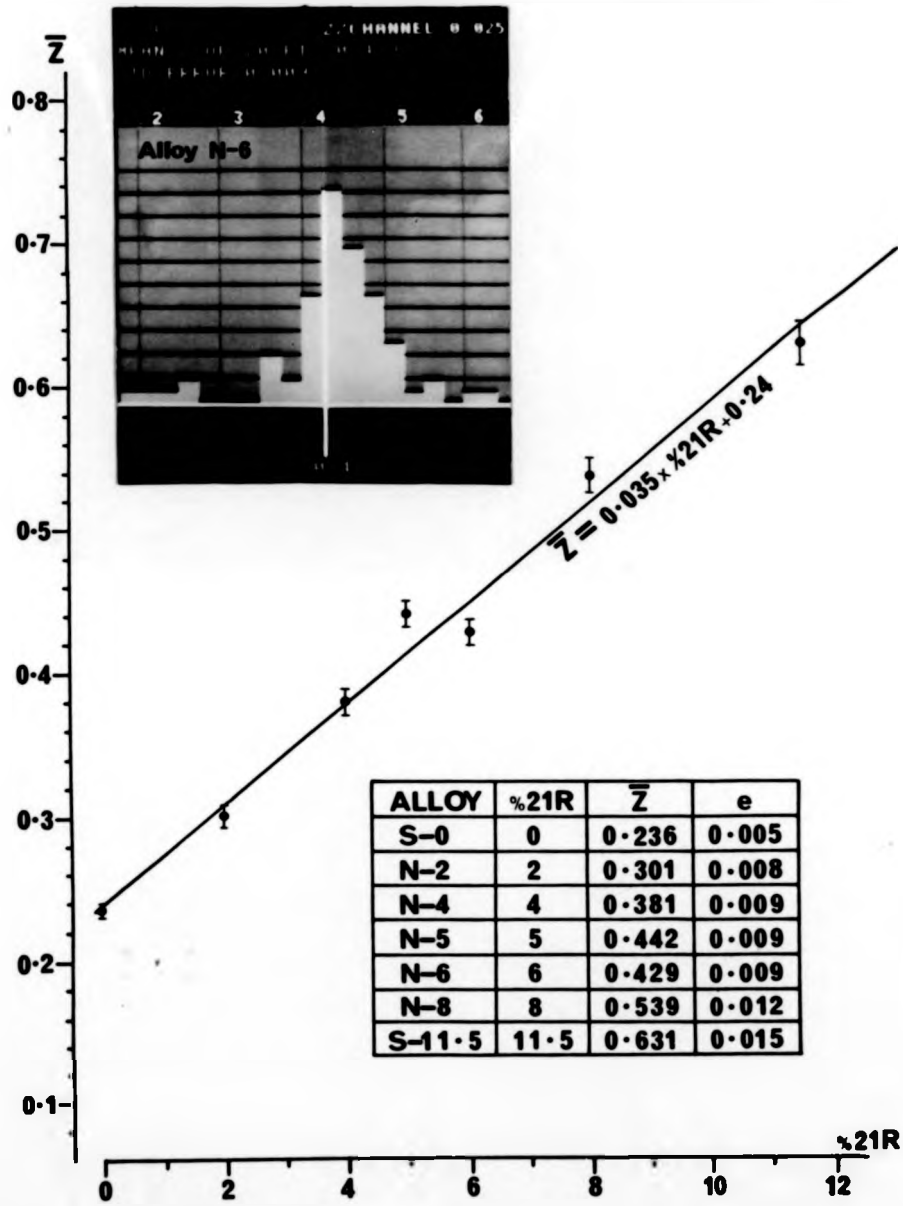

ALLOY	%21R	$\bar{Z}$	e
S-0	0	0·236	0·005
N-2	2	0·301	0·008
N-4	4	0·381	0·009
N-5	5	0·442	0·009
N-6	6	0·429	0·009
N-8	8	0·539	0·012
S-11·5	11·5	0·631	0·015

FIGURE 4.9 - The variation of z with wt% 21R addition

The frequency/z histogram for alloy N-6 is shown. The standard error, e, is related to the standard deviation of the data, σ, and the number of β' grains sampled, n, by the relation:-

$$e = \sigma / \sqrt{n}$$

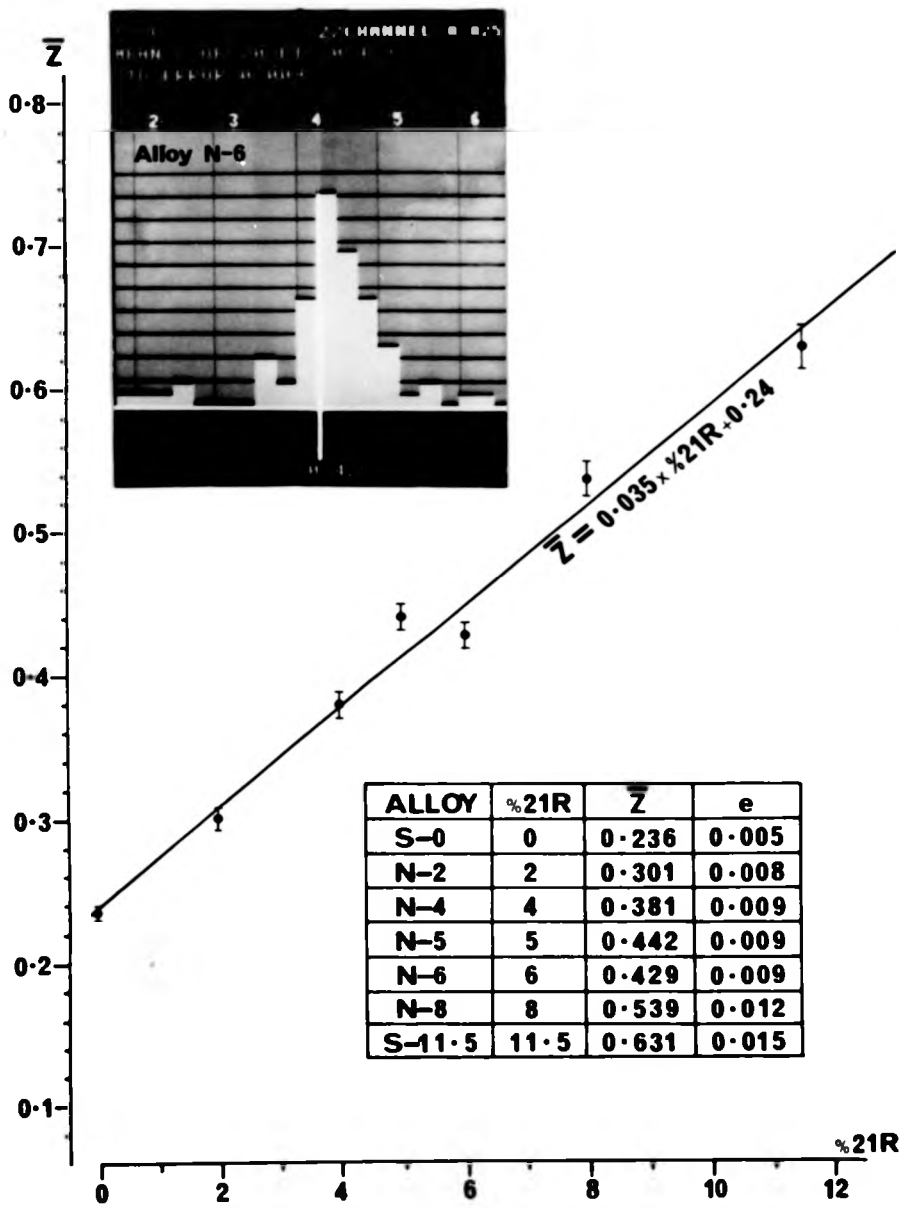

ALLOY	%21R	$\bar{Z}$	e
S–0	0	0·236	0·005
N–2	2	0·301	0·008
N–4	4	0·381	0·009
N–5	5	0·442	0·009
N–6	6	0·429	0·009
N–8	8	0·539	0·012
S–11·5	11·5	0·631	0·015

FIGURE 4.9 - The variation of z with $^{w}/_{o}$ 21R addition

The frequency/z histogram for alloy N-6 is shown. The standard error, e, is related to the standard deviation of the data, σ, and the number of β' grains sampled, n, by the relation:-

$$e = \sigma / \sqrt{n}$$

4.2.5 Analysis of TEM/EDAX results

(a) Imaging and diffraction

Thin sections of selected alloys were imaged in the bright field mode and β' grains of varying size were readily identified in the microstructure, their generally prismatic form being easily related to that observed in the SEM, see Figure 4.10.

The intergranular phase appeared more opaque to electrons than the β' grains (due to increased absorbtion by the relatively heavy Y^{3+} ions present), and its glassy nature was confirmed:-

(1) Unlike the crystalline β' grains, the matrix phase did not exhibit diffraction contrast effects during tilting sequences.

(2) In the Selected Area Diffraction (SAD) mode only 'halos' characteristic of the glassy state were obtained from this phase.

(3) During observation, the 100kV electron beam caused radiation damage, in the form of cavitation on a micro-scale, in this phase.

In the diffuse dark field mode, in which an objective aperture is positioned over part of the diffraction halo, the glass was found to totally envelop β' grains as previously observed[96].

SAD from the β' phase proved its hexagonal symmetry and calculation of unit cell parameters indicated values of $a \approx 7.61$ Å
$c \approx 2.91$ Å.

The presence of small round dark pools was noted in some of the larger β' grains, especially in the more 21R rich alloys, S-10.75 and S-11.5. Another feature, possibly associated with the presence of these pools, was a relatively high dislocation density in the β' phase.

(b) X-ray microanalysis in the TEM

X-ray spectra were calibrated as described in Appendix 1, only thin areas near the specimen edge were analysed. The contamination spot, deposited on each surface of the analysed thin section, was monitored to ensure that the electron beam only interacted with the areas from which analysis was required.

Both large and small β' grains were analysed and although compositional variability was demonstrated within each specimen, this was not a grain size related effect and data always lay

FIGURE 4.10

TEM thin section of alloy N-6

β' and glassy (g) regions are indicated.

FIGURE 4.10

TEM thin section of alloy N-6

β' and glassy (g) regions are indicated.

FIGURE 4.11 - EDAX in the TEM for alloy S-0

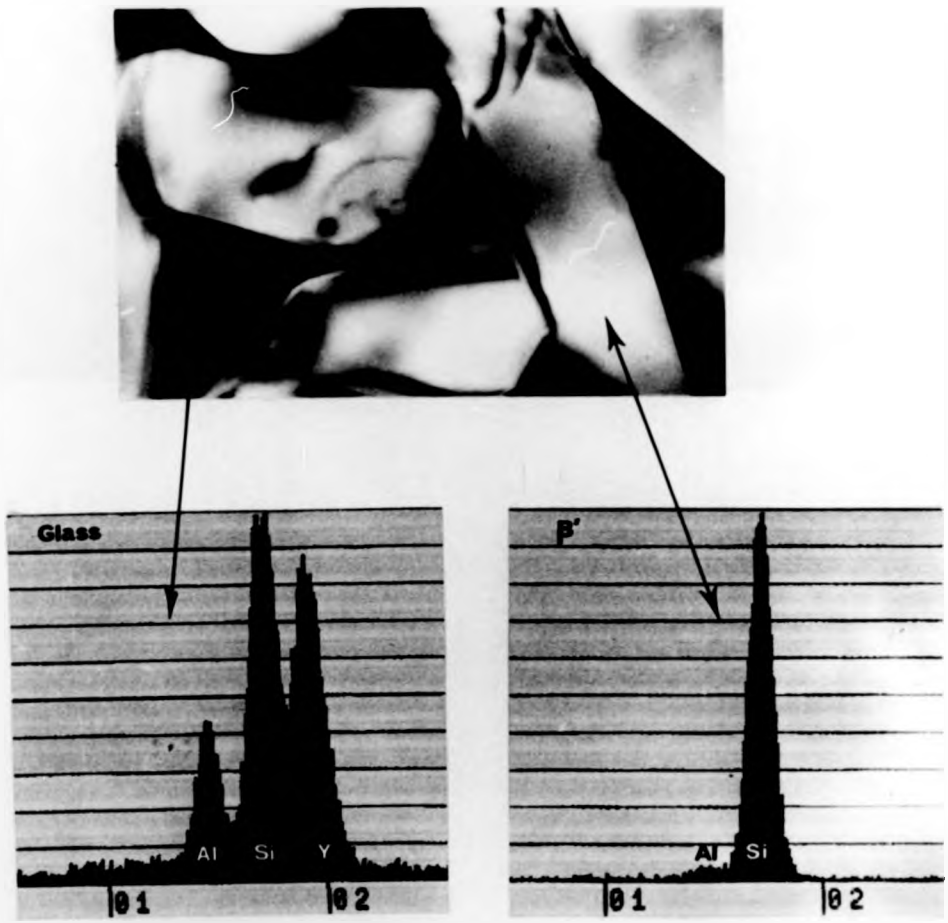

CATIONIC RATIOS:-

Al	:	Si	:	Y
23.01	:	47.38	:	29.60

Al	:	Si
3.44	:	96.56

$z \approx 0.21$

FIGURE 5.11 - EDAX in the TEM for alloy S-0

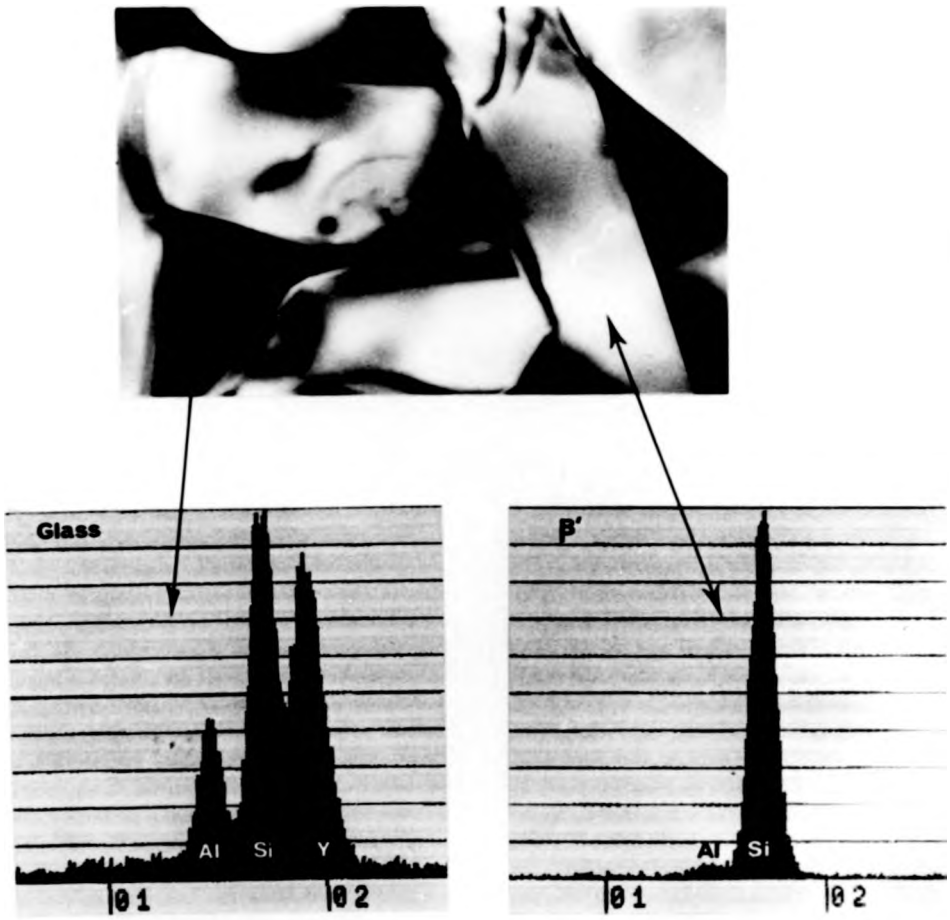

CATIONIC RATIOS:-

Al	:	Si	:	Y
23.01	:	47.38	:	29.60

Al	:	Si
3.44	:	96.56

$z \approx 0.21$

within the range of z determined by SEM/EDAX technique.

Large glassy pockets were analysed and their compositions determined, see Figure 4.11. Again some variability was demonstrated within each specimen, but mean analyses were in agreement with data obtained in the SEM and are presented as Figure 4.12. Using this data for glass cation content, assuming no losses during sintering and that all Y^{3+} is contained in the intergranular glass phase, a calculation of a/o O and a/o N in the glass and z in $Si_{6-z}Al_zO_zN_{8-z}$ was performed. The data obtained is presented as Table 4.9 and values of z obtained from this calculation (Model 2) are compared with data from Model 1 and with results from SEM/EDAX in Figure 4.13. It may be seen that the general trend observed using SEM/EDAX is verified by Models 1 and 2.

The change in oxygen and nitrogen contents in the glasses as calculated by Model 2 may be compared with those expected in the sintering liquids (ignoring the presence of Si_3N_4 and calculated as Model 1A) by comparison of Tables 4.9 and 2.3. The calculated glass nitrogen content varies in the range 0a/o to 28a/o, of which the alloys N-5, S-10.75 and S-11.5 exceed the accepted range of nitrogen content for bulk glasses 0 - 15a/o. Thus it would seem that the matrix of these ceramics should lie outside the glass-forming compositional volume. However, consideration of glass structural parameters derived from Model 2 data shows that the range of R' (2.28 - 2.75) and Y' (2.49 - 3.45) lies within that found to enable formation of stable glasses (R', 2 - 2.96) in which three-dimensional structures form (Y', 2.1 - 3.7).

For glasses of similar cationic composition, an increase in nitrogen content may be seen to cause an increase in Y' and hence properties such as viscosity, see Figure 4.14. Two lines may be drawn through the data points of this plot. One line 'a' joins data from alloys S-0, N-2, N-4 and S-11.5, which are readily seen to be of similar cationic composition identified in projection onto the ternary oxide diagram. Another line,'b', relates data from alloys N-6, N-8 and S-10.75A lying in a less Si^{4+}, more Y^{3+} rich part of the phase diagram, and therefore expected to contain a more open, less bonded, network structure. Alloy N-5, being the most silica rich of all alloys, shows an expectedly high value of Y', and alloy S-10.75B, poorer in network formers and richer in modifying Y^{3+} ions exhibits a lower Y' parameter.

FIGURE 4.12 - Syalon Ceramic intergranular glass compositions (TEM/EDAX)

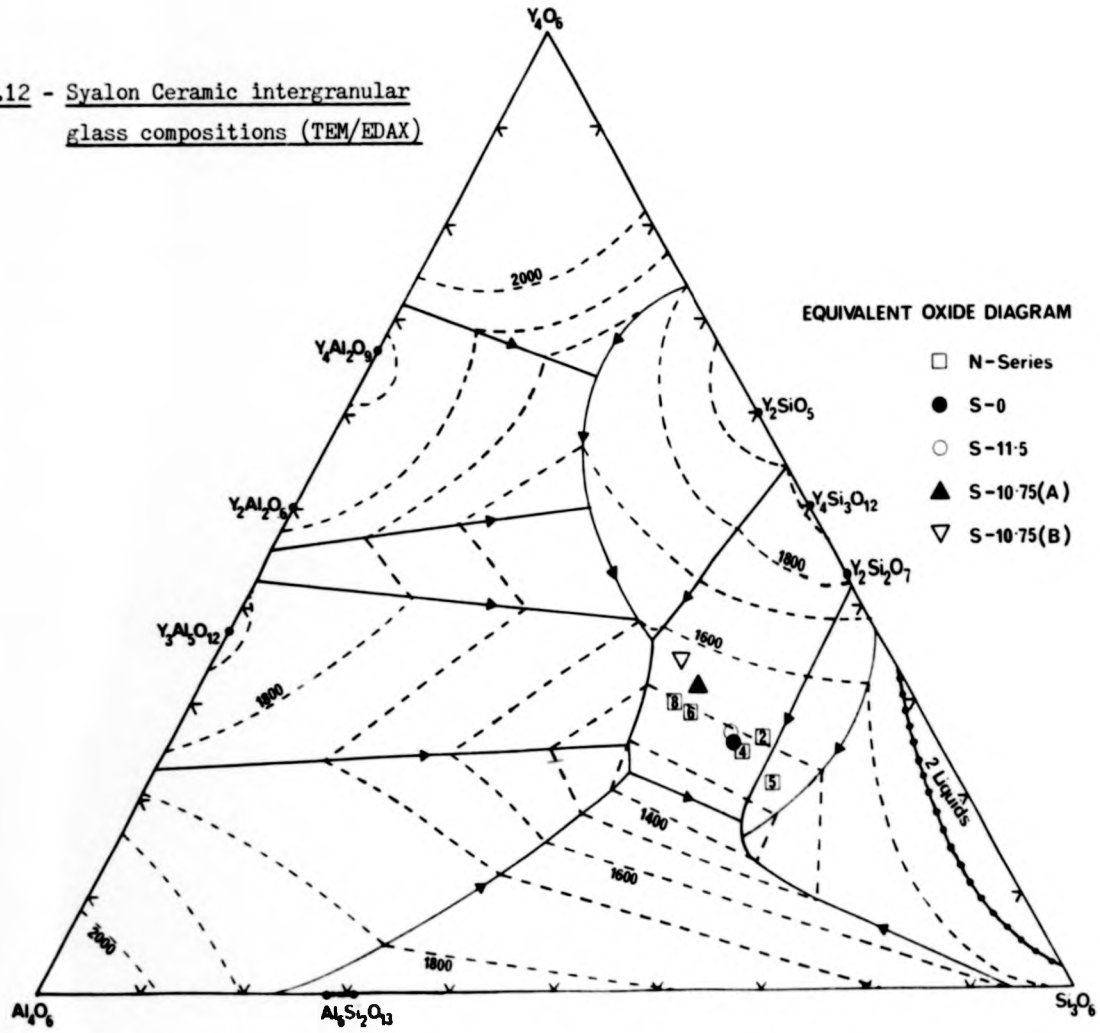

FIGURE 4.13 - Comparison of β''-SS Al_2O_3 subtitution level values obtained by calculation and by microanalysis

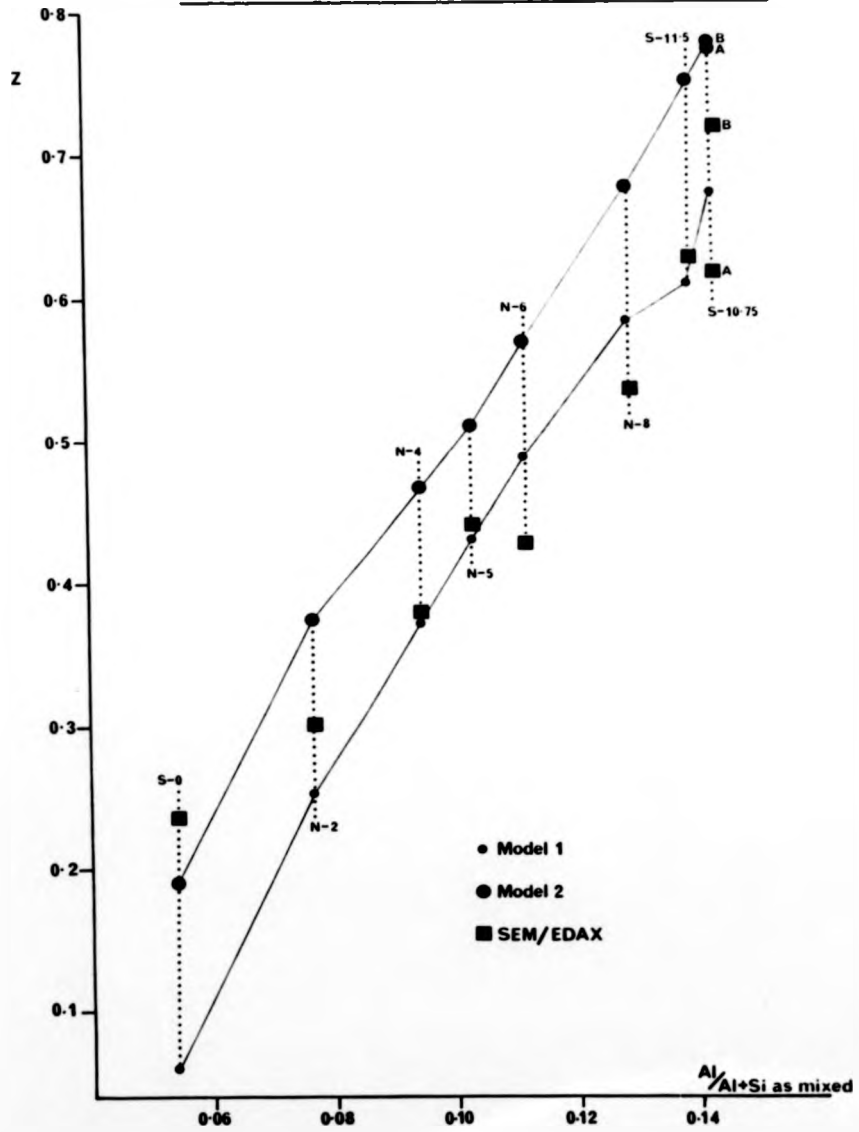

Alloy	Glass Composition from Model 2								Model 2	SEM/EDAX
	$^a\%$ Si	$^a\%$ Al	$^a\%$ Y	$^a\%$ O	$^a\%$ N	$^a\% \frac{O}{O+N}$	R'	Y'	β'_z	$\beta'_{\bar{z}}$
N-2	18.67	7.44	11.42	56.17	6.30	0.899	2.64	2.71	0.376	0.301
N-4	18.34	8.65	11.33	51.74	9.94	0.839	2.56	2.88	0.468	0.381
N-5	20.86	8.63	9.78	43.53	17.20	0.717	2.28	3.44	0.512	0.442
N-6	16.18	9.79	12.66	52.05	9.32	0.848	2.70	2.59	0.571	0.429
N-8	15.80	10.20	13.30	48.40	12.30	0.797	2.69	2.63	0.679	0.539
S-0	17.37	8.44	10.85	62.65	0.68	0.989	2.75	2.49	0.190	0.236
S-11.5	19.41	9.29	13.04	30.14	28.12	0.517	2.28	3.45	0.754	0.631
S-10.75B	15.80	9.48	15.86	37.37	21.50	0.635	2.66	2.68	0.780	0.722
S-10.75A	17.27	9.52	14.50	35.01	23.21	0.596	2.49	3.03	0.776	0.621

TABLE 4.9 - Glass and β'_{ss} compositions calculated using Model 2, assuming no losses during fabrication.

Si-Al-Y data for glass and Si-Al data for β'_{ss} from TEM/EDAX and SEM/EDAX systems respectively.

Glass Structural Parameters;

$$R' = \frac{(^a\% O + {}^a\% N)}{(^a\% Si + \frac{2}{3}\,{}^a\% Al)}, \quad Y' = 8 - 2R'$$

FIGURE 4.14

A Dependence of glass properties (Y') on nitrogen content

Arrows indicate the effect on Y' of increasing Si, Al and N contents of the intergranular glass composition.

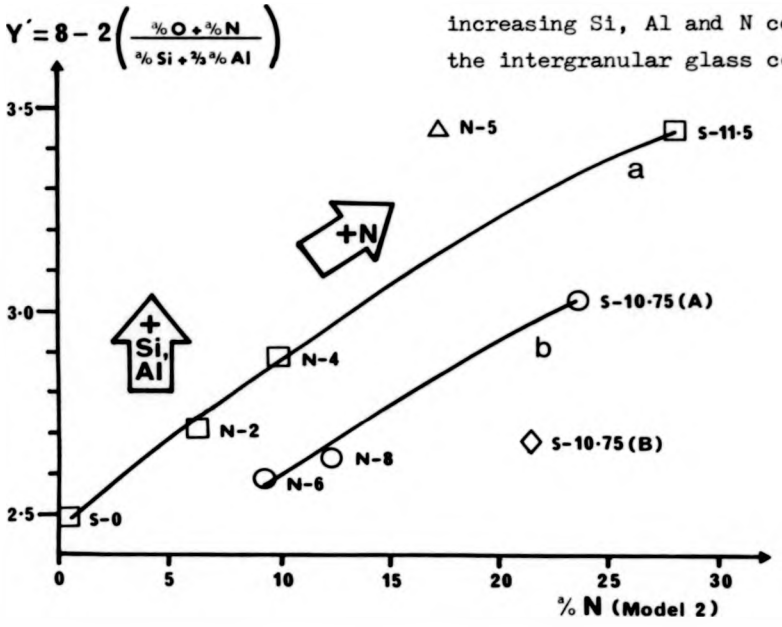

B Glass compositions

TEM/EDAX

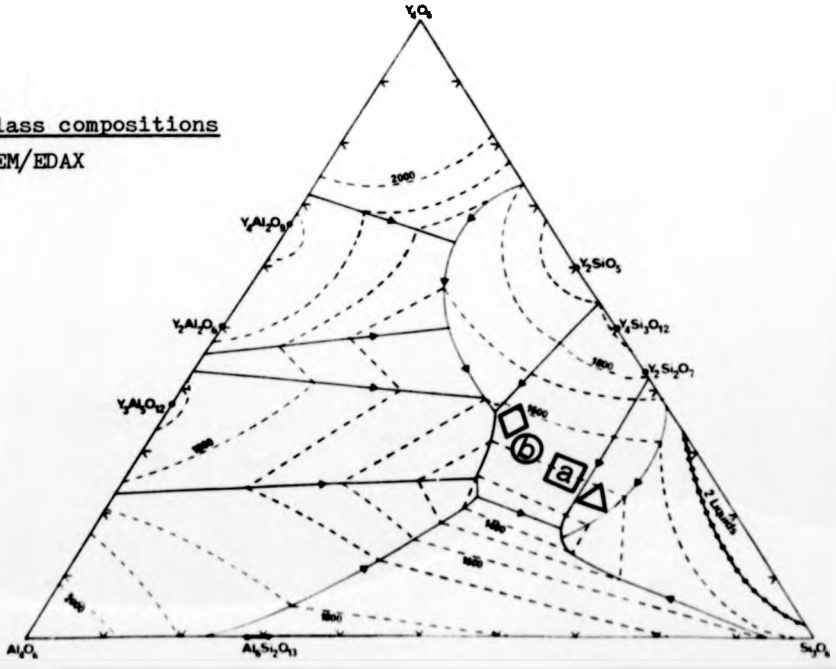

The glass forming region in the Y-Si-Al-O-N system is found to extend towards the AlN corner of the Janecke prism. This indicates that addition of N^{3-} to the glass composition allows greater solubility of Al^{3+} and vice-versa. This may increase the proportion of Al^{3+} contributing to the network structure and thus values of Y' could be higher than indicated by assumption of 2/3 structural and 1/3 modifying Al^{3+}.

The small electron absorbing pools observed in the β' grains of 21R rich alloys were subjected to x-ray microanalysis. Although the small pool size precluded quantitative analysis, it was found that these spherical inclusions were rich in yttrium and aluminium suggesting a composition similar to that of the eutectic glass.

4.2.6 Electron Energy Loss Spectroscopy results

The data acquired by EDAX from intergranular glass of the three ceramics and the two bulk reference standards is presented, as previously in the form of a normal projection onto the ternary oxide face of the Janecke prism, see Figure 4.15. Analysis A was taken from the intergranular glass of alloy S-0, B from alloy S-10.75B and C from S-10.75A. Energy loss spectra obtained from the reference bulk and Syalon Ceramic intergranular glasses are presented in Figure 4.16A, spectra from the β' phase are presented in Figure 4.16B. The 40 eV energy windows are indicated, and the area under the N K edge (A_N) and O K edge (A_O), used for derivation of composition, are made obvious by shading. The N/O ratio for each glass and analysed β' grain were calculated using the expression:-

$$N/O = 0.457\ A_N / A_O$$

and the β' z value derived using:-

$$z = \frac{8}{(N/O) + 1} .$$

Table 4.10 is a presentation of the analysed composition for each glass obtained by combining data from EDAX and EELS systems and assuming oxide stoichiometry, as presented previously[97], a further correction was then applied to adjust for charge balance (when N^{3-} replaces O^{2-}) and the parameters R' and Y' calculated.

Also presented are as-mixed compositions of the bulk glasses and intergranular glass compositions derived using Model 2. It may readily be seen that there is excellent agreement between analysed

and as-mixed results for the standard glasses. The decrease in silicon content of Glass 2 is probably due to SiO volatilisation during fabrication, since this glass was melted at a higher temperature than Glass 1 to compensate for an expected increase in viscosity associated with the higher N/O ratio.

FIGURE 4.15 - Compositions of standard and intergranular glasses

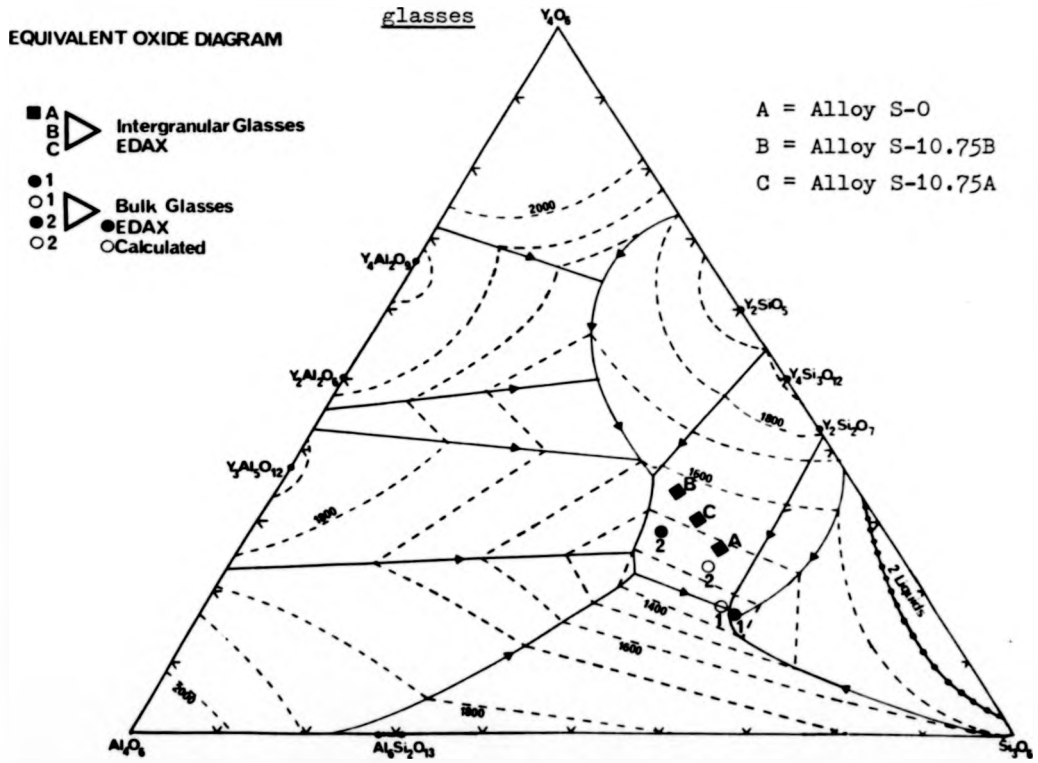

With respect to Model 2 compositions, the decrease in intergranular glass nitrogen contents described by microanalysis data leads to an expected decrease in Y', and, since the analysed data for the bulk standard glasses is in good agreement with calculated as-mixed data, there would seem to be little reason to doubt the results.

The analysed composition range of the intergranular glasses appears acceptable to the reported glass forming region in the Y-Si-Al-O-N system[47], and the range of nitrogen content displayed across all glasses (0 - 13%) lies within the range 0 - 15% in which other bulk glasses have been prepared and investigated[47],[53],[55]. Thus, Model 2 appears to overestimate the glass nitrogen content, and since it also appears to overestimate the β' z level (cf. values from

SEM/EDAX in Table 4.9), the possibility of AlN loss, or formation of a small amount of an AlN rich phase in the microstructure, presents itself. Glass compositions projected onto the ternary oxide face of the Janecke prism in Figure 4.12, derived using Model 2 are compared with compositions analysed by EELS in the normal projection onto the base plane of the Janecke prism in Figure 4.17.

The β' substitution levels derived from Al/Si analysis by EDAX and N/O analysis by EELS are compared in Table 4.10. It may be seen that EELS analysis demonstrates an increase in z over that described by EDAX, but inaccuracies arise, for analysis of nitrogen rich phases by EELS, due to interaction of the N K and O K edges causing difficulty in estimation of the background under the latter. These difficulties may be overcome by use of Fourier Transform based deconvolution programmes in a dedicated microcomputer system, but this facility was not available for use in this investigation.

FIGURE 4.16A - EELS spectra for bulk and intergranular glasses

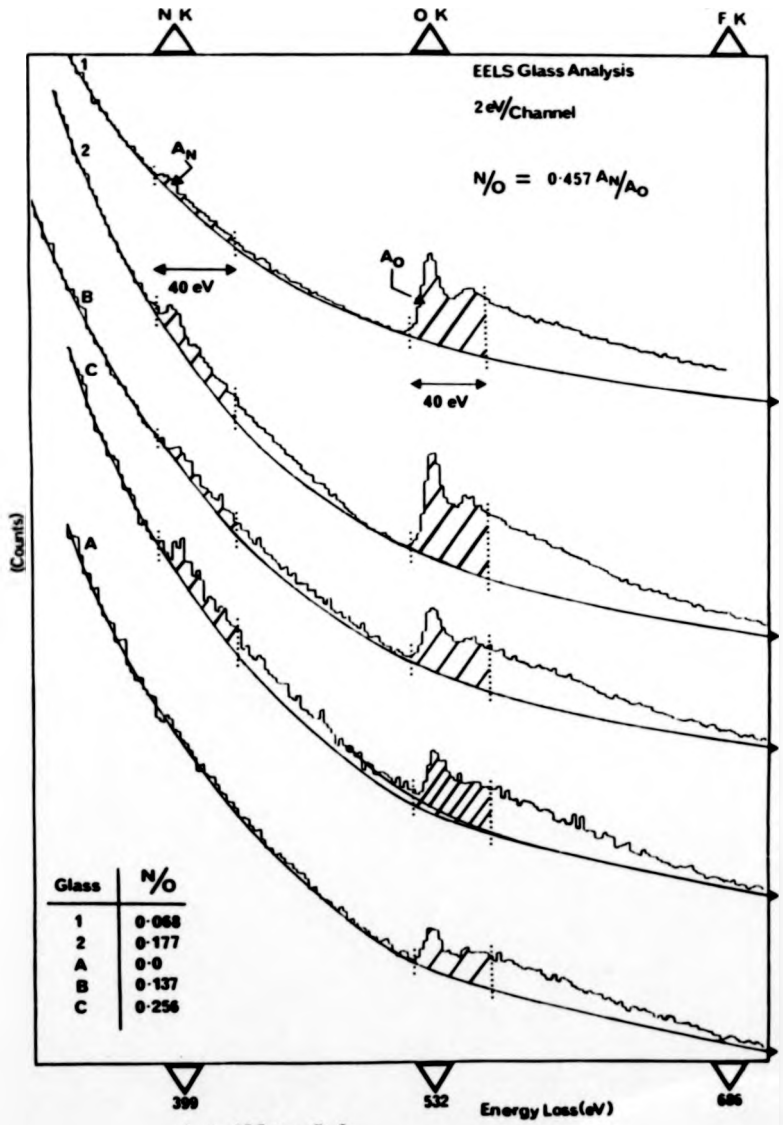

A = Alloy S-0

B = Alloy S-10.75B

C = Alloy S-10.75A

FIGURE 4.16B - EELS spectra for β' phase in Syalon Ceramics

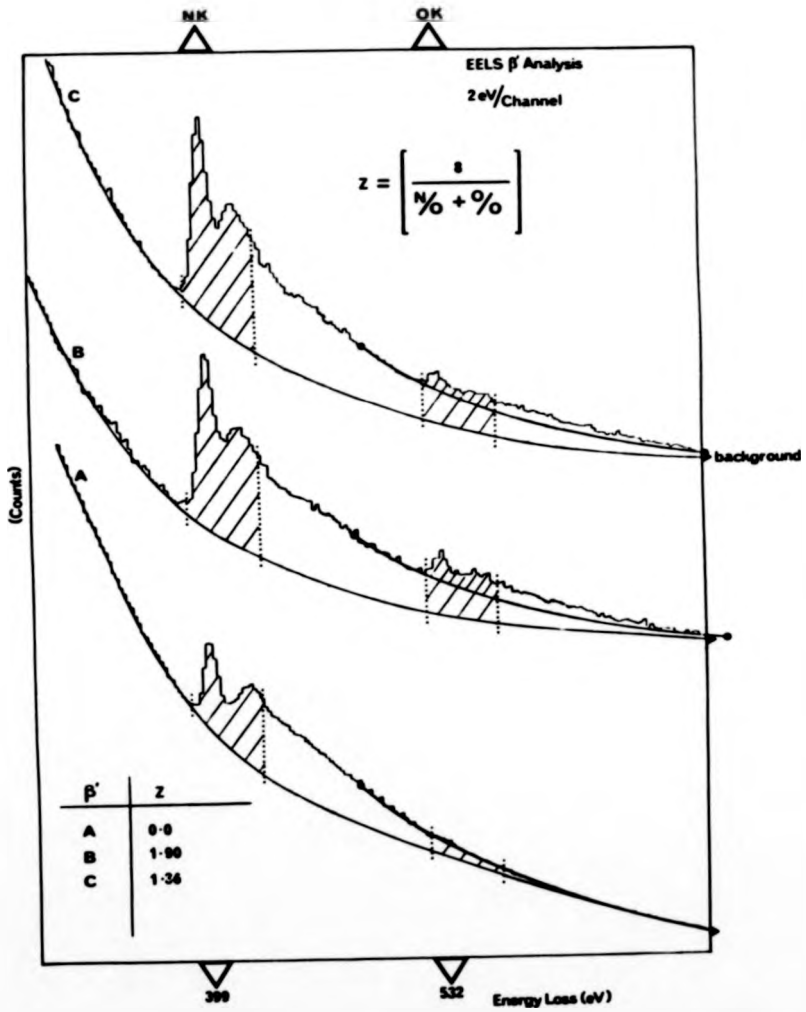

A = Alloy S-0

B = Alloy S-10.75B

C = Alloy S-10.75A

Designation	a% Si	a% Al	a% Y	a% O	a% N	R'	Y'	Comments	β' z	
Bulk Glass 1	18.984	10.202	7.632	60.010	3.077	2.45	3.11	Calculated 'as mixed' compositions	/	
Bulk Glass 2	17.736	9.940	10.765	51.620	9.940	2.53	2.95		/	
Syalon A	17.37	8.44	10.85	62.65	0.68	2.75	2.49	Calculated using Model 2	0.190	
Syalon B	15.80	9.48	15.86	37.37	21.50	2.66	2.68		0.780	
Syalon C	17.27	9.52	14.50	35.01	23.71	2.49	3.03		0.776 *	
Bulk Glass 1	19.67	9.92	7.28	59.10	4.026	2.40	3.20	Analysed compositions from EDAX and EELS spectra	/	
Bulk Glass 2	14.95	11.32	12.58	51.96	9.196	2.72	2.56		/	
Syalon A	17.37	8.44	10.85	63.33	/	2.75	2.49		0.236	0.0
Syalon B	14.80	8.86	14.90	54.06	7.42	2.97	2.06		0.722	1.90
Syalon C	16.40	9.03	13.76	48.43	12.38	2.71	2.58		0.621 **	1.36 ***

TABLE 4.10 - Compositional Data for Standard Bulk Glasses and Syalon Ceramic Intergranular Glasses.

Syalon A = Alloy S-0, Syalon B = Alloy S-10.75B, Syalon C = Alloy S-10.75A

Data for Syalon β' phase; * Calculated using Model 2

** Analysed using SEM/EDAX

*** Analysed using TEM/EELS

FIGURE 4.17 - Projected intergranular glass compositions onto the isothermal phase diagram for the system Si_3N_4 - AlN - Al_2O_3 - SiO_2 at 1760°C

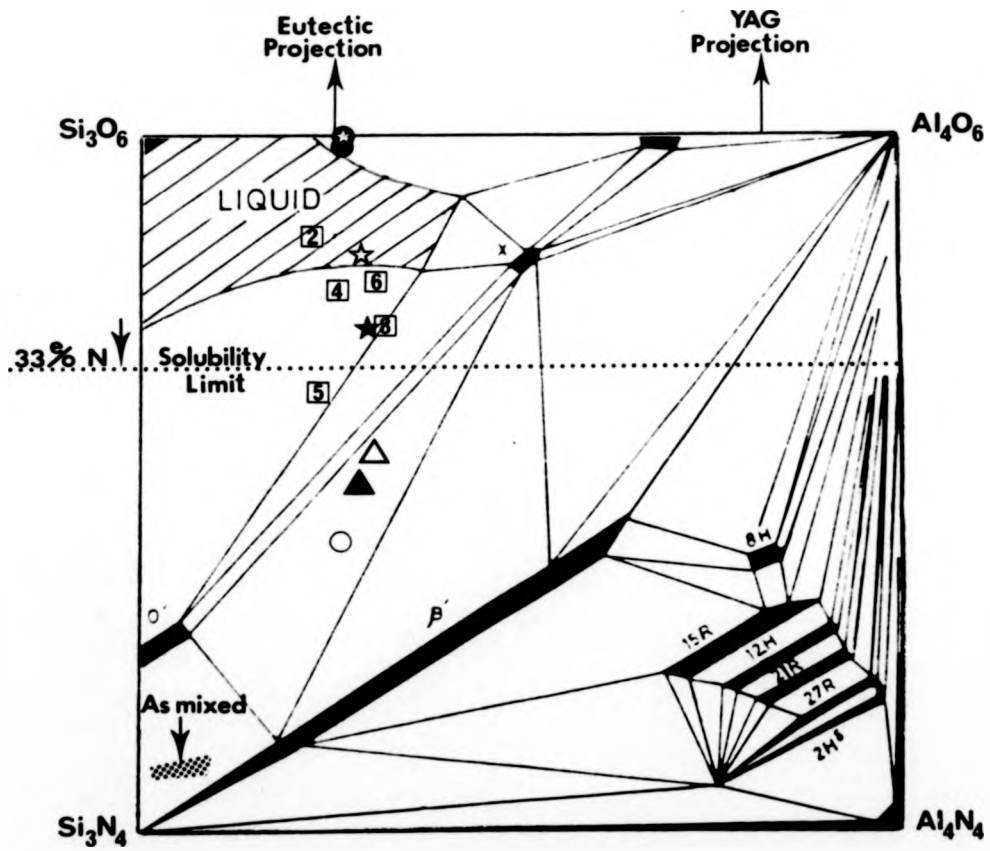

Model 2 compositions;

- □ N-Series
- ● S-0
- ○ S-11·5
- ▲ S-10·75 (A)
- △ S-10·75 (B)

EELS Analysis;

- ✪ S-0
- ★ S-10·75 (A)
- ☆ S-10·75 (B)

4.3 Discussion - The relationships between composition and microstructural character of Syalon Ceramics

The properties of ceramics, discussed in the next two chapters, must depend upon their microstructural character which is derived during sintering and therefore compositionally dependent, as discussed in Chapter 2. The results obtained in this chapter must therefore be discussed with reference to the observed sintering behaviour previously considered.

4.3.1 The relationship between liquid composition, during sintering, and the resulting value of z in the β'_{ss}.

Increasing the aluminium content of the sintering liquid by addition of 21R polytypoid is seen to directly increase the aluminium substitution level of the β'_{ss} denoted by z. Prediction of the value of $\bar{z}$, for ceramics sintered under similar conditions to those described here, is possible using the empirically derived relation:-

$$\bar{z} \approx (0.035\ ^{w}\!/_{o}21R) + 0.24$$

as presented in Figure 4.9. This tendency, over the duration of the $\alpha \rightarrow \beta'$ conversion, must move the mean composition of the potential liquid forming component towards the eutectic trough of Figure 2.7, by removal of excess aluminium. However, removal of oxygen from the liquid occurs simultaneously with aluminium uptake into β' and this must lead to a reduction in liquid volume and increased concentration of nitrogen. In effect, formation of intermediate YAG, observed using XRD[46], removes excess aluminium from the system at low temperatures, enabling formation of a more near eutectic composition liquid, of low viscosity, in which liquid phase sintering may initiate. As temperature is increased dissolution of the YAG occurs, yttrium decreasing liquid viscosity and aluminium being available for solution in the β'.

4.3.2 Liquid composition and resulting glass nitrogen contents

Calculations (Model 1A) indicate a heavy nitrogen oversaturation in the sintering liquids of alloys compounded with large 21R additions. Thus, loss of nitrogen to the surroundings is expected in these cases, hence, the results of EELS indicate a lower nitrogen level in these glasses than predicted using Model 2.

This effect may also account for some of the inherent porosity observed in as-sintered ceramics prepared with high 21R additions, the nitrogen possibly forming bubbles, on cooling after sintering, as its saturation limit in the liquid decreases. Therefore, especially in the case of high 21R addition, some overestimation of the parameter Y' is probable.

However, formation of α' phase was noted in alloys S-10.75A and B (SEM) and S-11.5 (SEM and XRD), of which the liquids contain high theoretical nitrogen contents during sintering. This yttrium stabilised phase has been found to exist as a solid solution along the tie line Si_3N_4 - 0.1 Y_2O_3 : 0.9 AlN in the high nitrogen region on the plane Si_3N_4 - Y_2O_3 - AlN of the Janecke prism[98]. Since this phase requires high nitrogen contents for formation from sintering liquids, nitrogen loss before the final cooling stage must be minimal and removal of some nitrogen from the liquid into α' accounts for some of the observed decrease in glass nitrogen content. Thus limitations have been demonstrated in the accuracy of data calculated using Models 1, 1A and 2, and the derived parameters R' and Y', but the general trends illustrated by this data are still applicable, as demonstrated by microanalysis.

4.3.3 Comparison of alloys S-10.75A and S-10.75B

Alloys S-10.75A (1750°C sinter) and S-10.75B (1700°C) were fabricated from a single parent composition S-10.75, and thus any compositional variation must derive from their different sintering temperatures. As expected, the β' phase of ceramic B, sintered at the lower temperature, was found to exhibit a higher value of $\bar{z}$. This effect is derived from the lower solubility of aluminium in the liquid phase at lower temperatures, thus more is taken into the β'_{ss}. Although oxygen is also taken into the β', in association with aluminium, and this concentrates the nitrogen content of the liquid phase, a reduced nitrogen content is demonstrated in the intergranular glass of alloy S-10.75B compared to S-10.75A. This effect is due to the higher β' volume present in alloy B which primarily reduced the contents of silicon and nitrogen in the sintering liquid leaving a residue for glass formation relatively rich in yttrium and oxygen.

The general observation, made across the range of alloys, is that glass nitrogen content and $\bar{z}$ of the β' are seen to increase

together as 21R content increases, and associated with this effect is a tendency towards dark colouration. Since S-10.75A is considerably darker than alloy S-10.75B, in the as-sintered state, it is reasonable to associate the darkening colouration with increased nitrogen levels in the intergranular glass.

Nb. this is a seperate effect to that described in Section 4.2.3, in which light and dark bands at the billet surface are described, where the contrast arises due to light scattering at regions of porosity.

There does not appear to be a simple relationship between intergranular glass volume fraction and optical darkness.

The higher sintering temperature applicable to alloy S-10.75A, which causes generation of a larger liquid volume, also leads to more rapid and less restrictive growth of β' grains. There is also the possibility of more Ostwald ripening than occurs in alloy S-10.75B.

4.3.4 Composition and intergranular glass volume fraction

The relationship of increasing glass volume, in as-sintered ceramics, with increased as mixed oxygen content has been demonstrated (Section 4.2.4), but it was also noted that increasing the yttrium content also enhances glass volume. Accounting for this factor enables reasonable prediction of glass volume fraction, V_g, from a known composition, as presented in Figure 4.18 and represented by the empirically derived relation:-

$$V_g\% \equiv A\% \approx [4.736\ \%(Y + O)] - 34.692$$

It should be noted that this equation only holds for ceramic alloys sintered under similar conditions ($\sim$1850°C/1 hr.) and therefore may not apply to alloys S-10.75A and B, although good agreement with the relationship is demonstrated by alloy N-5.

4.3.5 Characterisation of the β'_{ss} with relation to sintering behaviour

The unit cell parameters of β', as monitored using XRD, and the z level of the β', as determined by EDAX, may be related as in Figure 4.19. The data points denoted by squares with vertical error bars are taken from work presented in the literature[66], and the data denoted by circles is extracted form Table 4.7 and Figure 4.9. The horizontal error bars represent standard errors calculated from EDAX data but vertical error bars have not been applied since uncertainty in a and c is rather large and the zero adjustment procedure,

FIGURE 4.18

Alloy	N-2	N-4	N-5	N-6	N-8	S-0	S-10.75	S-11.5
$^{a}\%(O+Y)$	9.102	9.295	9.391	9.488	9.681	10.049	9.294	8.78
A %	8.40	9.30★	9.81	10.25★	11.14	12.79	9.30★	7.34

★as determined from graph.

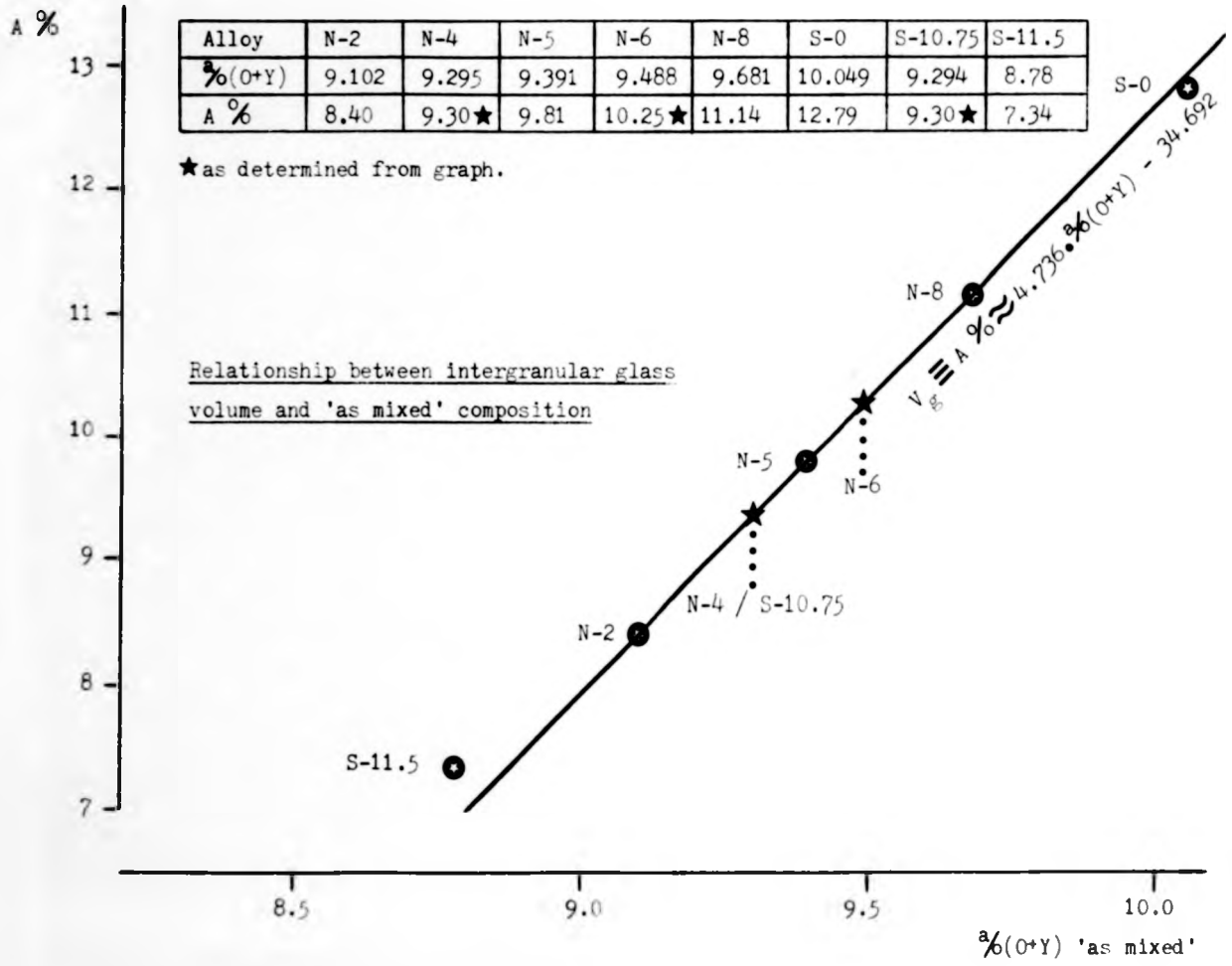

Relationship between intergranular glass volume and 'as mixed' composition

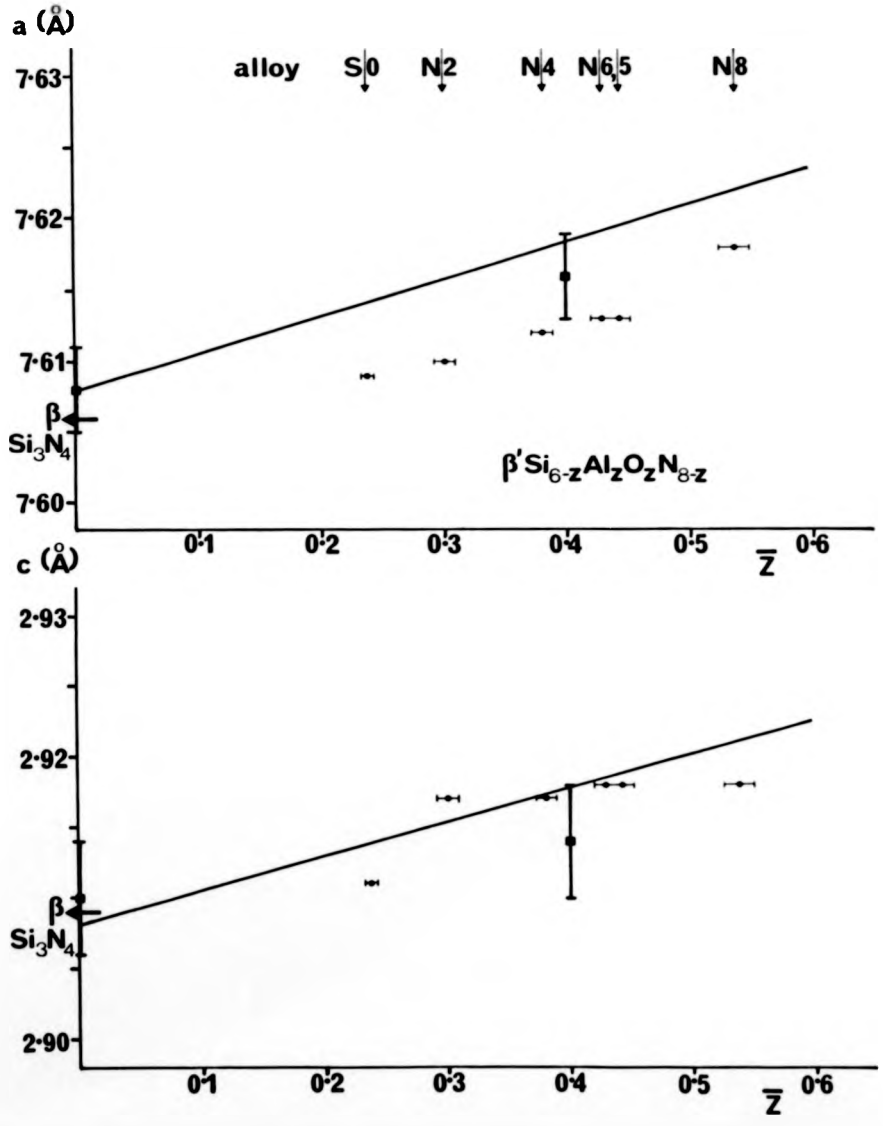

FIGURE 4.19 - The change in unit cell parameters, a and c, with Al_2O_3 substitution level, z, in the β' phase

The solid lines and data points denoted by squares with vertical error bars are taken from the literature[66]. Data points denoted by circles with horizontal error bars were obtained by XRD and TEM/SEM/EDAX analysis.

described in Section 4.2.2, was used.

The results of this analysis may be seen to be in good agreement with the plots described by the lines and taken from various alloys completely spanning the range of alumina solid solution in β-Si_3N_4[66].

The presence of small glass pools in occasional large β' grains in some alloys may be related to the formation of intermediate YAG, although it is felt unlikely that YAG and β' mutually promote epitaxial growth (see Section 5.4.2). Another possibility is that small amounts of YAG or yttrium rich liquid phase may be trapped between small silicon nitride grains (α or α', or β or β') which may promote epitaxial β' growth and subsequently form one large grain. Such grains would rapidly become homogeneous in terms of structure and chemistry except for the entrapped yttrium rich phase, which becomes rounded in outline in order to reduce surface energy.

A monomodal β' grain size distribution is exclusively exhibited by alloy S-0, all other ceramics being characterised by a bimodal distribution, seen by consideration of micrographs obtained from the SEM. This effect also relates to liquid phase volume, composition and properties, during sintering, and the conclusions of Chapter 2 lead to the following summary of sintering behaviour for ceramics fabricated with low or high polytypoid contents.

(a) Alloy S-0 sintering scenario

Primary rearrangement begins at low temperatures (1300 - 1400°C) with significant densification occuring before initiation of the $\alpha \rightarrow \beta'$ transformation. At the sintering temperature ($\leq$ 1850°C) diffusion rates are high in the large liquid volume of near eutectic composition, and Ostwald ripening may occur to a great extent, removing most of the small grains originally formed in the microstructure. On cooling, a large volume of liquid remains in the form of intergranular glass.

(b) Alloy S-11.5 sintering scenario

Primary rearrangement accounts for an insignificant amount of densification before onset of the $\alpha \rightarrow \beta'$ transformation, which occurs slowly due to low diffusion rates through a relatively small volume of liquid phase, of high viscosity, oversaturated in nitrogen. Some formation of α' occurs while most excess aluminium (and oxygen) is taken into the developing β' grains. The number of small β' grains produced is high due to the large amount of constraint

provided by contiguity with other grains in the relatively small liquid volume. Full densification is achieved, but the time remaining for Ostwald ripening is short and this stage of sintering contributes very little to the character of the microstructure. Thus, a bimodal grain size is observed in the cooled microstructure and the low intergranular glass volume of high nitrogen content relates to the composition of the sintering liquid.

(c) Other alloys

Ceramics of composition intermediate to the alloys S-0 and S-11.5 undergo a sintering behaviour which is intermediate in format and exhibit a trend in microstructural character, as discussed.

4.3.6 Summary

The relationships between as mixed composition, sintering behaviour and resultant microstructural character of a range of Syalon Ceramics have been presented and discussed.

A full definition of the microstructure present in selected ceramic alloys has been presented and this data will allow an understanding of the behaviour of these materials when subjected to elevated temperatures and sub-critical stress at elevated temperatures.

CHAPTER 5.- The microstructural evolution of Syalon Ceramics during heat-treatment

In this chapter the results of a brief investigation of Syalon Ceramics heat-treated by dwell upon cooling from the sinter temperature are reported. A study designed to further elucidate the dependence of intergranular glass crystallisation behaviour upon composition and temperature is then presented in four main sections. The introductory sections detail the construction of heat-treatment furnaces and experimental techniques used, the third section is a presentation, with brief discussion, of the results obtained. In the fourth section the results are summarised and further discussed.

5.1 Post-sinter heat-treatment during fabrication

A previous investigation of Syalon Ceramics[38] indicated that devitrification of the intergranular glass, to YAG, was possible on heat-treatment at 1400°C. In an attempt to reproduce this effect in alloys N-2, N-4, N-6 and N-8, billets were sintered in the normal manner except that the cooling 'ramp' was interrupted with a 5hr. 'dwell' at 1400°C. Specimens were taken from the bulk of these billets and examined as follows:-

5.1.1 Density, XRD and Optical examination

In general the specimens appeared darker, in reflected light, than as-sintered materials of the same nominal composition, and some bars from alloys of higher 21R content exhibited 'dark spots' of diameter ~ 1mm.

Density measurements obtained from heat-treated bars are presented in Table 5.1, and when compared with data from as-sintered material it may be seen that, except for an apparent decrease in the density of alloy N-2, there is no significant change of density, within limits of error.

Results from XRD indicated the presence of YAG (ASTM card 8-178) in alloys N-4, N-6 and N-8. The β'-SiAlON reflections exhibited the intensity profile characteristic of as-sintered N-source materials, and no extra reflections were obvious.
NB. Heat-treatment of similar ceramics at 1400°C/5hrs.[66] produced YAG crystallisation and an extra reflection observed was assigned to

simultaneous Si_3N_4 crystallisation. A commensurable observation was a subsequent decrease of 0.005Å in the β'-SiAlON lattice parameter after heat-treatment for 10hrs., interpreted as homogenisation of the solid solution.

A comparison of data for β' cell parameters and crystal size before and after heat-treatment is compiled as Table 5.2. Considering the large limits of error applicable no significant variation can be attributed to heat-treatment. However, prolonged heat-treatment time may be expected to lead to changes in these parameters[66]. The position of YAG reflections indicated a zero shift of $\sim 0.125^{\circ}$ θ to be applicable to x-ray spectra of both heat-treated ceramics, this is in good agreement with the calculated shift, $\Delta\theta$, and lends support to the method used for evaluating the cell parameters a and c.

TABLE 5.1 - Density data for 'as-sintered' and heat-treated bars

Alloy	N-2	N-4	N-6	N-8
Density $g.cm^{-3}$ 'as-sintered'	3.229	3.226	3.241	3.236
Density $g.cm^{-3}$ 1400°C/5hrs.	3.170	3.222	3.236	3.240

(an error of ± 0.01 $g.cm^{-3}$ is applicable.)

TABLE 5.2 - β' SiAlON cell parameters and crystal sizes (XRD)

Alloy	aÅ	cÅ	$\Delta\theta^{\circ}$	D_{hkl} (μm) ± 25% (200)	(101)	(210)
N-6 'as-sintered'	7.613	2.918	+0.058	0.33	0.28	0.33
N-8 'as-sintered'	7.618	2.918	-0.155	0.27	0.21	0.24
N-6 1400°C/5hrs.	7.611	2.917	-0.153	0.28	0.25	0.25
N-8 1400°C/5hrs.	7.614	2.918	-0.148	0.30	0.28	0.31

5.1.2 Electron Microscopy and X-ray Microanalysis

The post-sinter heat-treated alloys were examined in the SEM and the dark 'spots', observed optically, were related to areas of YAG crystallisation and enhanced intergranular porosity.* EDAX was used to assess the Al_2O_3 substitution level, z, of the β' phase and the results are presented in Table 5.3. The data suggests a decrease in β' aluminium concentration during 1400°C/5hr heat-treatment of alloys N-2 and N-4,

* see Figure 5.14

but no change for alloys N-6 and N-8.

TABLE 5.3 - z in $Si_{6-z}Al_zO_zN_{8-z}$ obtained from as-sintered and 1400°C/5hr post-sinter heat-treated ceramics (SEM/EDAX)

Alloy	$\bar{z}$ ± e 'as-sintered'	$\bar{z}$ ± e 1400°C/5hrs.
N-2	0.301 ± 0.008	0.270 ± 0.004
N-4	0.381 ± 0.009	0.369 ± 0.003
N-6	0.429 ± 0.009	0.430 ± 0.010
N-8	0.539 ± 0.012	0.537 ± 0.010

(e = standard error)

The intergranular phase of alloys N-4, N-6 and N-8 provided microanalysis spectra compatible with the composition of YAG ($\sim Y_3:Al_5$), and no glassy pools were obvious, by atomic number contrast, in the backscattered electron mode. Further analysis in the TEM, using SAD and EDAX, confirmed the presence of YAG, in agreement with XRD, and this phase was found to be present in the same diffracting condition (ie. crystallographic orientation) over large areas, despite interference by the dominating volume of β' phase. This observation is indicative of a low nucleation density for YAG in these materials.*

Occasional small pockets of uncrystallised glass were observed in alloy N-4 at β' grain junctions, but alloys N-6 and N-8 appeared to be completely crystalline β'/YAG composites. The possibility of a very thin glassy layer being present at β'/YAG interfaces was demonstrated using the dark field diffraction technique previously promoted[96], but the validity of this evidence is contentious, the effect possibly arising via diffuse scattering along regions of relative disorder at the boundaries.

Alloy N-2 proved to contain a glassy intergranular phase which was depleted in SiO_2 by ~ 2% compared to the as-sintered glass composition. Rare areas, a few μm in diameter, were detected, in which crystallisation of a phase of nominal analysis 3% Al, 51% Si, 46% Y had occurred in the intergranular matrix. This phase was also identified in alloys N-4 and N-6, where its occurence was also rare and thus is not expected to greatly affect compositional balance. The analysis is consistent with a slightly aluminium substituted Y-N-α Wollastonite ($Y_3Si_3O_6N_3$) or an yttrium disilicate ($Y_2Si_2O_7$) polymorph.

* see figure 5.0

FIGURE 5.0 - Alloy N-4 microstructure after deformation at 1300°C in the compressive creep mode

Complete crystallisation of the intergranular glass, to YAG of constant orientation over large areas, is observed. 'Morphological stabilisation' of the YAG phase, resulting in a discontinuous phase distribution, then occurs. Compare with Figure 4.10 (glassy matrix).

FIGURE 5.0 - Alloy N-4 microstructure after deformation at 1300°C in the compressive creep mode

Complete crystallisation of the intergranular glass, to YAG of constant orientation over large areas, is observed. 'Morphological stabilisation' of the YAG phase, resulting in a discontinuous phase distribution, then occurs. Compare with Figure 4.10 (glassy matrix).

The decrease in glass Si^{4+} content, analysed for alloy N-2 after heat-treatment, cannot be ascribed solely to crystallisation of Si_3N_4, despite evidence from XRD for a decrease in β' z parameter. Using Model 2 (see Chapter 4) a fall of 0.008 is expected in z for the variation in glass composition measured, cf. 0.031 indicated using SEM/EDAX.

Nb. the glass structure parameter Y' is also expected to change from 2.71 to 2.47 due to this variation in composition.

Another possibility is crystallisation of Si_2N_2O, occasional highly faulted grains typical of this phase were observed in the microstructure, EDAX providing evidence for a small aluminium substitution.

In order to further explore the crystallisation behaviour of Syalon Ceramics a heat-treatment programme was initiated and will next be described.

5.2 Construction, calibration and performance of heat-treatment furnaces

Two tube furnaces were used for heat-treatment of ceramic specimens, one available commercially (Carbolite Ltd. Sheffield) and the other built specifically for use in this research programme.

The commercial furnace consisted of a horizontal 'Recrystallised alumina' tube surrounded by four SiC resistance heating elements, this assembly was insulated with ICI Safil fibre board and furnace bricks, contained in a Sindanyo box. Heating was effected via a Eurotherm Type 070 controller and Pt-13%Rh /Pt thermocouple. Radiative heat loss was minimised by facing the tube ends with MI28 refractory brick (Morganite Ltd.), but free movement of air, from the laboratory surroundings, over the specimens, was not greatly restricted.

The second furnace (see Figure 5.1) was designed to enable a choice of heat-treatment atmosphere, from air, various bottled gases and vacuum to 10^{-5} Torr. A vertical 'Recrystallised alumina' tube was sealed, with 'O' rings, to valve assemblies at each end. Heating was provided by a SiC dual spiral muffle resistance heating element (Crusilite Type DM), which surrounded the specimen/atmosphere containment tube, and the whole assembly was surrounded with ICI Safil insulation contained in a Sindanyo box. The element was powered by a Eurotherm Type 070 controller via a variac and temperature measurement made using a Pt-13%Rh /Pt thermocouple. A rotary/diffusion pump system was connected to the bottom valve of the containment tube.

FIGURE 5.1 - The heat-treatment furnace

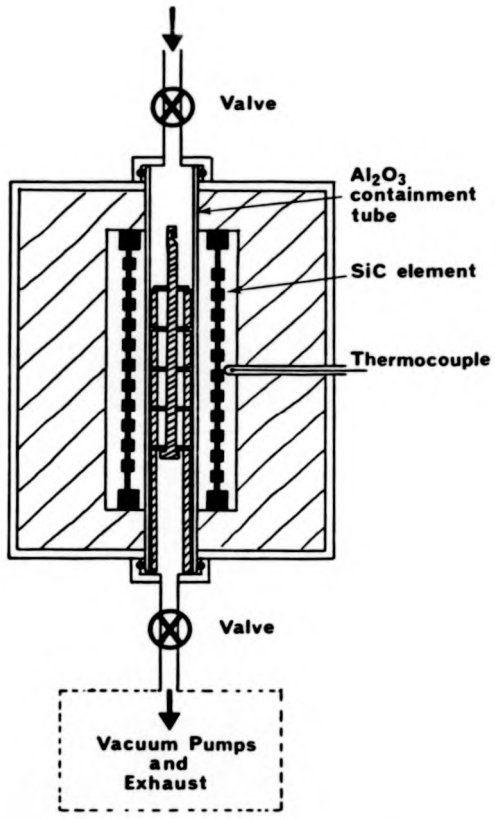

To minimise reaction with the specimens the support shelves were machined from a block of single phase non-cavitating HPSiAlON and the shelf supports and central rod were machined from Recrystallised alumina. The specimens and supporting system were lowered into, and retrieved from, the furnace using a wire noose.

Using a standard Pt-13%Rh /Pt thermocouple and potentiometer, both furnaces were calibrated over the temperature range 800-1550°C in 50°C increments and the 'heat zone',defined as the volume at desired temperature ± 10°C, was located at the various temperature levels. Stability of temperature level was monitored over long time periods (~100 hrs.) to ensure freedom from thermal drift.

5.3 Experimental detail

Alloys S-0, S-10.75A and B were provided (courtesy of Lucas-Cookson Syalon Ltd) in the form of half-billets of approximate dimensions as shown in Figure 5.2 All other alloys were provided in the form of $(3x3)mm^2$ cross-section rectangular bars of varying lengths.

FIGURE 5.2 - Approximate dimensions of Syalon Ceramic half-billets

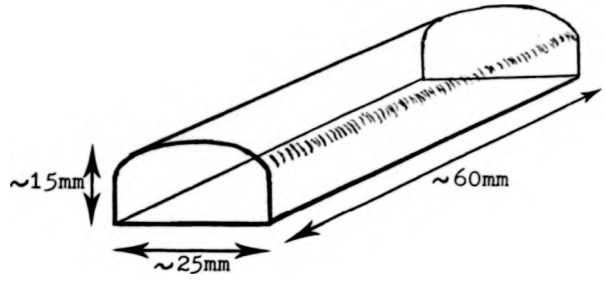

Using a diamond slicing wheel mounted on a cutting machine (Jones and Shipman Ltd.) similar rectangular bars were sliced from the half-billets, and samples of all alloys were machined in the form of cubic specimens of, side ~3mm. After grinding to an '800 grade' finish using SiC laps the specimens were notched for identification using a diamond loaded file. A specimen of each alloy was ultrasonically cleaned in acetone, loaded onto the HPSiAlON shelves in the specimen holder and the whole assembly was lowered into the heat-treatment furnace.

Before treatment under a nitrogen atmosphere the furnace was evacuated and then backfilled with gas. A slight overpressure was maintained throughout heat-treatment to minimise leakage of oxygen into the furnace.

For heat-treatment in air the containment tube top seal was removed and the tube end loosely faced with aluminium foil and furnace brick, to prevent radiative heat loss. The bottom valve was left open allowing some convective air flow past the specimens. Some air heat-treatments were performed in the commercial furnace previously described in Section 5.2.

Periodically furnace temperature was measured to ensure calibration and stability of the heat zone, and temperatures were measured at least every 24 hrs. during long heat-treatments to ensure freedom from thermal drift.

Specimens heat-treated under nitrogen were cooled by switching off the heating power and flushing nitrogen through the furnace, while cooling after heat-treatment in air was achieved by removal of the specimens from the furnace and leaving them to stand in static air.

The small specimen size and presence of oxidised surface layers precluded sensible assessment of density, thus no measurements were made, although heat-treatment of larger specimens was possible for alloys S-0, S-10.75A and B.

Investigation of 'surface' and 'bulk' behaviour was pursued in the same progressive manner as detailed for characterisation of alloys in the as-sintered state. The results of optical and electron microscopy and x-ray analysis are presented in the next section. Most of the results were obtained from S- and N-series alloys described in Chapter 4, for which the as-sintered microstructural state has been fully defined. However, inclusion of results from other, only partially characterised, alloys is made.

5.4 The results of heat-treatment

5.4.1 Interaction between Syalon Ceramic and heat-treatment atmosphere

This sub-section serves only to confirm that environmental interaction with Syalon Ceramics takes the same form as proposed in the literature[68],[69],[70],[71]. A more complete study of oxidation behaviour was completed as a seperate part of the Syalon Ceramic Research Programme and is presented elsewhere[99]. An understanding of the changes induced by atmospheric interaction under heat-treatment is necessary for full appreciation of the effects described in the matrix crystallisation and creep performance sections of this thesis, and thus a brief review has been presented (see Section 3.1.2). The results of XRD and x-ray microanalysis in the SEM performed on specimens heat-treated under various atmospheres will next be described.

(a) Interaction under Argon atmosphere

Specimens of S-0 and S-11.5 were simultaneously heat-treated for 20 hrs. under an atmosphere of 'five nines argon' at temperatures of 1200, 1300 and 1400°C. All specimens heat-treated at 1200°C exhibited porous and roughly textured surfaces on which β' grains were surrounded by glass rich in yttrium and aluminium. The rough texture

was maintained on specimens heat-treated at 1300°C, but, using XRD and SEM tecniques, small round patches of YAG were readily identified growing as plates on the surface. Further increase of temperature to 1400°C led to enhanced volume of YAG formation, ~50% of the surface of S-11.5 being covered by large, non-faceted, plates of YAG with occurence of β' grains at their edges. Occasional polyhedral YAG crystals, of diameter ~5μm, were observed scattered on the surface of both ceramic alloys and the relative composition $Y_3Al_{4.5}Si_{0.9}$ was derived from them using EDAX. However, an overestimation of low silicon contents in material predominantly composed of yttrium and aluminium is caused due to an error in the software, and manual correction implied a metal ion composition $Y_3Al_{4.5}Si_{0.6}$. Similar analyses were obtained fom the plates of YAG, see Figure 5.3.

The simultaneous substitution of Si^{4+} and N^{3-} for Al^{3+} and O^{2-} in YAG has been proposed[38], this implies a general composition $Y_6Al_{10-x}Si_xO_{24-x}N_x$, and the limit for such substitution has been described by the formula $Y_3Al_{4.6}Si_{0.4}O_{11.6}N_{0.4}$[100]. As expected, the surface morphologies described are not typical of passively oxidised Si_3N_4-based material, although migration of the intergranular phase to the surface still occurs, the specimens being very weak due to porous sub-surface regions.

(b) Interaction under Nitrogen atmosphere

Standard grade bottled nitrogen was used, however the small oxygen content present as impurity usually led to passive oxidation behaviour as described below. The oxidised surface of all alloys was characterised after heat-treatment at various temperatures up to 1400°C. The atmosphere/scale interface was found to be covered with β-$Y_2Si_2O_7$ crystals, of various morphological character, surrounded by a glass rich in silicon and aluminium, as described in the literature[71],[75]. Some β-$Y_2Si_2O_7$ crystals were identified throughout the glass scale thickness although the majority were concentrated on the outer surface. The immediate sub-surface exhibited a large degree of inter-β' porosity due to extraction of the intergranular glass on oxidation, and further into the bulk lay unoxidised material of which the character varied across the range of alloys examined, depending upon initial intergranular glass volume and composition.

The presence of mullite ($Al_6Si_2O_{13}$) crystals was also demonstrated on the extreme scale surface of alloys S-10.75A and B, S-11.5, N-6 and N-8 after heat-treatment above 1200°C, for longer time

A - S-11.5

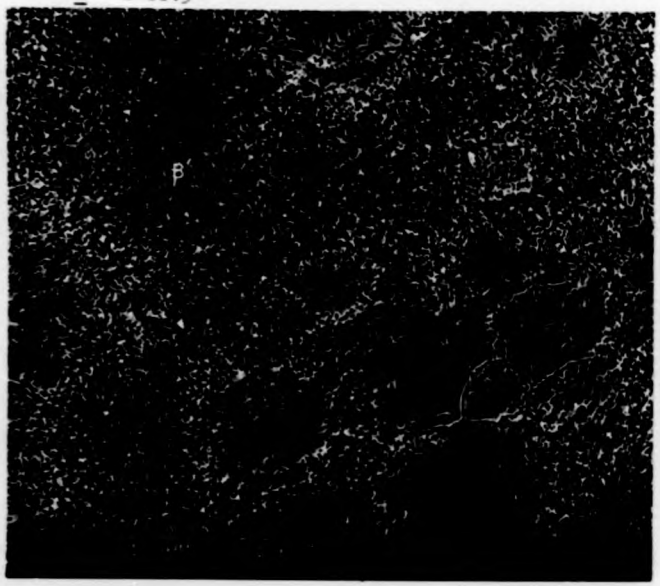

B - S-0

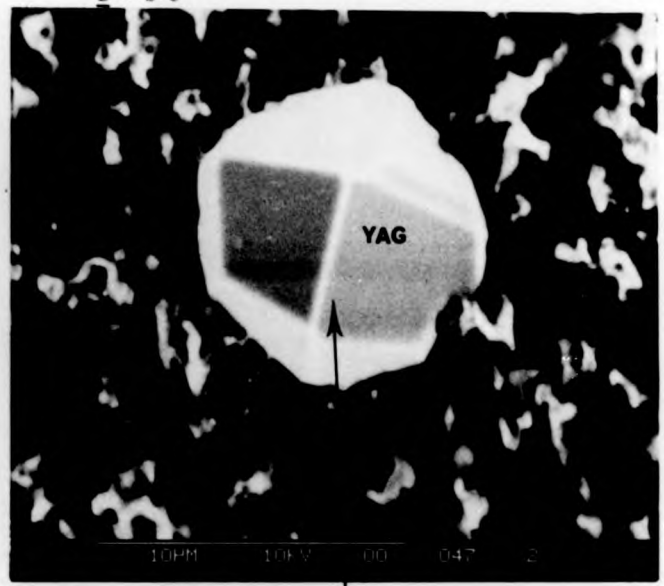

C

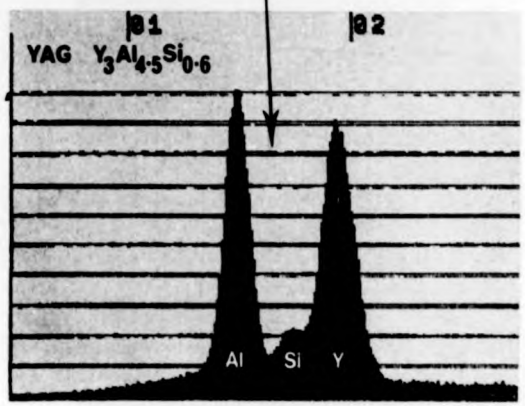

FIGURE 5.3 - YAG formation on actively oxidised Syalon Ceramic surfaces

Micrographs and analysis from the SEM/EDAX system:-

A - Alloy S-11.5, 1400°C/20 hrs. Ar atmosphere

B - Alloy S-0, 1400°C/20 hrs. Ar atmosphere

C - EDAX spectrum from YAG polyhedron

A - S-11.5

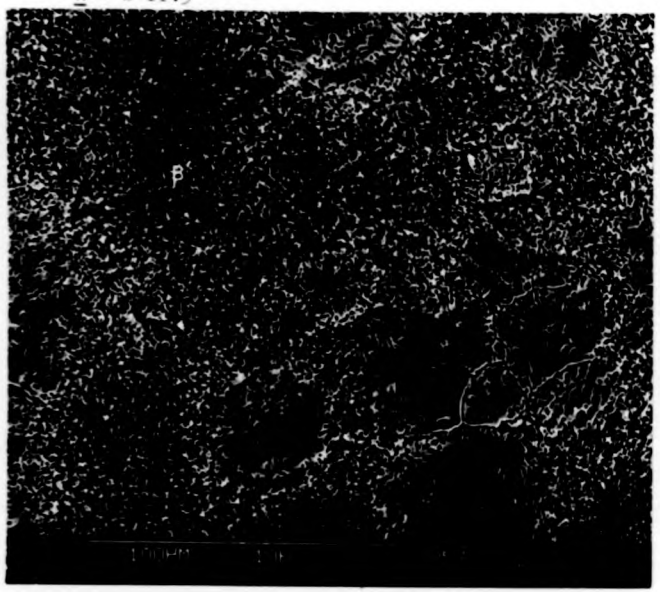

B - S-0

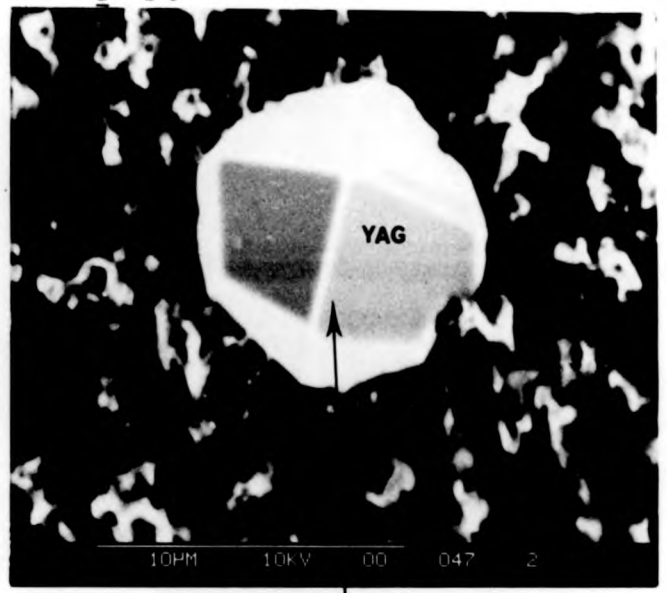

C

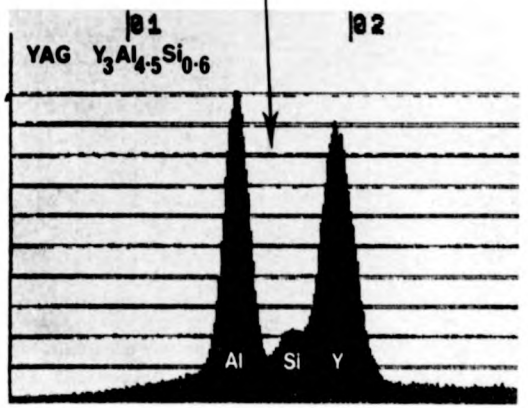

FIGURE 5.3 - YAG formation on actively oxidised Syalon Ceramic surfaces

Micrographs and analysis from the SEM/EDAX system:-

A - Alloy S-11.5, 1400°C/20 hrs. Ar atmosphere

B - Alloy S-0, 1400°C/20 hrs. Ar atmosphere

C - EDAX spectrum from YAG polyhedron

periods. The as-mixed a% Al/(Al + Si) ratios of all of these alloys exceeds a value of 11 (see Table 2.2) and the intergranular glass composition of all except S-11.5 occurs in the relatively aluminium and yttrium rich zone of the eutectic trough in the Y_2O_3-SiO_2-Al_2O_3 ternary diagram, see Figure 4.12. No other phase than $Y_2Si_2O_7$ was detected on the outer surface of the alloys relatively poorer in aluminium although the presence of cristobalite may have been expected[75]. However the formation of O', a silicon rich phase, has been detected[27] in the sub-oxide zone of this type of ceramic after heat-treatment at ~1300°C.

Since, during the oxidation reaction, transport of M^{y+} intergranular ions from the bulk to the surface occurs, the change in composition at the oxide scale surface may be used to monitor the progressive oxidation of Syalon Ceramics with time. Figure 5.4 illustrates the reduction of oxidation rate with increased time at 1200°C under a nitrogen atmosphere (with oxygen impurity) for alloy S-0. Although iron is a common contaminant in these materials it is not found to concentrate in the oxide scale but remains in the inter-β' channels, in combination with silicon, where it is readily identified in the electron microscope.

Polished sections through the ceramic specimens, normal to the oxide surface, were examined under the optical microscope and in the SEM. Below the oxide scale a zone of light contrast, with respect to the bulk material, was observed with the naked eye. This light grey zone was found to grow further into the bulk with increasing oxidation time, as schematically illustrated in Figure 5.5. Analysis of larger matrix pools within the light grey zone suggested a lower yttrium prescence than in the bulk, although more recent work[101] has led to the conclusion that the effect may be due to oxygen penetration down the glassy inter-β' channels, since the yttrium depleted zone does not always stretch completely to the interface between the light grey zone and the bulk.

The surface of alloy S-10.75A and B ceramics after heat-treatment for long periods (~200hrs.) under nitrogen at 1400°C was found to be covered by a thick, white, friable layer and the bulk ceramic was easily fractured due to the apparent removal of the intergranular phase. X-ray microanalysis in both the TEM and SEM defined the mean cation composition of the white layer as ~$Y_{10}Si_{6.8}$, and SAD from grains of the material scattered on a carbon film implied a hexagonal structure with variable lattice parameters:-

FIGURE 5.4 - Mean analysis of alloy S-O oxide surface (SEM/EDAX) after heat treatment at 1200°C under nitrogen atmosphere

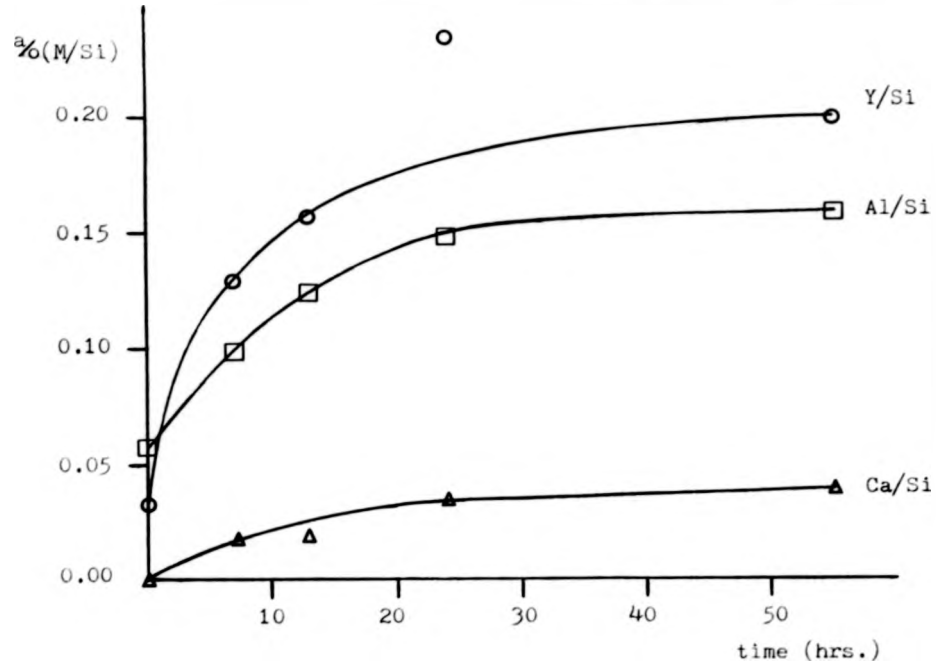

FIGURE 5.5 - Oxidation of intergranular phase (schematic)

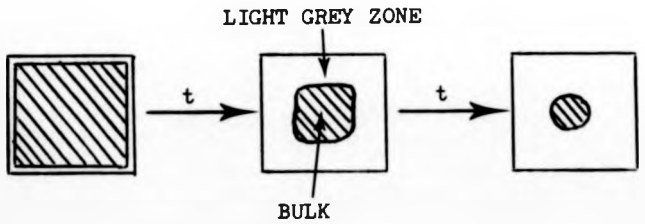

$$a = 9.28 - 9.45 \text{ Å}$$
$$c = 6.72 - 6.84 \text{ Å}$$

This data is identified with the known phase [102] Y-N-Apatite:-

$$Y_{10}(SiO_4)_6N_2 \longleftrightarrow Y_{9.7}(SiO_4)_6ON$$

a = 9.36 Å	a = 9.37 Å
c = 6.77 Å	c = 6.75 Å

of hexagonal structure which is well documented in the literature.

(c) Interaction under Air atmosphere

Under an atmosphere of ambient laboratory air all specimens underwent passive oxidation in the range 1100 - 1500°C as described in the previous section. However, under air, the penetration depth of the light grey oxidised zone was found to be greater, for a given time at a given temperature, when compared with specimens heat-treated under nitrogen.

5.4.2 Heterogeneously nucleated crystallisation

(a) Introduction

'Surface crystallisation' proceeds by the same growth mechanisms as bulk crystallisation, but is initiated more easily via heterogeneous nucleation catalysed at the specimen free surface and its associated flaws. It is essential, for operation of this heterogeneous process that the surface catalysing nucleation be wetted by the newly formed crystal phase in the presence of the mother glass phase. The fact that efficient sintering of β' ceramics is promoted by the presence of an oxynitride melt suggests a high degree of wetting with a low contact angle, producing a low β'/liquid interfacial energy, $\gamma_{\beta' L}$. On cooling this interfacial energy must increase, but in the temperature regime applicable to devitrification of the intergranular phase $\gamma_{\beta'\beta'}$ is likely to exceed $2\gamma_{\beta' L}$ and wetting is maintained [103]. In this temperature regime a crystal /β' interface would produce a relatively high interfacial energy (due to lattice mis-match) and there is an expected resistance to epitaxial nucleation of intergranular crystallinity on β' surfaces in this respect. Thus it is unlikely that the β' presence would promote heterogeneous nucleation, despite its large surface area, but the existence of porosity and any crystals of similar Bragg spacing, d_{hkl}, to the crystallising phase are expected to lead to heterogeneous nucleation.

Cubic specimens, of side 3mm, of various Syalon Ceramic alloys were subjected to 5hr. heat-treatments in the temperature interval 1100 - 1500°C, with 50°C increments, under a nitrogen atmosphere. Some heat-treatments were also performed in air.

After heat-treatment the cubic specimens were cut open and polished to a 1μm diamond paste finish. Examination of the specimens under the optical microscope and in the electron microscopes, utilising EDAX, led to the results expressed in Figure 5.6, in which two crystallisation regimes are represented:-

Crystal growth regime I - occuring at lower temperatures (> 1150°C) in which all nucleation is catalysed at the specimen free surface.

Crystal growth regime II- occuring at higher temperatures (> 1400°C) in which nucleation is catalysed at both the specimen free surface and simultaneously in the bulk.

In this one-step type of heat-treatment, not including an isothermal nucleation dwell, bulk nucleation densities are very low and the dominant mode is probably heterogeneous, catalysed by porosity and other flaws, rather than homogeneous.

Most quantitative data was collected from alloys S-0, S-10.75A and S-10.75B since they were available in larger volumes than other alloys. The behaviour of these alloys, provided in half-billet form, may be taken to indicate the trends expected upon addition of nitrogen to the intergranular glass and qualitative data taken from other alloys confirm these trends.

(b) Glass crystallisation in alloy S-0

In the temperature range 1200 - 1400°C, after heat-treatment for 5 hrs, the crystallisation behaviour of alloy S-0 matrix glass was found to be described by growth from heterogeneous surface nucleation. However, subsequent experiments proved that some bulk crystallisation does occur on heat-treatment in the range 1150 - 1300°C for longer times, although surface crystallisation is always the dominant mode.

Specimens annealed at temperatures below ~1100°C did not exhibit any intergranular crystallisation during heat-treatment for times up to 100 hrs.

Consideration of the ternary oxide diagram and results of microanalysis indicate a liquidus temperature, T_L, for S-0 matrix

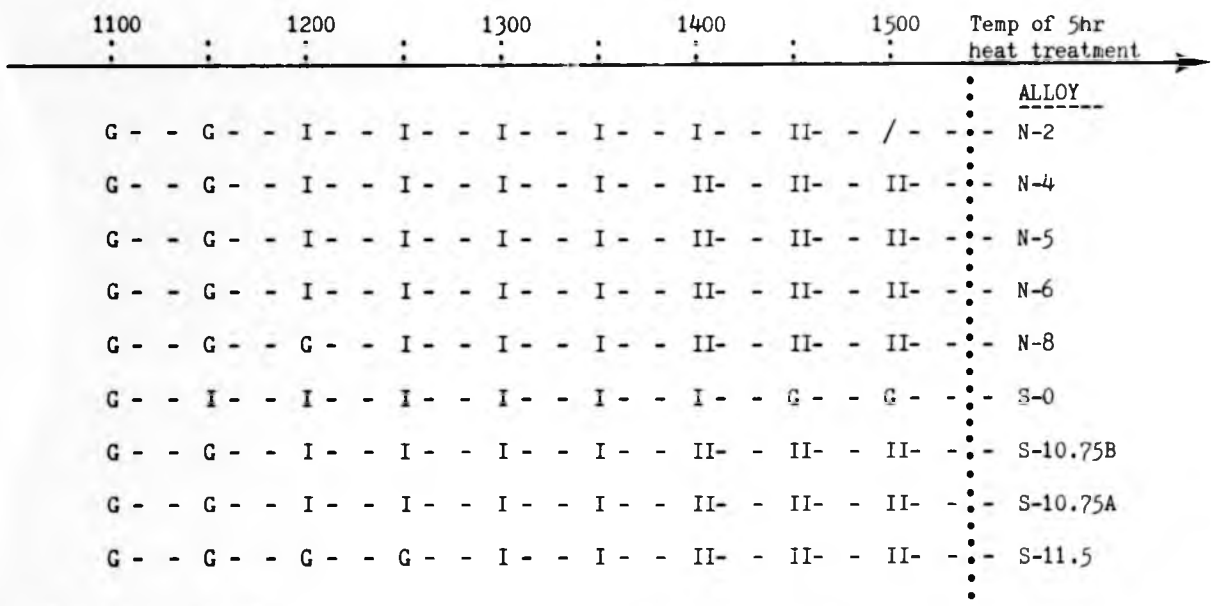

State of intergranular phase after heat treatment; G = Glass only
I = Growth regime I, surface nucleation
II = Growth regime II, nucleation in bulk and at surface

FIGURE 5.6 - Heterogeneous nucleation during 5hr heat treatment under N_2 atmosphere

glass at ~1485°C, see Figure 5.7, but no crystallisation was detected in specimens heat-treated at 1450°C for times up to 10 hrs, possibly indicating that a lower T_L is applicable.

FIGURE 5.7 - Section through the ternary oxide phase diagram

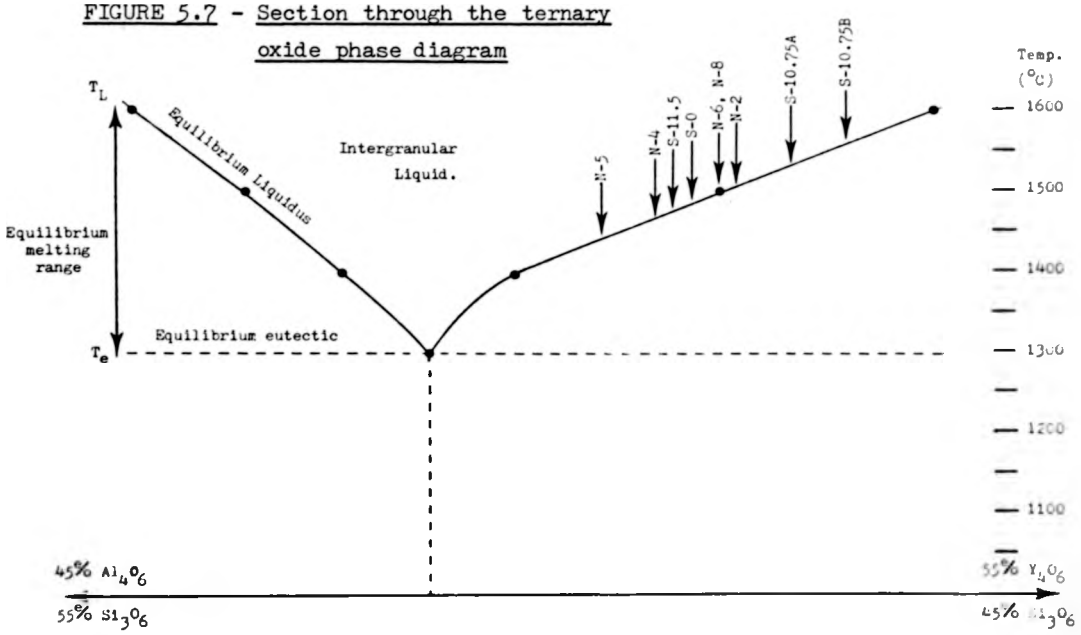

To assess the growth rate of the observed crystallisation effect, single dwell heat-treatments were performed in air at various temperatures for various times. Using a travelling microscope, the distance between the specimen surface and growth front was determined from optical micrographs, and the results are presented in Figure 5.8 in which each point represents the mean of measurements from the four surfaces and their parallel crystallisation fronts, cross—sectioned in each specimen. Measurements after short heat-treatment times were not made due to confusion in identification between the light grey oxidised zone and the crystallisation front. The kinetics of crystallisation are discussed in Section 5.5.2 with reference to the oxidation effect. For comparison a tentative line is drawn for heat-treatment at 1200°C in nitrogen and it is noted that the growth rate is higher than that for similar treatment in air.

FIGURE 5.8 - Kinetics of the surface crystallisation effect observed in alloy S-0

A Crystal growth rates

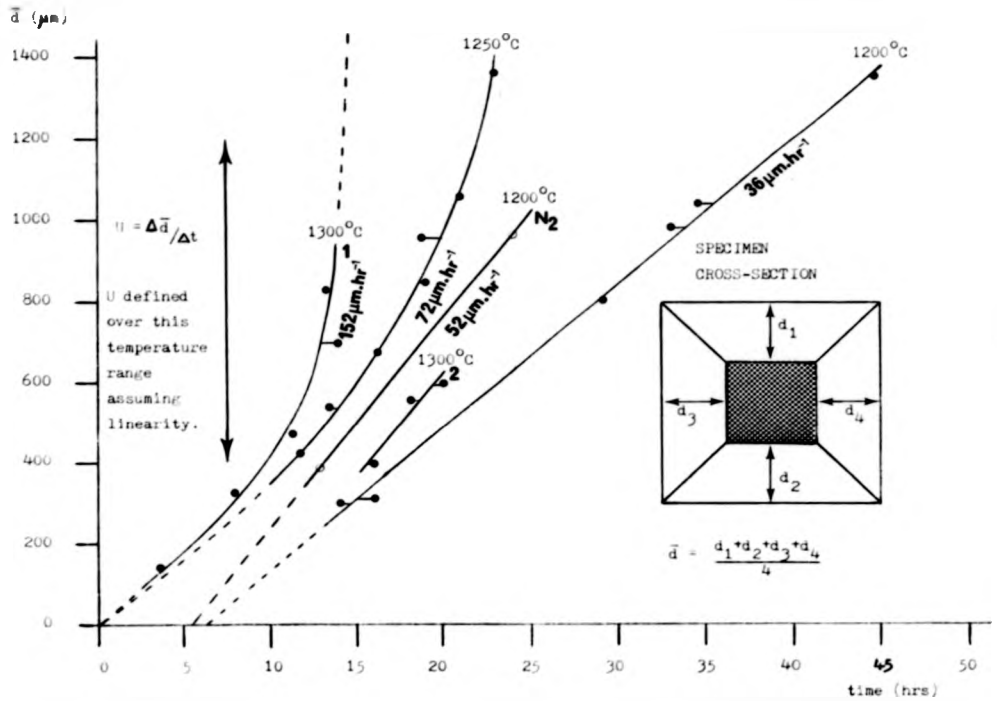

B Optical micrograph of alloy S-0 section after 1250°C/16hrs. heat-treatment in air

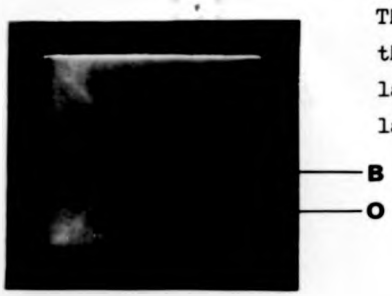

The crystallisation front has progressed through the light grey oxidised zone, labelled O, into the bulk material, labelled B.

FIGURE 5.8 - Kinetics of the surface crystallisation effect observed in alloy S-0

A Crystal growth rates

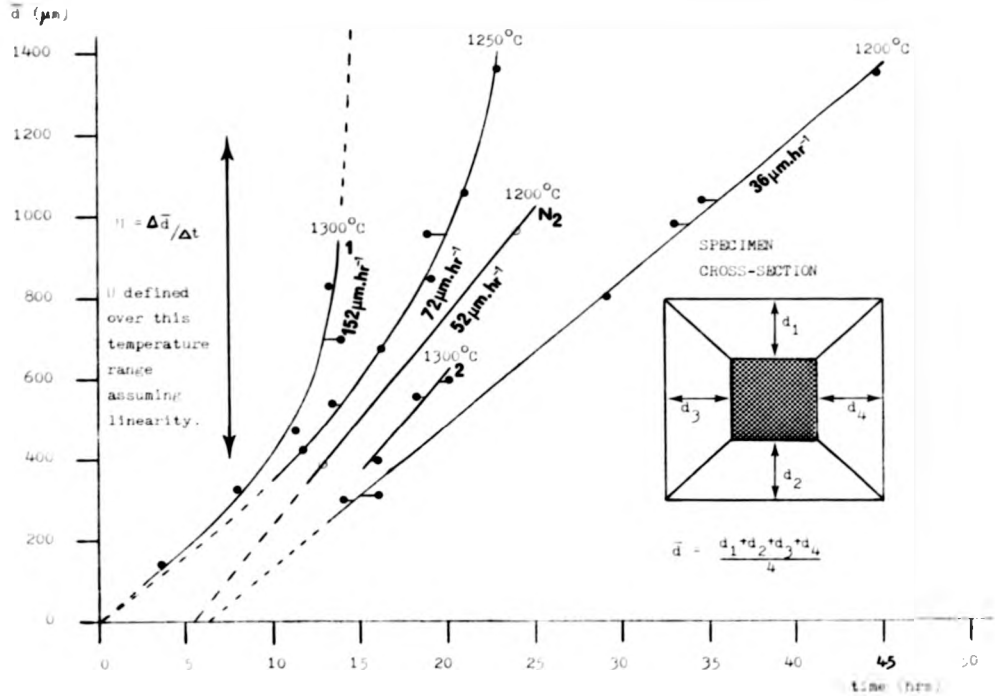

B Optical micrograph of alloy S-0 section after 1250°C/16hrs. heat-treatment in air

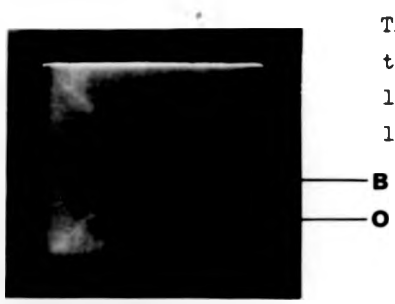

The crystallisation front has progressed through the light grey oxidised zone, labelled O, into the bulk material, labelled B.

In the SEM, microanalysis data was collected from many of the larger matrix pools, present in cross-sections of S-0 specimens, after various heat-treatments under a nitrogen atmosphere. The results, presented in Figure 5.9A, indicate that the volume ratio of $Y_3Al_5O_{12}/Y_2Si_2O_7$ increases with temperature in the range 1200 - 1400°C, although above 1300°C formation of YAG is demoted to longer heat-treatment times. XRD spectra taken from the crystallised sub-surface layers of alloy S-0 were found to differ from those, characteristic of β-$Y_2Si_2O_7$, obtained from the outer oxide scale. The sub-surface crystalline phase was identified as α-$Y_2Si_2O_7$ and similar spectra were recorded after crystallisation at higher temperatures, but with a larger contribution from YAG, as suggested by data from EDAX in the SEM.

The crystalline phase content identified in specimens of alloy S-0 is defined on a Temperature-Time map in Figure 5.10a and proposed Temperature-Time-Transformation curves are sketched around the data for detection of $Y_2Si_2O_7$ and $Y_3Al_5O_{12}$, in the SEM, by EDAX. Confirmation of crystal species identity was provided by XRD analysis taken from selected specimens. The equilibrium state liquidus, $T_L \approx 1485$°C, was derived from Figure 5.7, using data from TEM/EDAX analysis, and the predominant crystallisation mode is noted as surface nucleated. The shortest heat-treatment duration was 2 hrs. (1300°C) and only sub-surface β-$Y_2Si_2O_7$, associated with the oxidation effect, was observed in this specimen.

The growth front effect, described in Figure 5.8, was found to correspond to a line of intergranular interconnected porosity, when studied in the SEM, and to further elucidate its nature a thin section was prepared for observation and analysis in the TEM, see Figure 5.11. The porous nature of the front effect is demonstrated, the true crystallisation front moving through matrix glass a few β' grain widths behind.

Measurement of the β'_{ss} composition indicated no significant change from that of the as-sintered material, even after lengthy heat-treatment, thus it seems that the large residual glass volume in this alloy accomodates all ions rejected at the crystal growth fronts during heat-treatment.

Figure 5.9 - (Opposite) The relative fractions of crystalline phases present in Syalon Ceramics (SEM/EDAX)

The data obtained from alloys S-0 and S-10.75 both indicate an increase in the content of yttrogarnet relative to yttrium disilicate, with increasing heat-treatment temperature, as observed using SEM/EDAX techniques.

For alloy S-0 it is evident that increasing heat-treatment time leads to an enhancement of the yttrogarnet volume fraction.

FIGURE 5.9 - The relative fractions of crystalline phases present in Syalon Ceramics (SEM/EDAX)

Alloy	S-0	S-10.75B	S-10.75A
%N EDAX/EELS	0	7.42	12.38

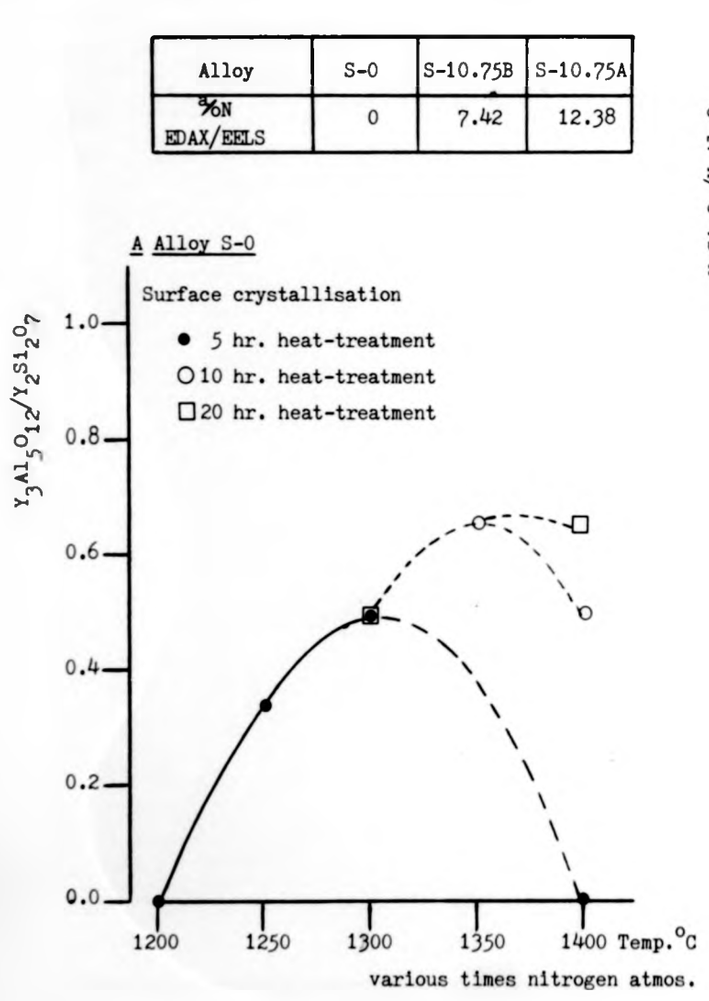

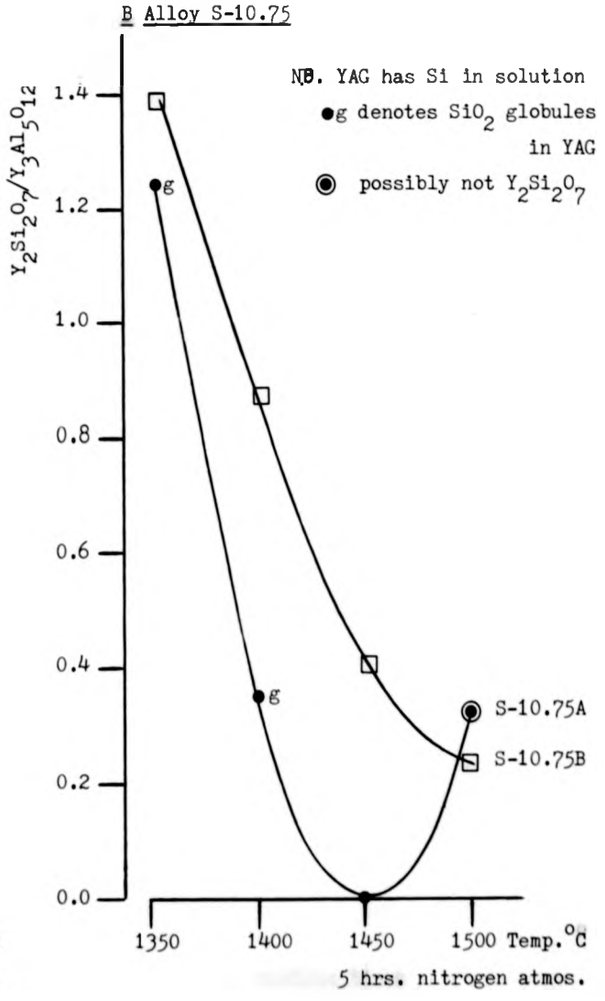

FIGURE 5.10 - **Proposed T-T-T curves**

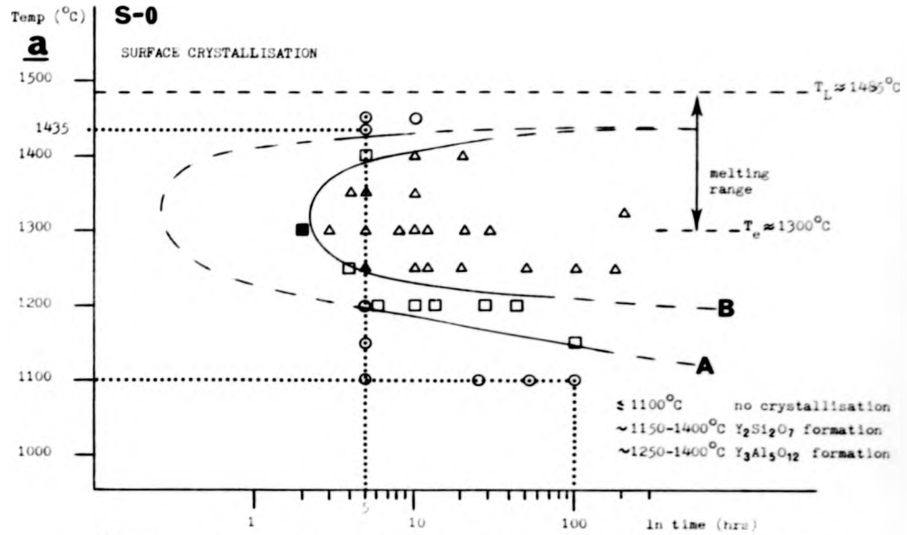

Curve **A** represents the necessary time for formation of an observable $Y_2Si_2O_7$ content (SEM/EDAX).

Curve **B** represents the necessary time for formation of an observable $Y_3Al_5O_{12}$ content (SEM/EDAX).

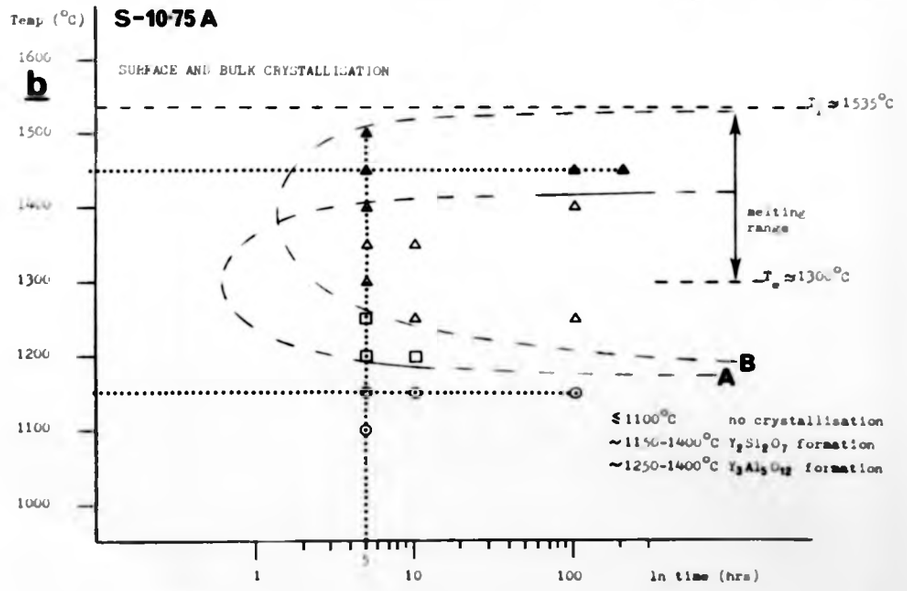

key:

- ○ Glass
- □ α-$Y_2Si_2O_7$* Glass
- ■ β-$Y_2Si_2O_7$* Glass
- △ α-$Y_2Si_2O_7$* $Y_3Al_5O_{12}$* Glass
- ▲ $Y_3Al_5O_{12}$* Glass

Observations from SEM/EDAX and XRD analysis.

FIGURE 5.11 (opposite)

a - Rectangular specimen of alloy S-0 (~10x3x3 mm^3) after heat-treatment in air at 1250°C, and the thin slice removed from it for preparation of a TEM specimen. Schematic.

b - Optical micrograph (transmitted and dark field reflected light mode) of the prepared TEM specimen. The two parallel porous crystallisation fronts are seen in light contrast at the edge of the ion thinned hole.

c - Low magnification electron micrograph of the specimen. The porous region A corresponding to the crystallisation front is considered in d. Less porous regions were found to be composed from β'/YAG/glass, and some formation of both YAG and $Y_2Si_2O_7$ was observed in the bulk of the specimen ahead of both growth fronts.

d - High magnification electron micrograph of area A. The growth front is seen to be a line of interconnected porosity, p, at β' boundaries, from which the intergranular phase has apparently drained. A meniscus may be seen at the corners of some porous β' triple grain junctions. The matrix volume immediately behind the porous front is predominantly glassy with crystalline matrix phases a few β' grain widths further back, at the true crystallisation front. Many porous regions remain in the crystalline microstructure when the porous front has propagated further into the bulk material.

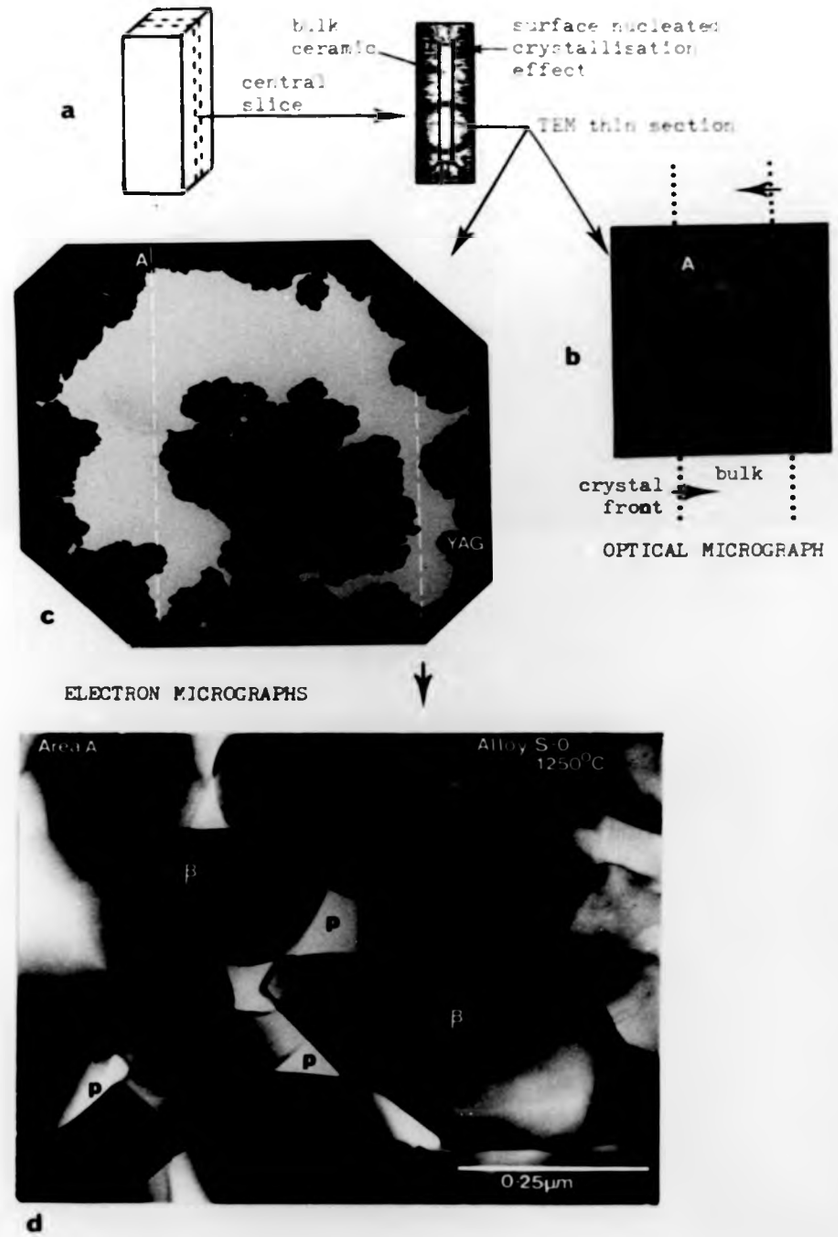

Section through the growth front of alloy S-0

FIGURE 5.11 (opposite)

a - Rectangular specimen of alloy S-0 (~10x3x3 mm^3) after heat-treatment in air at 1250°C, and the thin slice removed from it for preparation of a TEM specimen. Schematic.

b - Optical micrograph (transmitted and dark field reflected light mode) of the prepared TEM specimen. The two parallel porous crystallisation fronts are seen in light contrast at the edge of the ion thinned hole.

c - Low magnification electron micrograph of the specimen. The porous region A corresponding to the crystallisation front is considered in d. Less porous regions were found to be composed from β'/YAG/glass, and some formation of both YAG and $Y_2Si_2O_7$ was observed in the bulk of the specimen ahead of both growth fronts.

d - High magnification electron micrograph of area A. The growth front is seen to be a line of interconnected porosity, p, at β' boundaries, from which the intergranular phase has apparently drained. A meniscus may be seen at the corners of some porous β' triple grain junctions. The matrix volume immediately behind the porous front is predominantly glassy with crystalline matrix phases a few β' grain widths further back, at the true crystallisation front. Many porous regions remain in the crystalline microstructure when the porous front has propagated further into the bulk material.

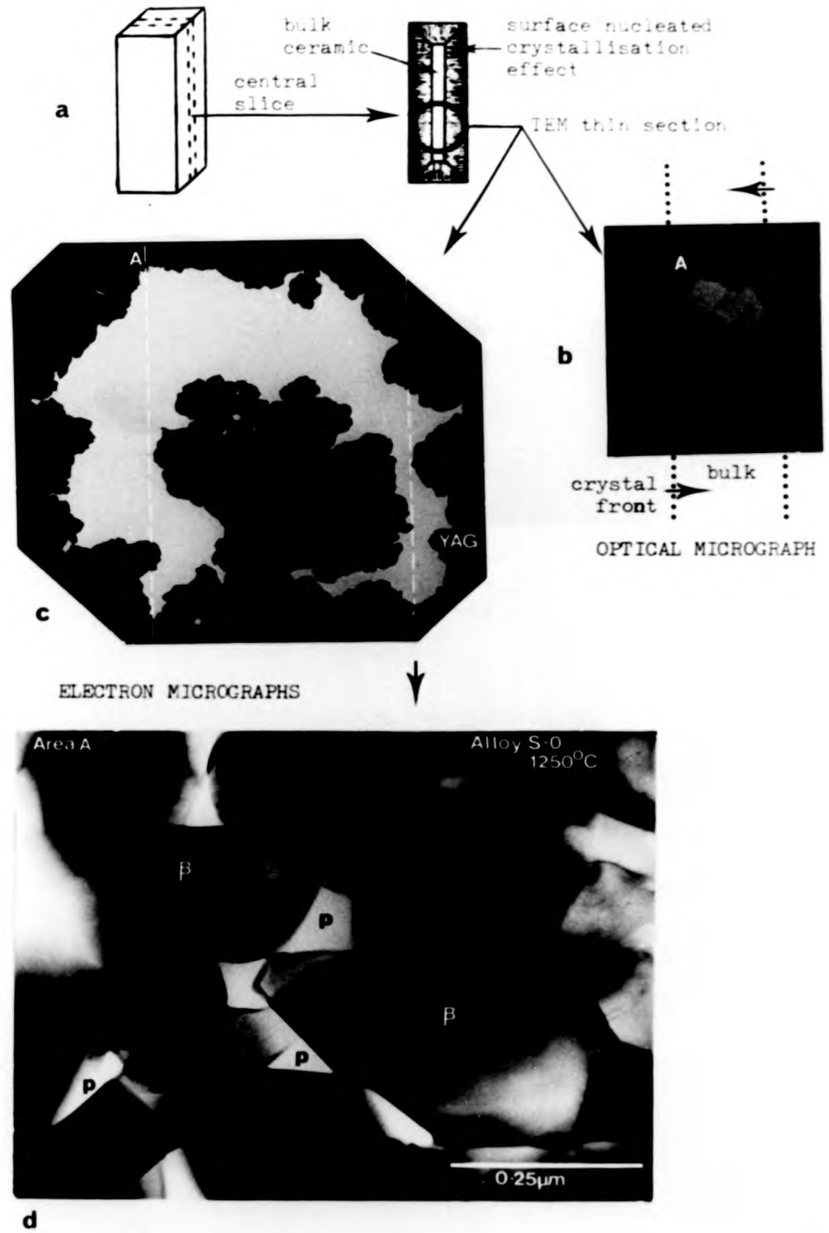

Section through the growth front of alloy S-0

(c) Intergranular devitrification in ceramic S-10.75A and other alloys with polytypoid addition

Five hour heat-treatment in the temperature range 1200 - 1350°C promoted surface crystallisation in alloy S-10.75A, similar in appearance to that found in alloy S-0. At higher temperatures, however, crystallisation of YAG, as the major phase, occurred in the bulk of the specimen. The tendency towards an increase in the volume ratio $Y_3Al_5O_{12}/Y_2Si_2O_7$ with increasing temperature is demonstrated in Figure 5.9B. It is evident that, for a given heat-treatment temperature, the predominance for YAG formation increases, with nitrogen content, along the alloy series S-0, S-10.75B, S-10.75A.

A tentative T-T-T diagram was constructed for the matrix glass of S-10.75A and is presented, as Figure 5.10b, for comparison with data from S-0 in Figure 5.10a.

The investigation of crystallisation behaviour in other alloys, of intermediate 21R addition, in various states of heat-treatment, prompted the general conclusion that addition of nitrogen to the matrix glass tends to shift the the devitrification regime to higher temperatures promoting YAG formation and decreasing the amount of $Y_2Si_2O_7$ produced.

5.4.3 The promotion of bulk nucleated crystallisation

Derivation of finer crystal size by increasing nucleation density is widely recognised as a route to improved properties, due to a decrease in stress and porosity levels, in the microstructure of glass ceramics[58]. This effect is most often achieved by exercise of a dual dwell approach to heat-treatment, in which the first temperature level is chosen to coincide with the maximum rate of nucleation, T_I, and the second level coincides with a controlled rate of crystal growth, $\approx T_U$.

Dual dwell heat-treatment of selected Syalon Ceramic alloys was performed under a nitrogen atmosphere, see Table 5.4, and qualitative assessment of matrix character was deduced during examination in the SEM and from optical microscopy. Some of the heat-treated alloys with finer crystal size were also examined in the TEM to assess the degree of crystallisation into the smaller inter-channels.

For all alloys other than S-0, N-2 and S-11.5 the heat-

treatment 1200°C/5 hrs. - 1400°C/5 hrs. produced the best microstructure in terms of degree of crystallisation, homogeneity, porosity levels and YAG crystal size. However, it is expected that further improvements could be made to individual alloys by refining the size of the temperature steps between dwell levels. Even with the dual dwell heat-treatments described, the YAG crystal size, observed by diffraction contrast in the TEM, stretched over many β' grain widths and it is believed that nucleation still occurs heterogeneously, at the presence of microporosity or other flaws.

TABLE 5.4 - Dual dwell heat-treatment of Syalon Ceramics

Temperature $Level_I$ = nucleating step

Temperature $Level_U$ = crystal growth step

$Level_I$ °C/ 5hr. Dwell	1100	1200	1300	1100	1200
$Level_U$ °C/ 5hr. Dwell	1400	1400	1400	1300	1300

The 'dark spots' associated with large YAG crystal growth and porosity were not present in most alloys after inserting a nucleation step, 1200°C/5 hrs, into the heat-treatment schedule, 1400°C/5 hrs, which previously gave rise to these large flaws. The removal of these defects from the material is expected to lead to enhanced corrosion and wear resistance, important properties in the application of these ceramics. Crystallisation of these alloys appeared almost complete, with only occasional glassy matrix volumes located at the corners of three grain junctions.

Alloy U-8 (not previously discussed in this thesis), prepared with Union Carbide source Si_3N_4 powder, was found to undergo bulk spherulitic type growth upon heat-treatment at 1400°C/5 hrs, see Figure 5.12. A dual dwell heat-treatment, performed at Lucas-Cookson Syalon Ltd, was found to remove the large scale inhomogeneity and finer crystallisation of YAG resulted.

Alloys S-0 and N-2 exhibited a large degree of residual glassy volume, even after the dual heat-treatments described, and the tendency to form large volumes of $Y_2Si_2O_7$ remained.

Alloy S-11.5 retained the 'dark spots' on dual heat-treatment, but it is believed that a further increase in the second (crystal growth) dwell temperature would remove these features.

Compositional analysis of the β'_{ss} indicated fluctuations in the alumina substitution level, z, after various heat-treatments.

FIGURE 5.12 - Coarse crystallisation effect in alloy U-8 after heat-treatment 1400°C/5 hrs.

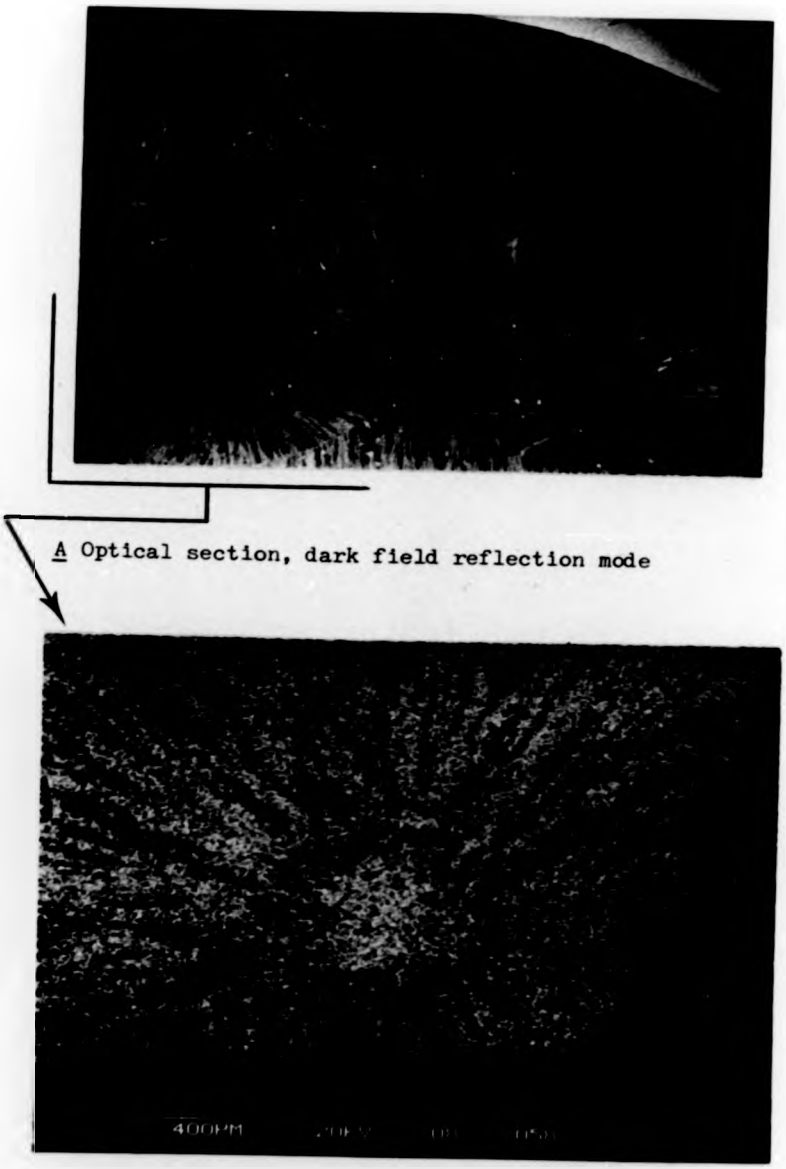

A Optical section, dark field reflection mode

B Backscattered electron mode in the SEM

FIGURE 5.12 - Coarse crystallisation effect in alloy U-8 after heat-treatment 1400°C/5 hrs.

A Optical section, dark field reflection mode

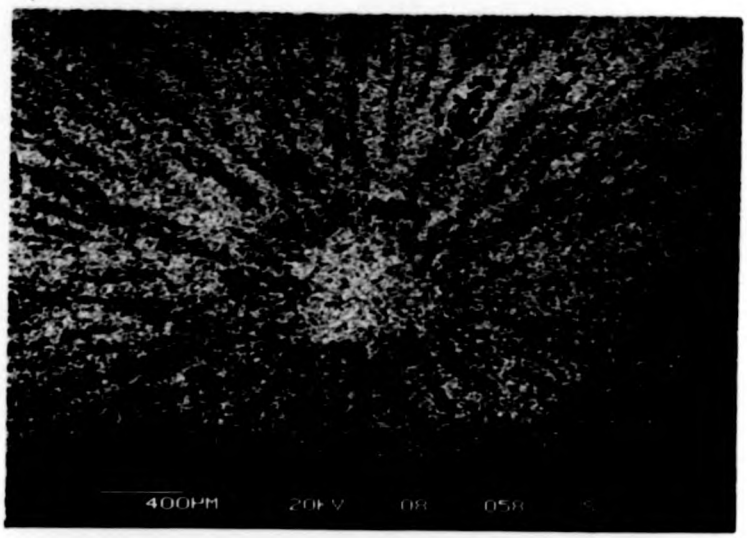

B Backscattered electron mode in the SEM

eg. for N-8 as-sintered $\bar{z}$ = 0.539 ± 0.012, but after the heat-treatment 1200°C/5 hrs. - 1400°C/5 hrs the value $\bar{z}$ = 0.564 ± 0.022 was obtained. Due to the dwell at 1200°C this material contained large amounts of $Y_2Si_2O_7$ and analysis of a β' grain adjacent to a large $Y_2Si_2O_7$ crystal gave $\bar{z}$ = 0.948, whereas a β' grain adjacent to a large YAG crystal gave the analysis $\bar{z}$ = 0.273. Such compositional variation amongst β' grains close to large matrix crystals was found to be a common effect and demonstrates the power of this phase in absorbing excess Si^{4+}, Al^{3+}, O^{2-} and N^{3-} ions from the surrounding matrix during heat-treatment.

5.5 Discussion - The effect of intergranular glass composition and heat-treatment temperature upon the devitrification behaviour of Syalon Ceramics

5.5.1 Crystallisation in the bulk

(a) The effect of glass composition on devitrification

The most important compositional parameter affecting the crystallisation behaviour of the various intergranular glasses investigated appears to be the nitrogen/oxygen content. This result is to be expected, since, (as shown in Chapter 4) during the sintering of an alloy with 21R addition, excess Al^{3+} ions are removed from the liquid component and concentrated in the β'_{ss}, which is well below its Al_2O_3 saturation limit in all the ceramics studied. This results in the formation of intergranular glasses, in ceramics of different as mixed composition, which are very consistent in terms of metal ion composition, all being close to the eutectic trough in projection onto the ternary oxide face of the Janecke prism. The major compositional difference between the intergranular glasses in a 21R addition series is, therefore, the nitrogen/oxygen ratio, which increases with 21R addition, but not in a linear fashion due to increased nitrogen loss or α' formation at high concentrations.

A change in glass nitrogen content is seen to influence the major product of devitrification, increased nitrogen levels favouring the formation of $Y_3Al_5O_{12}$ over the formation of $Y_2Si_2O_7$. It is suggested that the tendency to increased viscosity (demonstrated by the glass structural parameter Y'), upon addition of nitrogen to a glass, suppresses $Y_2Si_2O_7$ by decreasing the crystal growth rate (Ux B. $\Delta T/\eta$) the formation of YAG being promoted at higher temperatures.

(b) The effect of temperature on devitrification

Increasing the heat-treatment temperature is seen to favour the formation of YAG, over $Y_2Si_2O_7$, as the major product of crystallisation from the intergranular glasses. The highly isotropic (cubic) structure of YAG results in growth through the inter-β' glassy channels with a characteristic rounded glass/crystal interface. Yttrium disilicate, however, grows in a more faceted form and thus these two phases are easily distinguished in the TEM, even without application of EDAX, see Figure 5.13. In the SEM the two phases may be distinguished simply by observation in the backscattered mode, since the mean atomic number of yttrium disilicate is higher than that of YAG and it appears brighter in contrast against the dark β' background.

In highly viscous glass, supercooled 5 - 100°C, the occurrence of spherulitic growth, characterised by low nucleation density and slow growth rates, is a well documented phenomenon[58],[104],[105]. This type of growth accounts for the dark spots observed in alloys richer in 21R when heat-treated at 1400°C. Since, with experience,distinction between YAG, yttrium disilicate and glass is easily made in the SEM, without recourse to microanalysis, it is possible to map the YAG rich spherulites at low magnification, see Figure 5.14. Increasing heat-treatment temperature,to a level above the zone of supercooling, is expected to remove this effect from alloy S-11.5, since the then reduced viscosity would not support slow spherulitic growth mechanisms.

A micrograph demonstrating the growth of YAG through the intergranular glass of alloy N-12, after 1300°C/5 hr. heat-treatment is provided as Figure 5.15. Use of lower electron accelerating voltage enables higher resolution than seen in Figure 5.14 and the areas of YAG are clearly seen with residual (darker) glass between them. Increase of time or temperature leads to larger volumes of YAG crystallisation in this alloy.

5.5.2 Crystallisation nucleated at the specimen free surface

As well as catalysing heterogeneous nucleation, the specimen free surface leads to radical changes in the chemistry of the bulk intergranular phase, due to interaction with the atmosphere. It is the oxidation effect which causes the apparent acceleration of crystallisation with time in alloy S-0, see Figure 5.8. Initial loss of Y^{3+} ions, from the intergranular glass to the oxide scale surface,

FIGURE 5.13 - Comparison of morphology and analysis of YAG and Yttrium Disilicate as studied in the TEM

A - Micrograph showing growth of YAG through the intergranular glass of alloy S-10.75A after heat-treatment at 1350°C/5 hrs. Some phase separation in the form of SiO_2 globules is visible. A glass pool is present in one of the β' grains.

B - Microanalysis from the YAG phase.

C - Micrograph showing faceted morphology of $Y_2Si_2O_7$ crystal growing in glass of alloy S-0 on heat-treatment at 1200°C/ 5 hrs.

D - Microanalysis from $Y_2Si_2O_7$ phase.

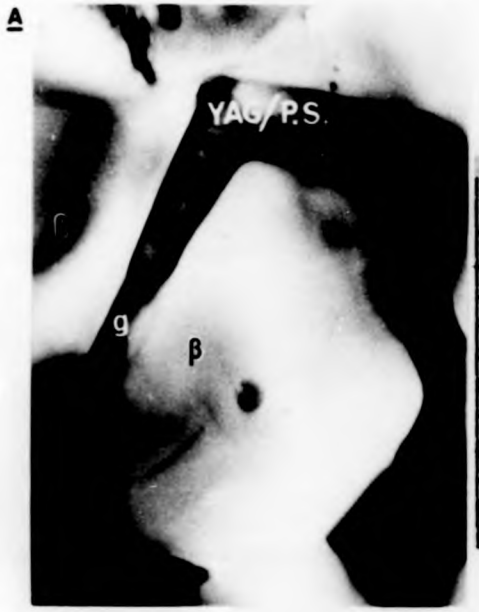

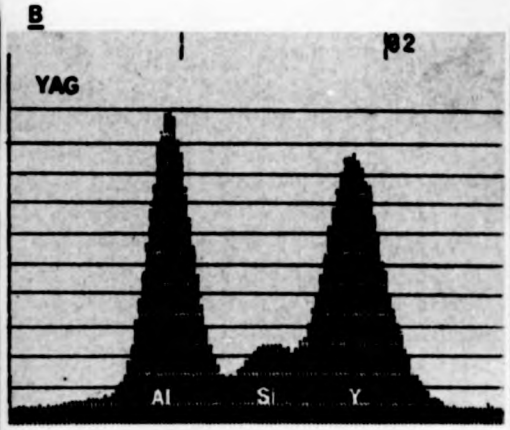

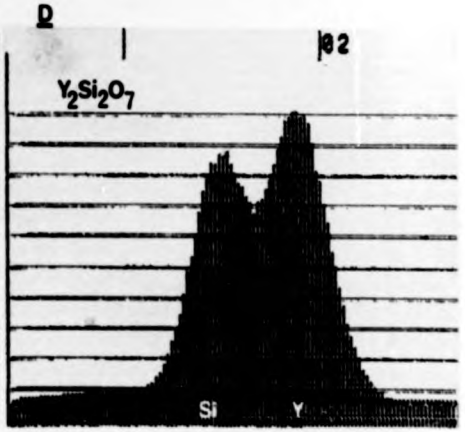

FIGURE 5.13 - Comparison of morphology and analysis of YAG and Yttrium Disilicate as studied in the TEM

A - Micrograph showing growth of YAG through the intergranular glass of alloy S-10.75A after heat-treatment at 1350°C/5 hrs. Some phase separation in the form of SiO_2 globules is visible. A glass pool is present in one of the β' grains.

B - Microanalysis from the YAG phase.

C - Micrograph showing faceted morphology of $Y_2Si_2O_7$ crystal growing in glass of alloy S-0 on heat-treatment at 1200°C/ 5 hrs.

D - Microanalysis from $Y_2Si_2O_7$ phase.

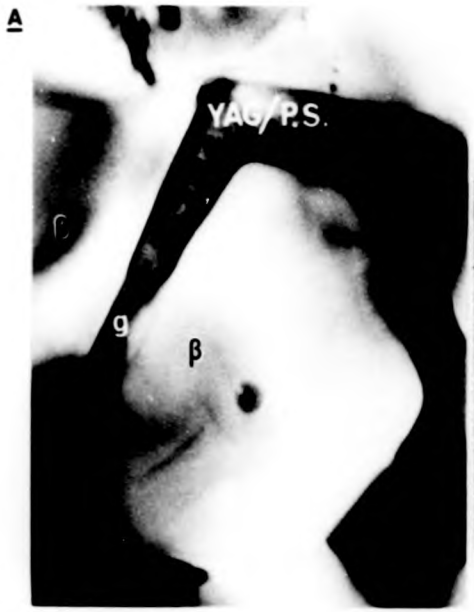

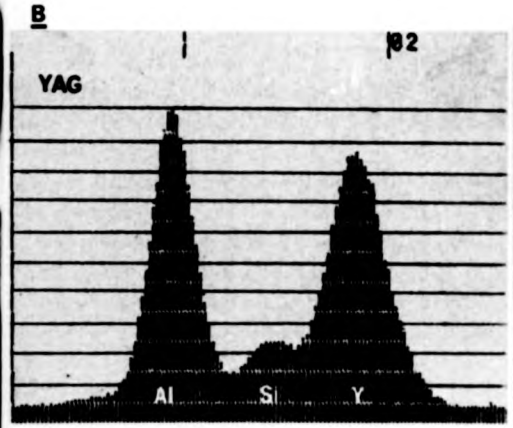

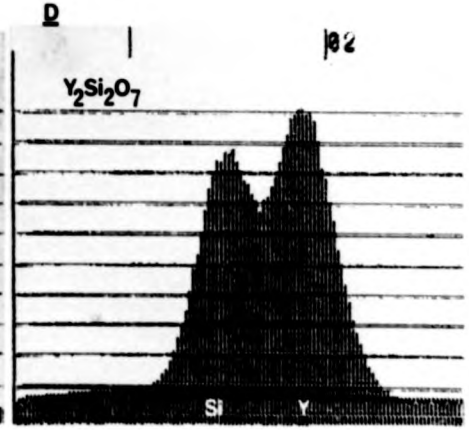

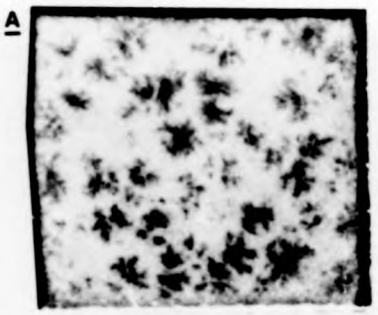

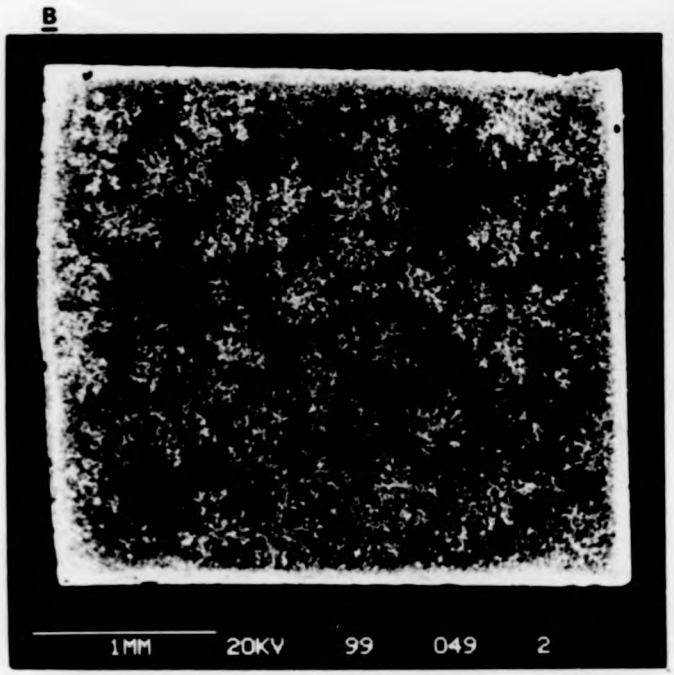

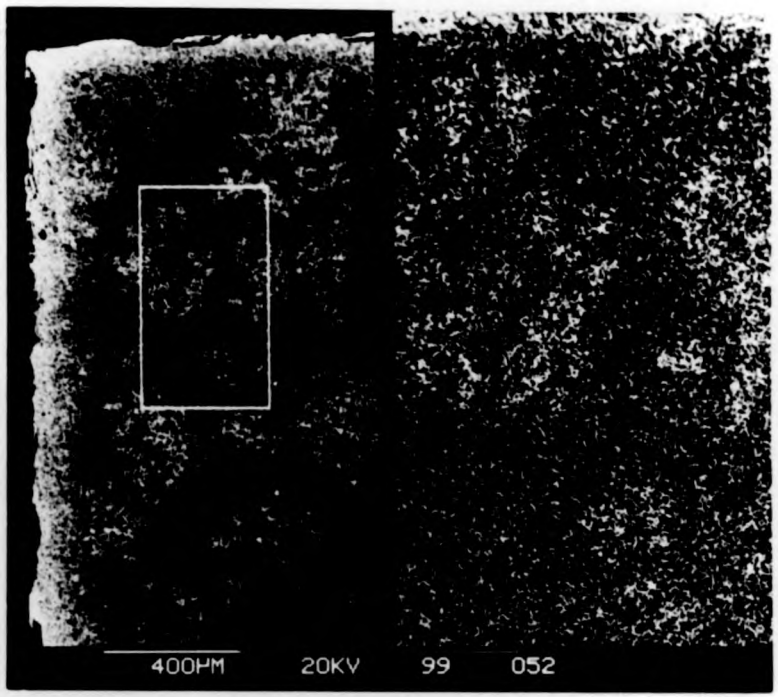

FIGURE 5.14 - Alloy S-11.5 cross-section after heat-treatment 1400°C/5 hrs.

A - Optical section showing coarse crystal regions.

B - SEM section, backscattered electron mode.

C - SEM section, backscattered electron mode.

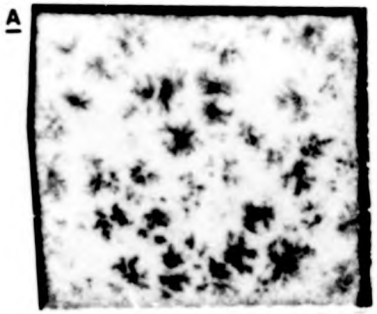

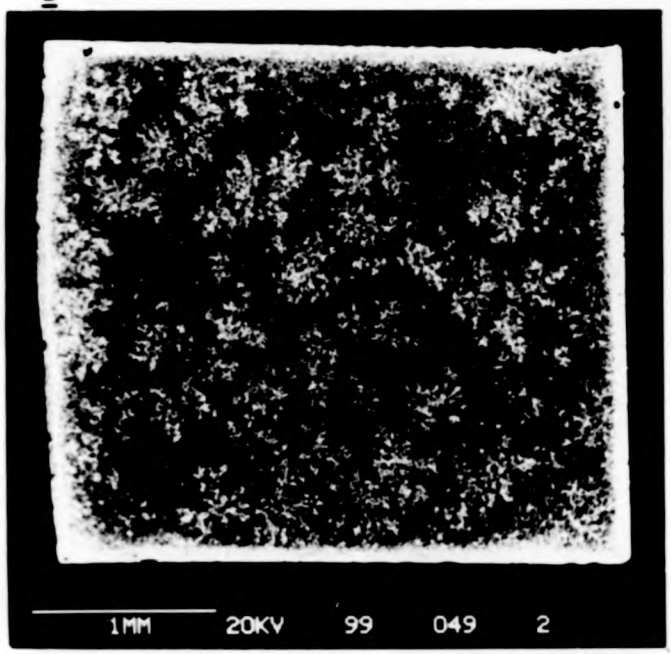

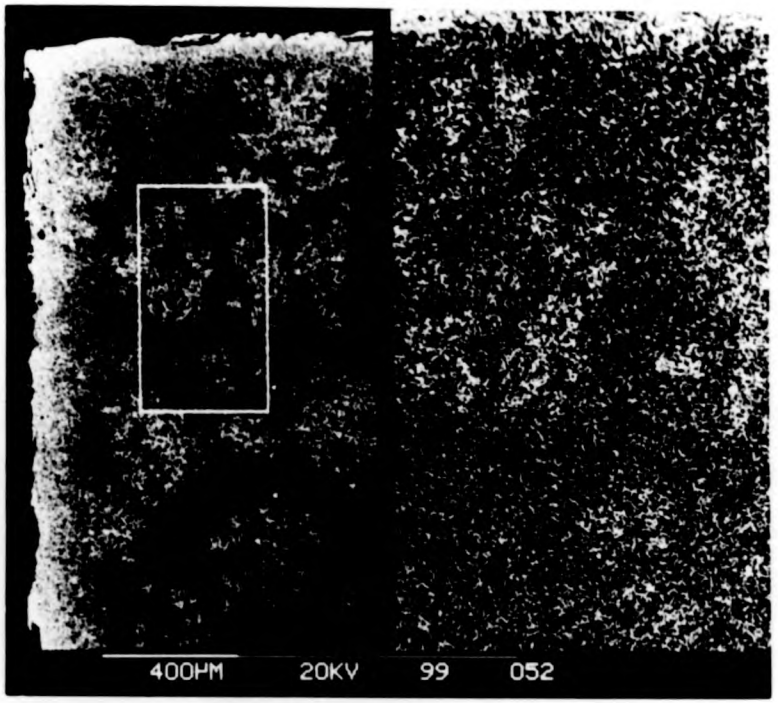

FIGURE 5.14 - Alloy S-11.5 cross-section after heat-treatment 1400°C/5 hrs.

A - Optical section showing coarse crystal regions.

B - SEM section, backscattered electron mode.

C - SEM section, backscattered electron mode.

FIGURE 5.15 - Backscattered electron micrograph of alloy N-12 heat-treated 1300°C/5 hrs.

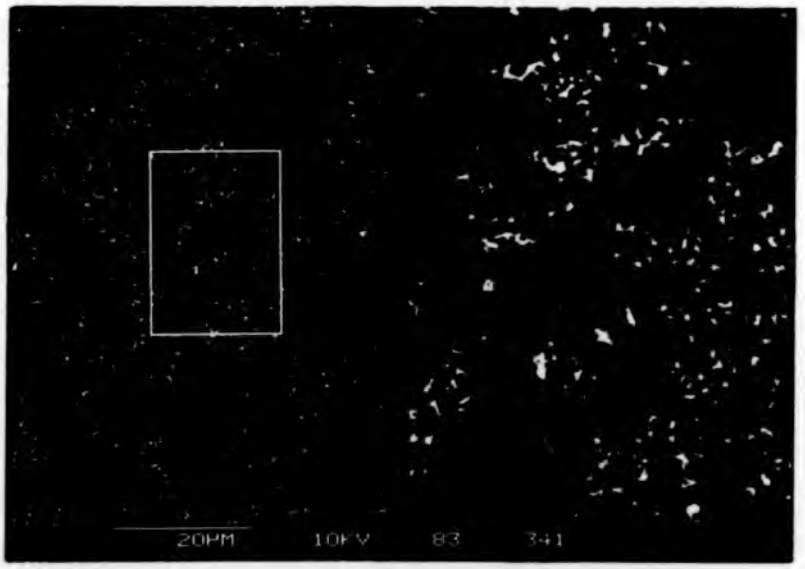

FIGURE 5.15 - Backscattered electron micrograph of alloy N-12 heat-treated 1300°C/5 hrs.

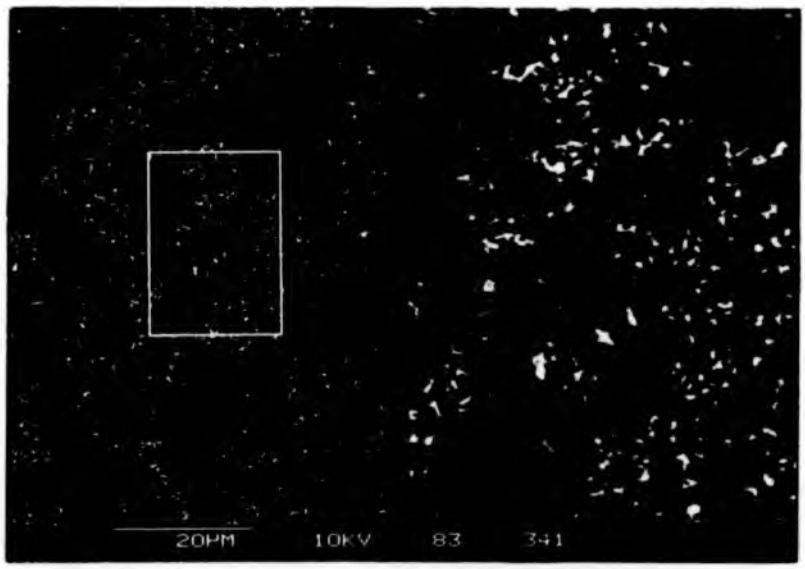

increases glass viscosity and degree of undercooling, which results in decreased $Y_2Si_2O_7$ growth rates. The crystal growth front then moves through a gradient of Y^{3+} concentration accelerating as it grows towards the bulk:-

At 1200°C this effect appears to be overcome after ~15 - 16 hrs. heat-treatment in air and a linear growth rate is observed at longer times, the crystal growth front passing through the light grey oxidation zone into the bulk of constant composition.

At 1250°C the crystal growth front is also seen to overtake the oxidation effect after ~16 hrs. heat-treatment and linear kinetics could be taken from the crystal growth curve after this time.

At 1300°C there is a large amount of instability at the growth front, some parts breaking ahead of the oxidised zone and other parts remaining behind the oxidation reaction front. This leads to confusion in measurement and the apparent observation of two growth fronts.

The difference in kinetics observed for heat-treatment under air and nitrogen atmospheres is explained in terms of small differences in furnace calibration. The furnace was calibrated under an atmosphere of ambient laboratory air and it is possible that it operates at higher temperatures when sealed and operated with a bottled gas atmosphere, since convection losses will not occur in this mode.

Microanalysis of matrix pools behind the porous front showed the presence of $Y_2Si_2O_7$, residual glass and some YAG. It appears, therefore, that the macro-composition behind and ahead of the front is the same and that a cellular type of growth mechanism describes the effect. The expression $U = B.\Delta T/\eta$, where B is a constant, arises by substitution of the Stokes-Einstein relation into the equation for crystal growth rate, U, see Figure 3.4, and this expression has been found to hold for a number of glass compositions[58],[59]. Thus, tentative evaluation of U from Figure 5.8, assuming linear kinetics over the range $1200\mu m > \bar{d} > 400\mu m$ and using a least squares fit to derive U, allows derivation of B/η as seen in Figure 5.16. In considering the process of viscous flow, standard treatment[106] yields the relation:-

$$\eta = \frac{\tau . \exp(\Delta E/kT)}{2\nu_o . \sinh(\tau V_o/2kT)}$$

where, τ = applied shear stress

E = activation energy in absence of stress

ν_o = the number of times per second the barrier is attempted

V_o = the flow volume

FIGURE - 5.16

Derivation of activation energy for crystal growth, assuming a relationship with viscosity, for alloy S-C.

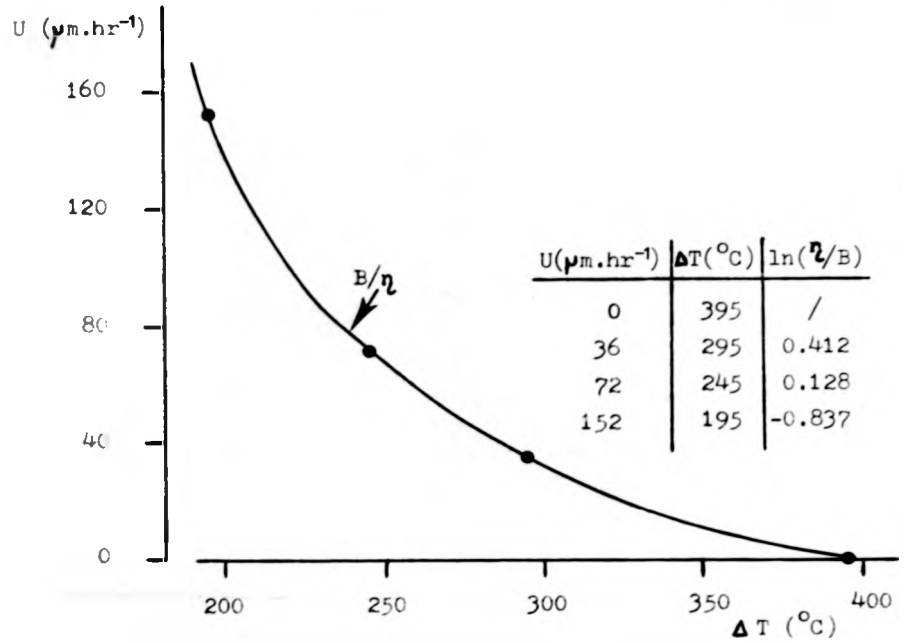

U(μm.hr⁻¹)	ΔT(°C)	ln(η/B)
0	395	/
36	295	0.412
72	245	0.128
152	195	-0.837

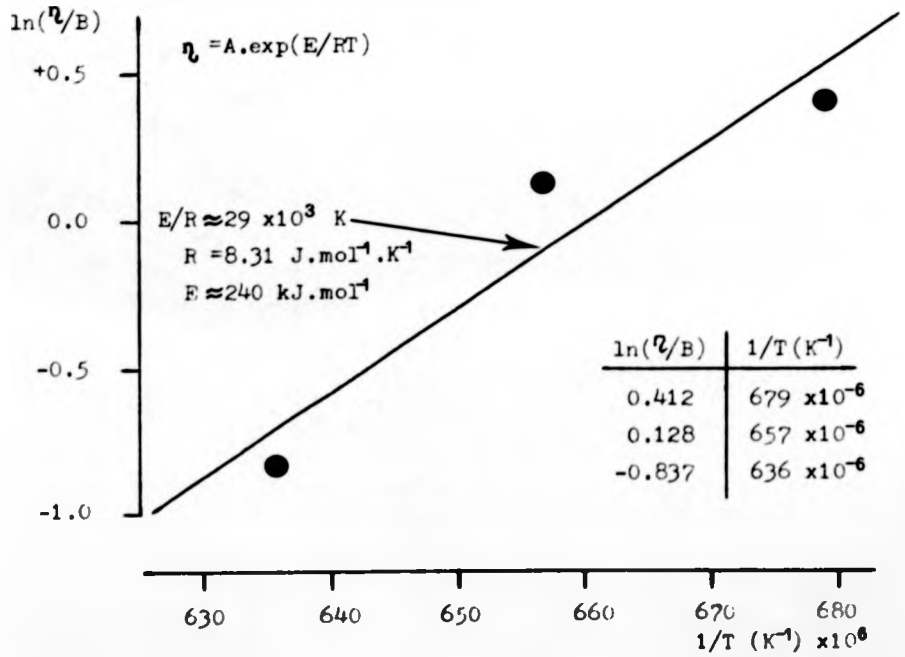

ln(η/B)	1/T(K⁻¹)
0.412	679 x10⁻⁶
0.128	657 x10⁻⁶
-0.837	636 x10⁻⁶

At low stresses $V_o \ll 2kT$, thus $\eta \approx A.\exp(\Delta E/RT)$. This leads to:-

$$\eta/B = (A/B).\exp(\Delta E/RT)$$

which enables evaluation of the activation energy, $\Delta E \approx 240$ kJ.mol^{-1}, in the temperature range 1200 - 1300°C, for S-O matrix glass.

Experimental observations have shown that the apparent activation energy for viscous flow increases with a reduction in temperature for most glass formers[107], but, for comparison, it is accepted that vitreous SiO_2 over the temperature range 1000 - 1400°C exhibits $\Delta E \approx 712$ kJ.mol^{-1}.

Above ~1350°C the free surface is found to nucleate YAG in alloys with high polytypoid addition, at lower temperatures (and at all temperatures in alloys with low and intermediate 21R addition) $Y_2Si_2O_7$ is the major phase surface nucleated. When YAG is surface nucleated there is always a considerable presence of $Y_2Si_2O_7$, probably caused by loss of nitrogen from the glass due to oxidation. However, surface nucleation of $Y_2Si_2O_7$ can occur at lower temperatures with little or no YAG formation. This effect is explained by consideration of the proposed T-T-T curves, see Figure 5.10.

The effect of the oxidation reaction upon crystallisation kinetics has been discussed, however it should be realised that crystallisation also affects the kinetics of oxidation. The formation of $Y_2Si_2O_7$, or YAG, in inter-β' channels, effectively removes Y^{3+} ions which would otherwise participate in the diffusion gradient between bulk and surface. This effect decreases oxidation rates in all alloys and was demonstrated when a partially surface crystallised specimen was sectioned and re-oxidised, the crystallised matrix region of the freshly cut surface produced far less Y^{3+} outdiffusion to the scale resulting in less formation of $Y_2Si_2O_7$ on the surface. During long-term oxidation, at ~1300°C, formation of a protective band, in which O' phase fills the inter-β' channels, produces an oxidation rate lower than that observed in untreated material[27]. Thus, selective heat-treatment may be a route to ceramics which display high oxidation resistance.

Examination of oxidised specimens which cross-sectioned part of the billet surface, proved that the outer layer, of low glass content, suffered far less oxidation corrosion than bulk billet material. Thus, components fabricated directly to size and shape specification, without surface machining operations, are expected to perform in a superior manner under high temperature oxidising conditions due to the protective influence of this ~0.6mm thick sheath.

5.5.3 Summary

The crystallisation product species have been identified and the balance of their formation has been shown to depend upon the nitrogen content of the as-sintered intergranular glass and the heat-treatment parameters.

The coarse crystallisation effect, which may occur in some alloys, has been avoided by exercise of dual dwell heat-treatments in which nucleation densities are increased.

It has been observed that the β' phase may play a role in adjusting the composition of the intergranular phase, by absorbing residual ions, during certain heat-treatments.

CHAPTER 6. - Creep deformation of Syalon ceramics at elevated temperature

6.1 Design and construction of the creep apparatus

An apparatus designed to perform high temperature uniaxial compressive creep, on a small ($3x3x5\ mm^3$) Syalon Ceramic specimen, was built. A second rig was built to the same design but the loading assembly was adapted to enable testing in the four-point bending mode of a specimen of size $3x3x35\ mm^3$.

6.1.1 The compressive creep apparatus

The apparatus was based on a design used previously by the Ceramics Research Group at Warwick and first described by Karunaratne [108]. A number of refinements were made to the original design with the aim of ;-

(1) Decreasing frictional effects present in the loading system.
(2) Removing the problem of chemical reactivity between the specimen and creep platens, through which the load is applied.
(3) Stabilising temperature zones and gradients.
(4) Decreasing and quantifying the effects of variation in ambient temperature of the creep rig.

A schematic of the loading assembly is available as Figure 6.1a. An applied load, P_1, is magnified by a factor of 51/5 along the length of the loading arm, transmitted through a floating fulcrum system, A, and applied, as P_2, through the loading assembly. The fulcrum and axle arrangement, of the loading arm, runs in oiled roller bearings to minimise frictional effects. The loading assembly consists of a brass cylinder, lined with PTFE, through which a polished steel piston loads a series of ceramic rods contained in an outer Recrystallised alumina guide tube, which is firmly seated in a steel base, G, rigidly attached to the creep rig frame. Load P_2 is transmitted through an alumina upper loading rod, B, sited over an HPSiAlON platen, D*. Below the specimen is a similar HPSiAlON platen/rod arrangement seated on another alumina rod, F. HPSiAlON was selected for use in the heat zone due to its superior creep properties with respect to alumina and its low level of reactivity with the Syalon Ceramic specimen (cf. SiC).

* The HPSiAlON used for construction of rods and platens was obtained from a billet previously shown to exhibit non-cavitating creep behaviour [34], and each platen was heat-treated at 1400°C for 600 hrs. to ensure de-segregation of all grain boundaries.

FIGURE 6.1 – The compressive creep apparatus

a

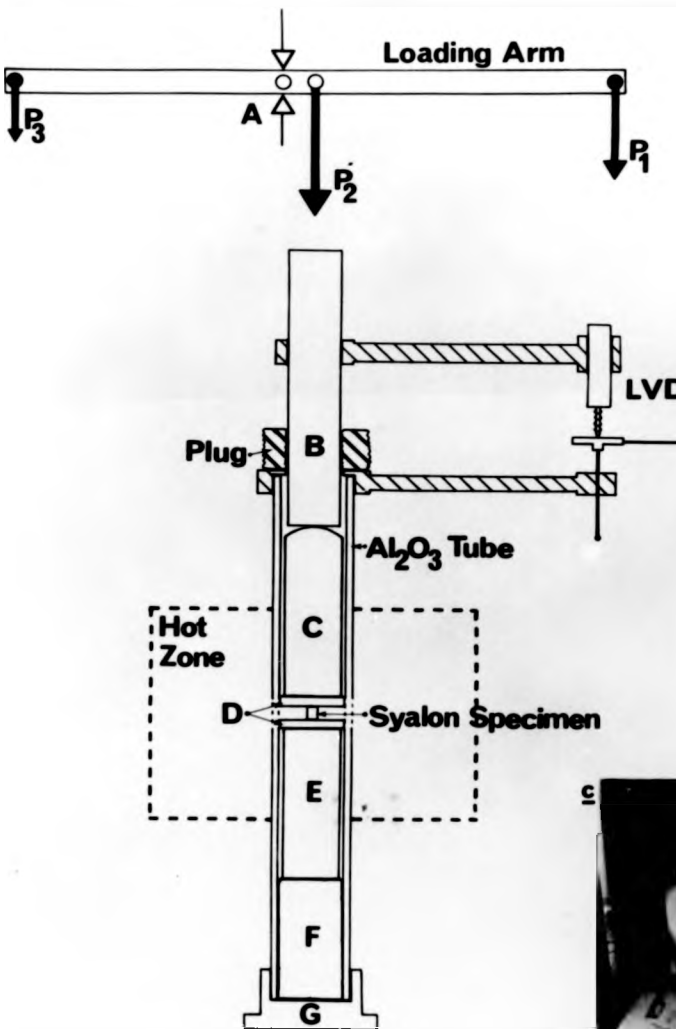

b

c

FIGURE 6.1 – The compressive creep apparatus

a

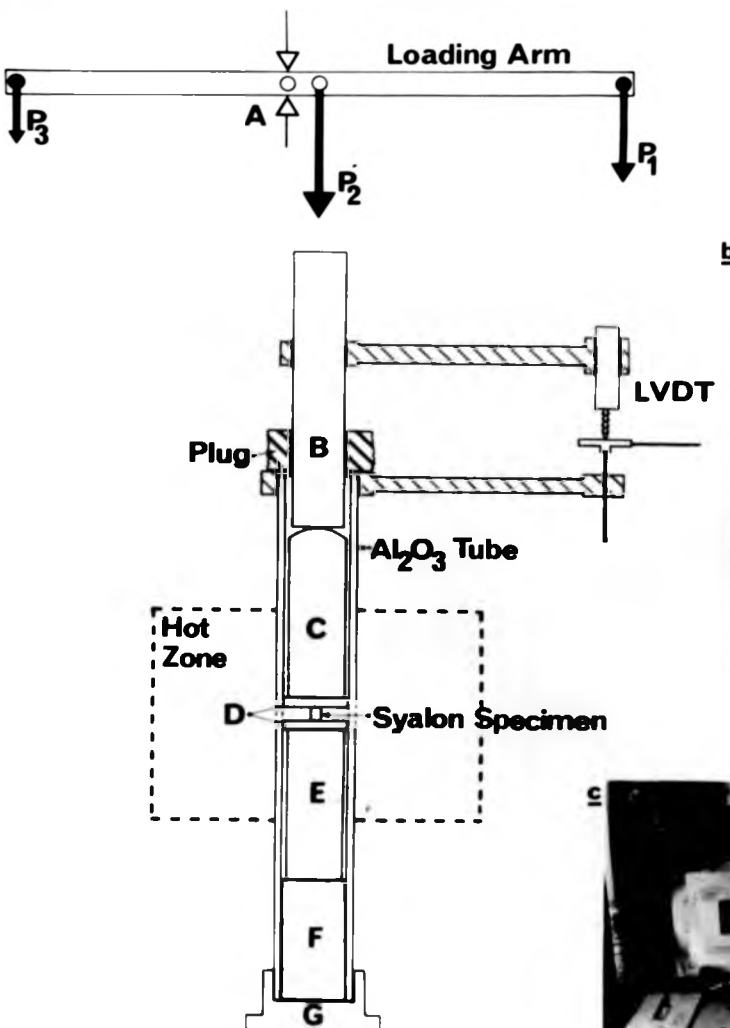

b

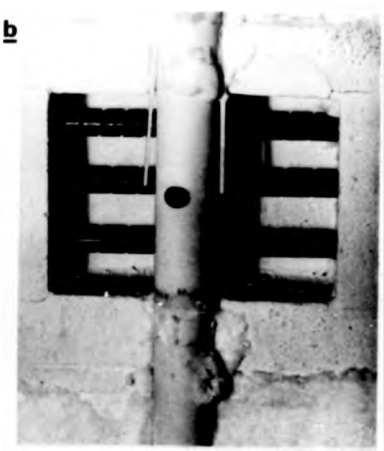

c

The creep measurement system may be considered in two parts:-

(1) A Linear Variable Differential Transducer (LVDT) of the capacitance type, Model 1071B with Model 22 DC-DC signal conditioner (Automatic Systems Laboratories Ltd.), rigidly held in an aluminium support clamped to the upper alumina loading rod (B).

(2) An LVDT stage mounted on a micrometer screw thread running in an aluminium rod clamped to the alumina guide tube.

Once adjusted for a convenient zero point the LVDT stage and core remains static while the LVDT body moves, with the upper loading apparatus, as the specimen creeps. The resulting signal is recieved and plotted by one pen of a CR652 mk.II chart recorder (J. J. Lloyd Instruments Ltd.)

To heat the loading assembly/specimen, a furnace capable of operating in excess of 1500°C was constructed. To facilitate specimen positioning a split furnace design, with contoured mating faces, was utilised, each half housing three matched Crusilite Type X SiC resistance heating elements (Morganite Electroheat Ltd), see Figure 6.1b and 6.1c. The elements were connected in series and powered from a Eurotherm Type 070 stepless temperature controller linked to two Pt-13%Rh /Pt thermocouples, aligned close to the creep specimen in the heat zone.

To decrease heat flow from the furnace hot zone to the LVDT the furnace case was lagged using mineral wool and the top of the loading assembly was plugged with alumina fibre Safil wool (ICI).

To decrease the effects of varying ambient temperature on the creep rig, it was housed in a small room with a recycling thermostatically controlled air temperature conditioner. A thermistor device and amplifier, connected to a twin-pen chart recorder, enabled simultaneous recording of creep rate and LVDT temperature, thus enabling true creep rate to be determined, despite variation in ambient temperature.

6.1.2 The four-point bend creep apparatus

A frame and furnace of the same design as that utilised for high temperature compressive creep characterisation was built for testing in the four-point bending mode. Figure 6.2a is a schematic representation of the loading assembly. The load, P, is applied directly to the loading assembly, since magnification along the loading arm is

FIGURE 6.2 – The four-point bend apparatus

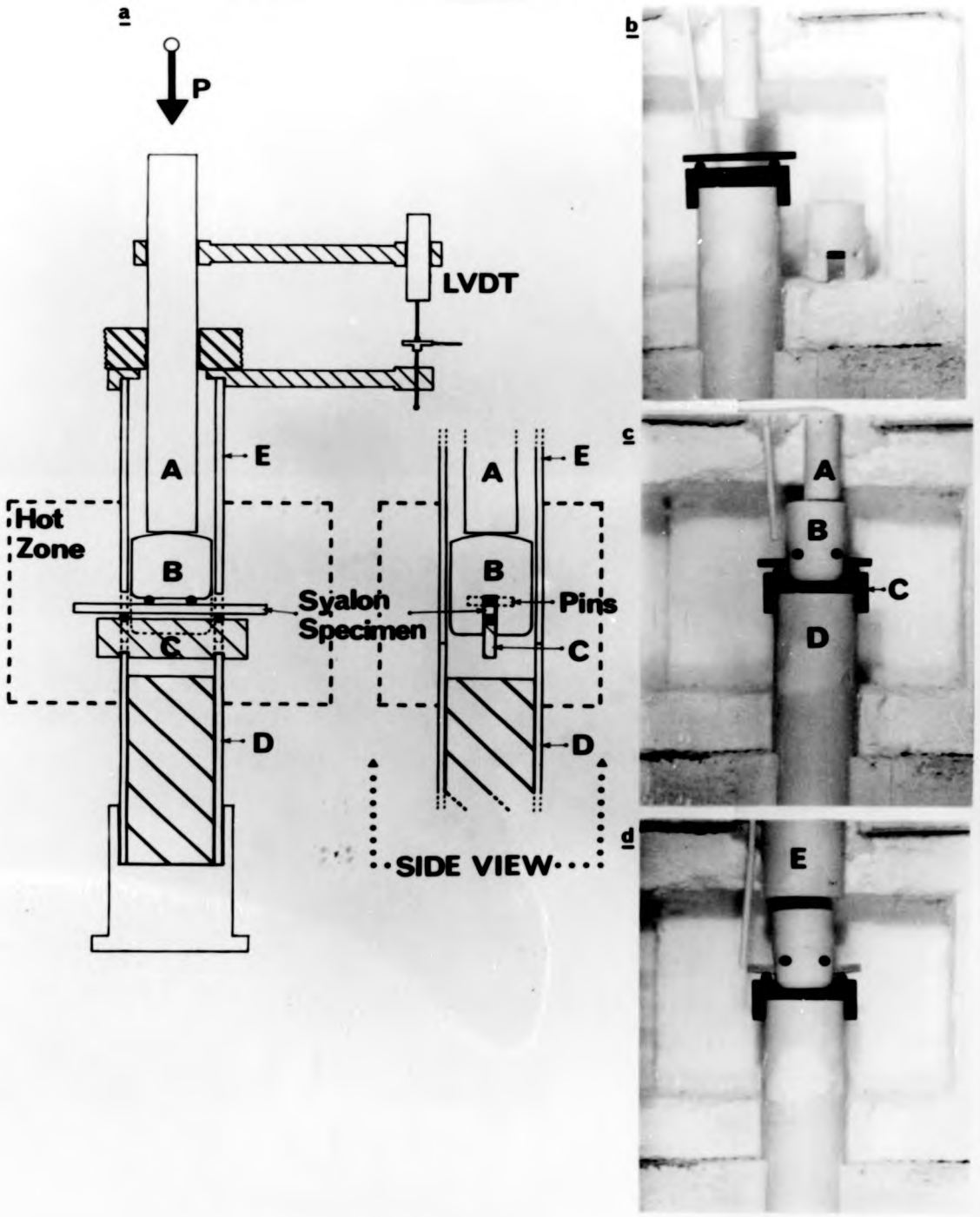

FIGURE 6.2 – The four-point bend apparatus

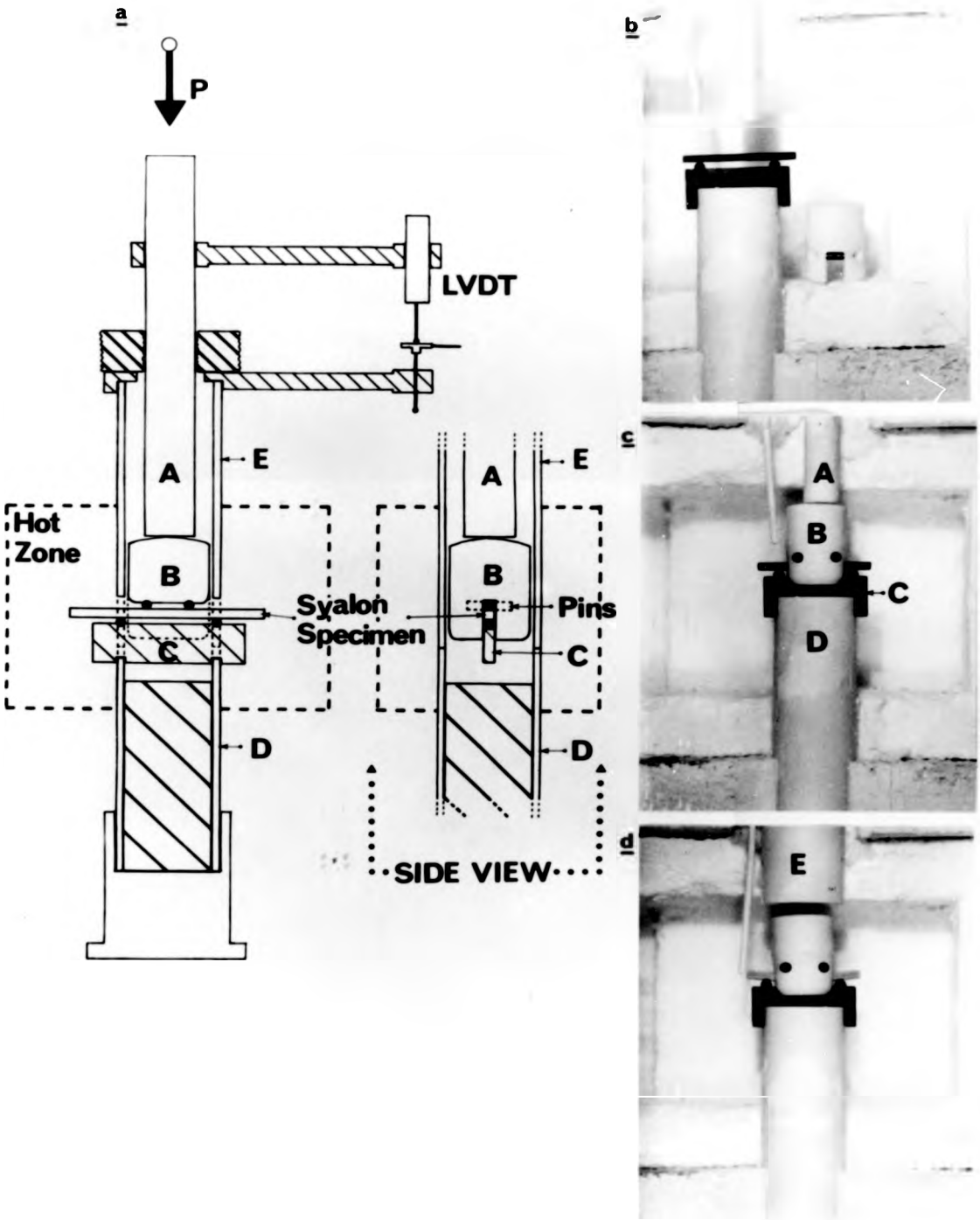

not neccesary to achieve measurable creep rates in a four-point bending specimen of the designated size. However, a loading arm is still included in the apparatus to balance the mass of the loading assembly, provide stability and enable the apparatus to be easily adapted to the compressive creep mode if so desired. The specimen is loaded between four HPSiAlON ceramic, cylindrically machined, pins. The two upper pins are seated in an alumina upper loading head, B, which straddles the specimen and a 'Refel' SiC specimen support beam, C. The two lower pins are seated in grooves machined into the SiC beam, through which load is transmitted via an alumina tube, D,seated in a steel base connected to the frame. An upper alumina guide tube, E, keeps the loading head centralised and serves as a clamping base for the LVDT stage support.

A Schaevitz Model 500DCB LVDT was used to monitor creep, with simultaneous LVDT temperature assessment by thermistor, recorded on a CR652 mk.II twin pen chart recorder, as used for compressive creep.

The apparatus was sited in the same temperature controlled creep laboratory as the compressive creep rig.

6.1.3 Calibration of the creep apparatus

By using a standard Pt-13%Rh /Pt probe thermocouple, the operating temperature in the heat zone of both furnaces was calibrated and found to be constant ± 10°C,throughout its volume, in the temperature range 1000 - 1450°C.

Calibration of the transducers/chart recorders was completed 'in situ' above the furnaces at operating temperatures:-

(1) The compressive creep transducer (1071B) showed complete linearity over its full range at 47°C with an output of 2.048 $V.mm^{-1}$ (cf. 1.93 $V.mm^{-1}$ at room temperature).

(2) The four-point bend creep transducer (500DCB) also exhibited linear behaviour,with an output of 468 $mV.mm^{-1}$ at 45°C (cf. manufacturers claim 500 $mV.mm^{-1}$ at room temperature).

6.2 Experimental procedure

To avoid specimen buckling or barreling effects during compressive creep experiments, the ratio of height, h, to breadth, b, should lie in the range $2.5 > h/b > 1.5$ [109] and thus specimens of size $\approx 3x3x5\ mm^3$ ($h/b \approx 1.7$) were produced for testing. Care was taken to cut square ends, enabling axial loading.

In the four-point bend loading apparatus the lower loading point span, L = 30mm, and the upper loading point span, a = 15mm, were chosen so that the span ratio, L/a = 2, lies in the region of stress exponent, n, insensitivity to strain, and enables measurable deflection rates, even at low stress levels[82]. Thus, specimens of size 3x3x35 mm^3 were cut for testing.

The loading apparatus in both creep rigs was vertically aligned to ensure freedom from frictional effects.

After polishing the specimen to a 6μm diamond paste finish, its mean dimensions were recorded using a micrometer and it was carefully aligned in the loading position in the creep rig:-

(1) The compressive creep specimen is clearly seen through the small access hole in the outer guide tube of Figure 6.1b. This photograph was obtained upon completion of a creep test, thus the specimen is sheathed in a crystalline oxide scale which is light in colour.

(2) The four-point bend specimen is seen upon the lower loading points in Figure 6.2b and the loading head is positioned above it in Figure 6.2c, prior to lowering of the outer guide tube. For clarity the heating elements have been removed from the heat-zone.

The furnace halves were brought together and locked in position and the rig run up to temperature at a rate of $\sim 3^{\circ}C.min^{-1}$ with a small load on the specimen. After soaking at temperature overnight, to ensure stable thermal gradients within the furnace and seating of the specimen on the platens/loading points, the transducer zero setting was adjusted to allow for a maximum recording range during creep.

All creep runs were conducted at constant temperature. After monitoring an 'apparent steady state creep rate', at a given load, the stress was increased by application of a load increment. Cycles of incremented load increase were recorded, on the chart recorder, from selected specimens, with inter-cycle recovery time sufficient to remove the tendency for negative visco-elastic effects.

Upon removal of the specimen from the creep rig, at the end of a test, the platens were re-polished and oxidised at $1350^{\circ}C$ for 50hrs, prior to replacement in the loading system. The specimens were examined by eye and with electron optical techniques.

6.3 Results of creep experiments performed on Syalon Ceramics

6.3.1 Alloy S-0

A set of isothermal creep experiments was performed, in the four-point bend mode, on specimens of alloy S-0, in the temperature range 1100-1250°C with ~50°C increments between each test. Derivation of the stress exponent, n, applicable to S-0/1160°C creep is described in Figure 6.3A, a log-log plot of specimen deflection rate, $\dot{Y}_L$, (from a chart roll recording mm deflection /mm time) versus load (kg applied to specimen). From the figure it is apparent that creep of S-0 is characterised by two stress exponents in two stress regimes at 1160°C. A log-log plot of creep rate, $\dot{\varepsilon}_{max}$, versus applied stress, σ_{max}, in the high stress regime is presented as Figure 6.3B, in which n=3 was substituted into the equations for outer fibre stress and strain rate.

In both plots of Figure 6.3 lines are constructed through data points ascertained by measurement of $\dot{Y}_L$ at times of 25×10^3s (25ks), 50ks and 75ks after applying a specified load. From the data it is apparent that true steady-state creep is not achieved within 75ks after applying a given load. The symbol ✪ is plotted at the point $\ln\sigma = 18$, $\ln\dot{\varepsilon} = -18$ to facilitate comparison with other creep data presented in this thesis.

Similar creep data was obtained from alloy S-0, initially loaded in the as-sintered condition, at temperatures of 1100°C, 1200°C 1250°C and the results are presented in Figure 6.4, in which the value n=1.5 was substituted into the equations for ε_{max} and σ_{max}. It should be noted that this leads to an overestimate of the creep performance, in the high stress regime, of S-0 ceramic at 1100 and 1160°C. Data obtained from pre-oxidised HPSiAlON[34] is also presented for comparison.

(a) S-0/1100°C creep

Post-test examination indicated a significant presence of SCG on the tensile face of this specimen. A thin glassy oxide scale was found to sheath the specimen, but at 1100°C the oxidation reaction is insufficient to promote gross cation outdiffusion and reduction of glass volume. Despite the occurrence of SCG a large improvement in creep resistance occurs between 75ks and 225ks after loading, and this effect must be due to crystallisation of $Y_2Si_2O_7$ (the total time at 1100°C for this test was ~500hrs.) from the matrix. Data in the low stress regime fits an n=1 Newtonian viscous flow mechanism, but at higher stresses intergranular cavitation linked by SCG from the tensile face is

FIGURE 6.3 - Derivation of the stress exponent, n, and creep of alloy S-0 at 1160°C

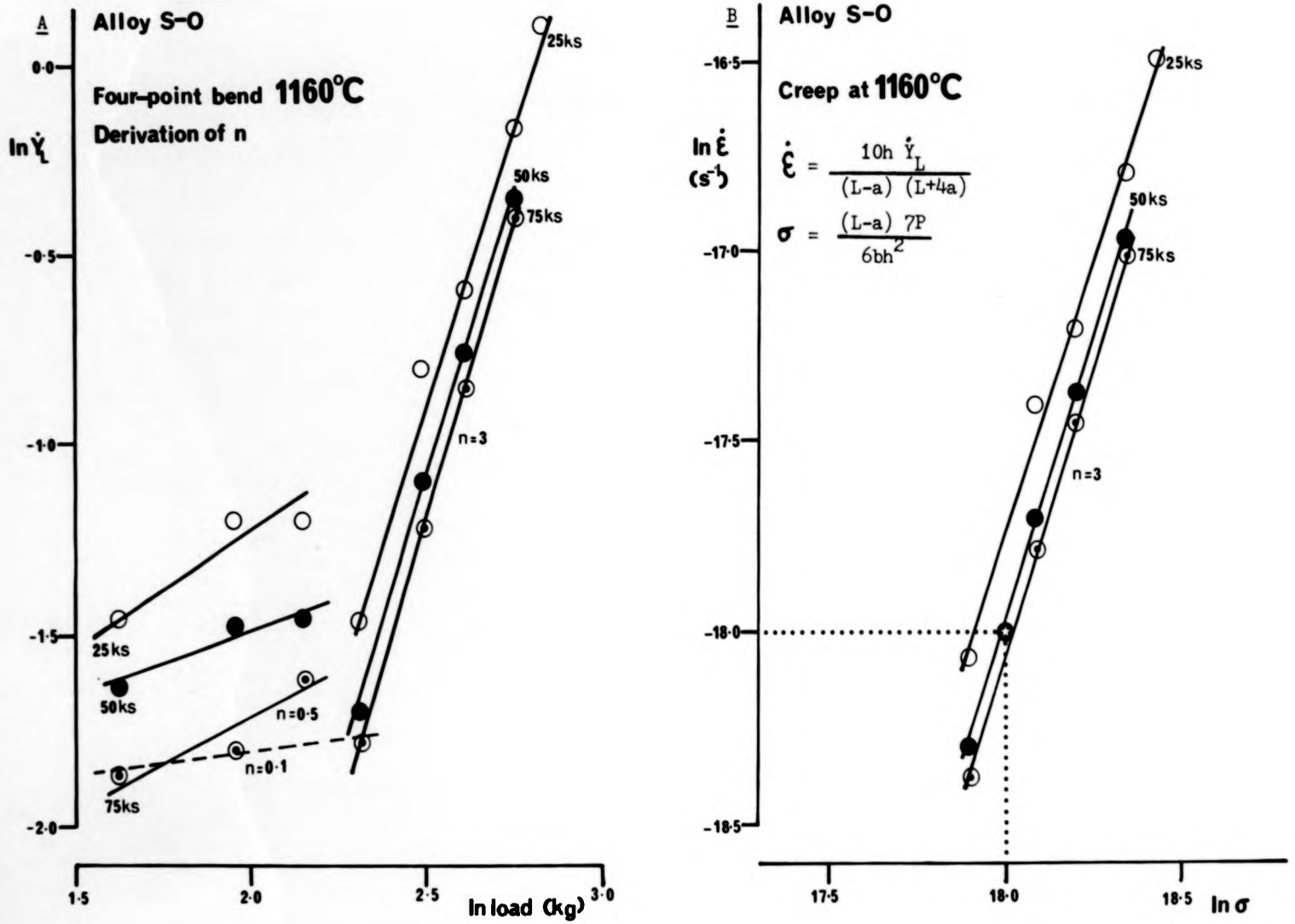

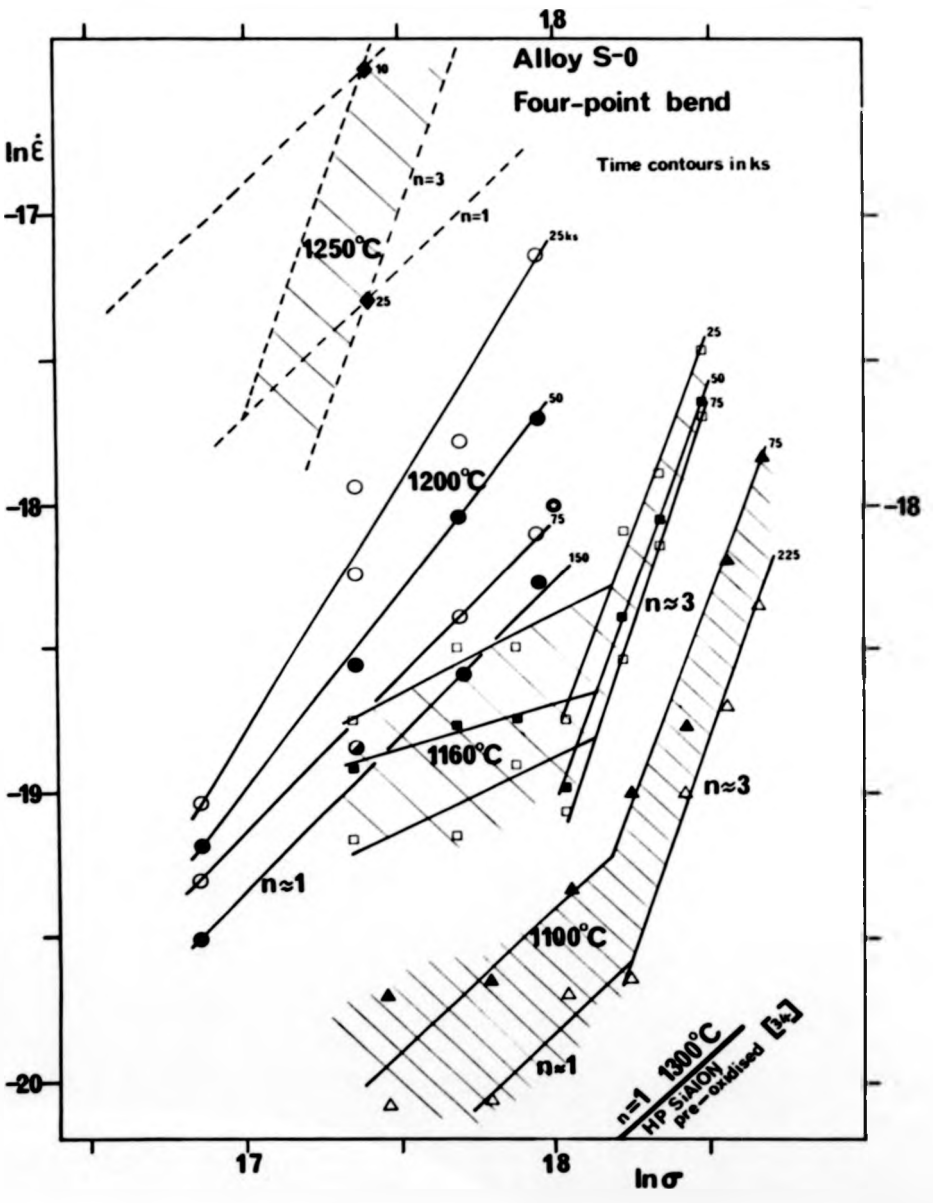

FIGURE 6.4 - Four-point bend deformation of alloy S-0 at different temperatures
(separate isothermal experiments)

characterised by n=3 behaviour.

(b) S-0/1160°C creep

Post-test examination indicated very extensive SCG on the tensile face of this specimen and some $Y_2Si_2O_7$ formation in the thin oxide scale. The creep behaviour is very similar to that found at 1100°C, although improvement in pseudo-steady state creep rates occurs more rapidly due to enhanced oxidation and crystallisation effects.

(c) S-0/1200°C creep

In the stress regime under investigation no SCG occurred, and behaviour is characterised by viscous flow through the residual grain boundary glass. Large improvement in creep resistance occurs via oxidation and crystallisation.

(d) S-0/1250°C creep

The extremely high creep rate precluded long term testing, and data was only recorded at one stress level. The large volume of highly fluid residual glass in this material implies a very low temperature ceiling for constant engineering application.

6.3.2 Alloy S-10.75A

The compressive creep of alloy S-10.75A, at 1300°C, initially loaded in the as-sintered condition, is characterised by the unshaded data plots in Figure 6.5, taken from long term tests in three separate loading cycles. Four-point bend, 1300°C, tests were also performed on pre-heat-treated specimens of this ceramic. After a dual dwell YAG crystallisation treatment and extended oxidation stage, initial pseudo-steady state creep is characterised by n=1 behaviour, with possible cavitation occurring at long test times giving rise to n=1.5 character. Creep after a low temperature mono-dwell pre-treatment, to promote $Y_2Si_2O_7$ crystallisation and oxidation, is also characterised by n=1 behaviour, and at the highest stress level the initiation of tertiary creep behaviour is noted.

The lower residual glass volume and superior crystallisation behaviour of this ceramic leads to higher creep resistance than that exhibited by alloy S-0. The mechanism for improvement of creep resistance, with time, of ceramic S-10.75A is discussed in Section 6.4.

6.3.3 Other ceramics

A specimen of S-11.5 was pre-treated 1100°C/5hrs.,

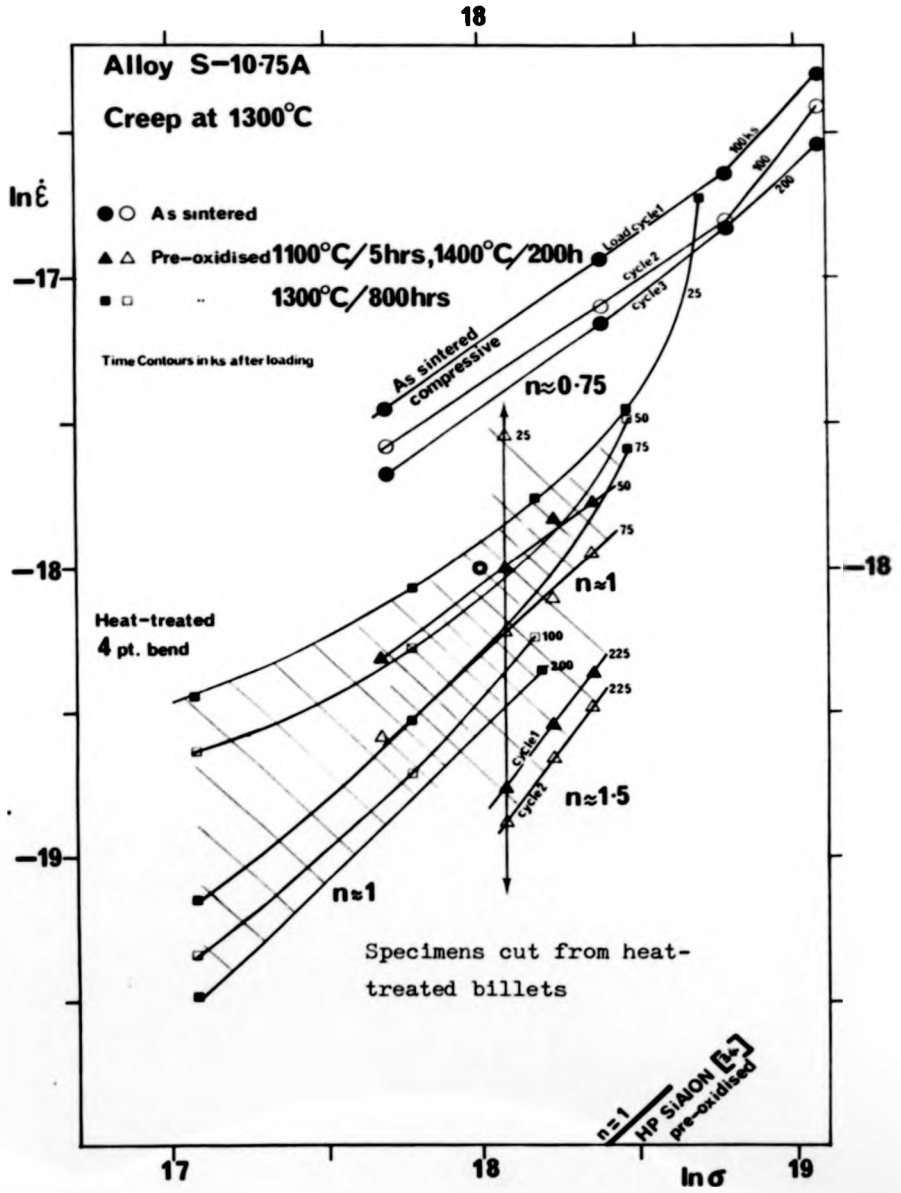

FIGURE 6.5 - Creep of alloy S-10.75A, loaded in the as-sintered state (compression) and loaded after oxidising/crystallisation pre-treatments (four-point bend)

1400°C/200hrs. to promote YAG crystallisation and remove residual glass via oxidation. The compressive creep performance, at 1300°C, of this specimen is documented in Figure 6.6 where the n=1.75 characteristic is readily appreciated.

A new Syalon Ceramic, K-8.5, fabricated with Kennametal Si_3N_4 powder on a sinter cycle of 1650°C/2hrs., 1800°C/5hrs. with nucleation and crystallisation dwells at 1250°C/7hrs. and 1400°C/5hrs., was also investigated. Since this ceramic was crystallised as part of the sinter cycle, the creep specimen was completely unoxidised when loaded into the compressive creep rig. Thus, a large improvement in creep resistance was monitored, with final behaviour characterised by n=1, due to the oxidation reaction. Further aspects of this behaviour are discussed in Section 6.4.

Upon removal from the creep rig examination of the oxide scale outer surface, in the SEM, showed the presence of $Y_2Si_2O_7$ and mullite ($Al_6Si_2O_{13}$). The HPSiAlON creep platens contained small surface depressions where the specimen had seated, and some contribution to the measured creep must be derived at this effect.

6.4 Discussion - The creep behaviour exhibited by Syalon Ceramics

Since only isothermal experiments were performed, it is not possible to obtain a meaningful value for the activation energy for creep, Q, and thus complete characterisation of the creep mechanisms occurring in Syalon Ceramics cannot be made from the data alone. However, post-test examination of the specimens provides evidence which may be related to the deformation process and this, when considered with the data, enables some qualitative comparison to be made between different ceramic alloys.

6.4.1 Secondary stage creep of Syalon Ceramics with various amounts of 21R addition

Common to all ceramics tested was the lack of a true steady-state secondary creep stage. Instead, microstructural evolution during the test gave rise to a long term improvement in creep resistance and pseudo-steady state behaviour.

In the four-point bend mode, creep of alloy S-10.75A is characterised by n=1 behaviour at 1300°C, regardless of the major devitrification product initially formed during an oxidising crystallisation

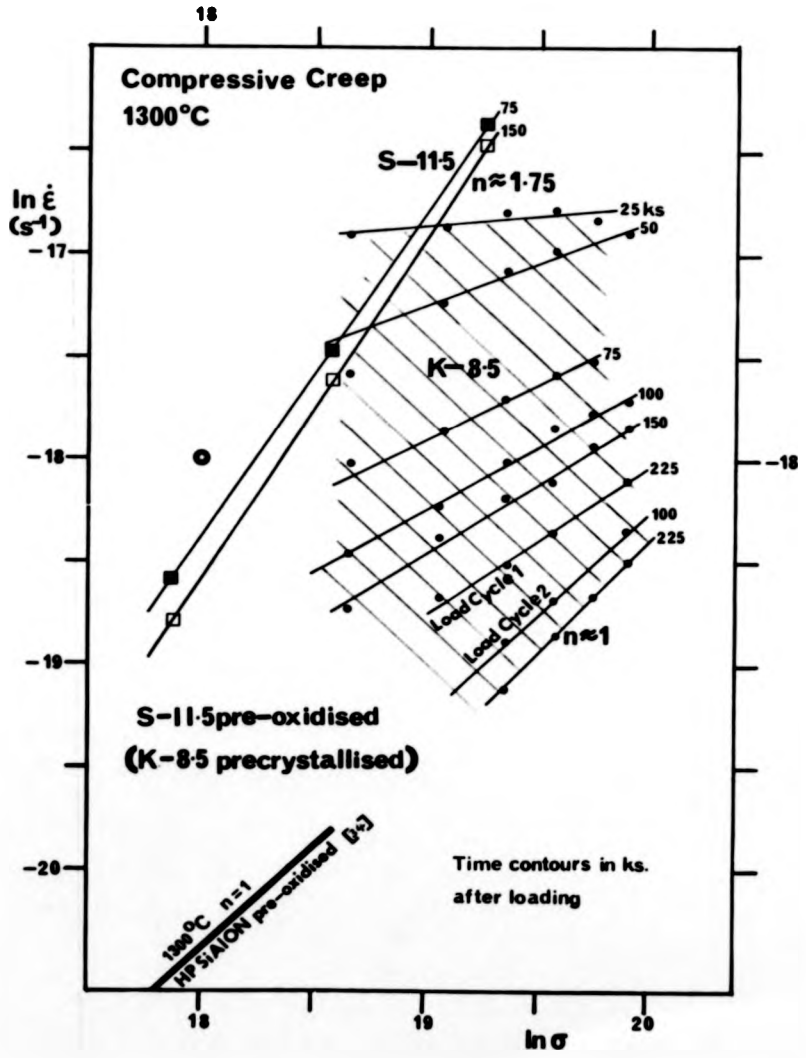

FIGURE 6.6 - The compressive creep of alloys S-11.5 and K-8.5, at 1300°C

pre-treatment. However, a specimen of the same alloy loaded in the as-sintered condition was found to exhibit a higher creep rate despite being loaded in the uniaxial compressive mode in which tensile forces are lower and SCG unlikely.

Sub-surface transformations occurring during oxidation (in the heat-treatment or creep furnace) occur in materials with glass matrices and are dominated by yttrium out-diffusion. Formation of O' phase (Si_2N_2O with aluminium in solid solution) occurs, increasing oxidation and creep performance. Reversion of YAG phase to liquid is also possible due to formation of a diffusion couple with the SiO_2 rich surface scale, and subsequent transformation to O' again leads to improved creep and oxidation resistance.

Within the bulk of the ceramic morphological changes occur during creep. With increasing time, crystallisation of the matrix phase can move towards completion, residual Si, Al, O and N ions being taken into β'_{ss}. Upon completion of crystallisation the isolation of YAG grains into a more disconnected form is driven by a decrease in β'/YAG interfacial energy. This further decreases oxidation, since diffusion along β'/β' boundaries is slower than diffusion along relatively wide liquid filled channels.

The larger glass volume fraction present in alloy S-0 and porosity generated during surface crystallisation, lead to cavitating behaviour above a critical stress, interlinkage of cavities/pores promoting SCG from the tensile face. Above $\sim$1250°C the relatively low viscosity of the low nitrogen glass in this alloy results in very high creep rates.

6.4.2 Comparison of creep behaviour exhibited by alloys S-11.5 and K-8.5

It was noted that the creep rates of S-series ceramics are considerably higher than those of ceramics produced earlier in the Syalon Ceramic research programme from Union Carbide and Norton source Si_3N_4[110]. Using x-ray photoelectron spectroscopy (ESCA), it was shown[111] that "α-Si_3N_4 provided by H C Starck Ltd. contains significant amounts of fluorine, derived from the HF acid leaching stage in which impurities are removed". Since fluorine was not detected in the intergranular glasses of alloys S-0 and S-10.75A and B by using EELS, see Figure 4.16A, it is evident that the amounts involved are rather small. However, the presence of 1% Fluorine in fused silica has been shown to reduce viscosity by $\sim$3 orders of magnitude, F^- replacing O^{2-} in the

structural network , resulting in proliferation of non-bridging links[112] and amounts undetectable by EELS could change YSiAlON glass properties by significant amounts. After crystallisation of the matrix phase any fluorine would be greatly concentrated in the residual glass between grain boundaries, and would promote cavitation effects above a critical stress, at a given temperature, during creep. Nb. Some F^- can be accomodated within the structure of yttrialite ($Y_2Si_2O_7$), but not in YAG.

The presence of fluorine may also explain the observation that Starck source α-Si_3N_4 based alloys require lower temperatures for densification than do ceramics fabricated with materials provided by other manufacturers.

Alloy K-8.5 was found to show superior creep resistance to S-10.75A and S-11.5, and cavitation was not present despite testing at very high stress levels. This alloy does contain iron impurity but there is no evidence for presence of F^-, and it is possible that this is a major factor contributing to the improved performance under load at elevated temperatures.

6.4.3 Summary

Ceramics fabricated with 21R addition show creep resistance superior to alloy S-0 fabricated without 21R and containing very little nitrogen in the intergranular glass.

Morphological changes occurring in the sub-surface and bulk of a ceramic, due to oxidation and crystallisation reactions, cause a time dependent transient behaviour in the creep rig.

There may be an inherent problem with the creep resistance of ceramics fabricated with LC.10 source Si_3N_4 due to the presence of F^- ions in the intergranular phase.

CHAPTER 7.- Conclusions and suggestions for future work

(a) Conclusions

The following conclusions may be drawn from the work presented in this thesis:-

(1). The density of Syalon Ceramic composites prepared over a wide compositional range is 3.23-3.24 $g.cm^{-3}$.

(2). Addition of 21R to a Syalon composition changes the β' grain size distribution from approximately monomodal to approximately bimodal and increases the mean alumina substitution level, z, as described by the empirical relation:-

$$z = (0.035\ ^{w}\%21R) + 0.24$$

Above $\sim 10\ ^{w}\%21R$ addition formation of α' phase is evidenced in the microstructure of S-series ceramics.

(3). With increasing mean alumina substitution level, $\bar{z}$, the β'_{ss} hexagonal unit cell parameters, a and c, are found to increase as described in the literature.

(4). The volume fraction of interganular glass, Vg, is found to increase with addition of yttrium and oxygen to a composition, as seen in the empirical relation:-

$$Vg\% \approx [4.736^{a}\% (Y + O)] - 34.692$$

(5). Addition of 21R increases the intergranular phase N/O ratio, and this affects crystallisation behaviour promoting formation of YAG over formation of $Y_2Si_2O_7$, at a given heat-treatment temperature.

(6). Increase in heat-treatment temperature, within the devitrification interval, is seen to increase the product YAG/$Y_2Si_2O_7$ ratio in a given ceramic alloy.

(7). β-$Y_2Si_2O_7$ is found to crystallise on the oxide scale surface while α-$Y_2Si_2O_7$ is identified in the intergranular matrix of Syalon Ceramics. YAG is found to contain a small amount of silicon in solid solution, and phase separation, in the form of SiO_2 globules, is visible in the YAG of certain alloys after specific heat-treatments.

(8). Correctly tailored dual dwell heat-treatments are found to

increase nucleation densities within the intergranular matrix, although the mode of nucleation appears to be predominantly heterogeneous.

(9). Increase of intergranular glass nitrogen content, upon addition of 21R, and decrease in intergranular phase volumes, are seen to increase Syalon Ceramic composite creep resistance.

(10). Morphological changes occurring in the sub-surface and bulk of the ceramics, due to oxidation and crystallisation reactions, cause a time dependent transient creep behaviour.

(11). There may be an inherent problem with the high temperature performance capability of Syalon Ceramics produced with H C Starck source α-Si_3N_4, due to the presence of fluorine.

(12). Components fabricated directly to size and shape specification, without use of post-sinter surface machining operations, are expected to perform in a superior fashion to machined articles, due to the protective influence of the $\sim$ 0.6mm surface sheath derived during sintering.

(b) Future work

Application of microcomputer technology to creep experiment data recording has been found to allow more flexible processing of results. Further work performed on alloy K-8.5 has confirmed the non-cavitational behaviour reported in this thesis and it is recommended that alloys fabricated with α-Si_3N_4 powder from other manufacturers be tested.

In order to maximise bulk properties of newly developed alloys study of their devitrification behaviour and development of applicable heat-treatment schedules must be made.

Generation of O' layers, sheathing ceramic alloys, should be further explored and pre-treated specimens subjected to mechanical testing.

Since many components may be formed directly to shape, or green-machined prior to sintering, they are expected to perform in a superior manner due to formation of a protective layer during sintering. It is therefore suggested that mechanical test specimens be sintered directly to shape in order to assess the likely properties of such 'protected' material.

APPENDIX 1.- Calibration of EDAX data using 'standard' materials

1. TEM/EDAX data

For a material containing two or more elements consider X-ray analysis of sections sufficiently thin to allow interelement absorption and fluorescence effects to be ignored. The relationship between elemental concentration, C_i, and the observed intensity, I_i, of their characteristic x-ray lines may be written;

$$C_x : C_y : C_z = I_x/P_x : I_y/P_y : I_z/P_z \quad \text{(Cliffe-Lorimer)}$$

where P_i is the relative intensity of an element calculated for given microscope conditions and available in tabulated form - see Table A1. Thus, in theory, EDAX from thin sections in the TEM is a technique which does not require the use of standards.

TABLE A1 - P_i for 100kV electrons, and keV's at which characteristic x-ray lines may be observed, for various elements

Element	K_α		L_α	
	P_i(100kV)	keV	P_i(100kV)	keV
12 Mg	0.45	1.253	0	/
13 Al	0.57	1.486	0	/
14 Si	0.66	1.739	0	/
20 Ca	0.93	3.690	0	0.341
26 Fe	0.99	6.398	0.052	0.705
39 Y	0.57	14.931	0.44	1.922

In the analysis of materials composed principally of aluminium, silicon and yttrium (oxides) it appears (from Table A1) convenient to use the AlK_α, SiK_α and YL_α lines to determine composition due to their close proximity in the x-ray spectrum. However, in practice the YL line is observed to be asymmetric in its intensity/energy profile due to the presence of $YL_{\beta,\delta,\delta}$ and M_α characteristic lines - see Figure A1. Since $YL_{\beta,\gamma,\delta}$ line information is not readily available it is relevant to perform a calibration procedure on data acquired from the TEM using EDAX spectra from 'standard' materials.

Figure A1 - Comparison of x-ray spectra composed of various energy lines characteristic of yttrium

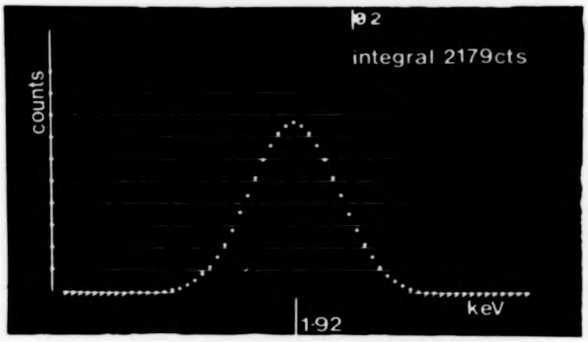

profile of YL_{α} characteristic x-ray line.

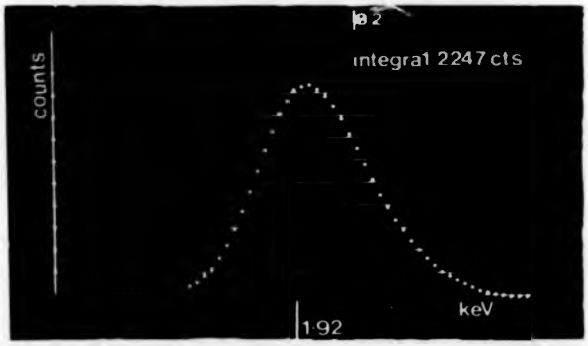

profile composed by superposition of YL_{α}, YL_{β}, YL_{γ}, YL_{ζ}, and YM_{α} lines.

Data from EDAX 9100 system with peak identification and peak generation software.

2. SEM/EDAX data

For the case of EDAX from SEM specimens, of thick section, effects arising from interelemental absorption and fluorescence must be accounted for, and further calculations (ZAF corrections) are required to yield quantitative data. Again, analysis of 'standard' materials allows calibration of EDAX spectra.

3. Preparation of 'standard' materials

'Standard' materials were prepared by reacting 'Analar' grade oxides as detailed below.

(a) Al_2O_3 - SiO_2 binary system - A standard of specified composition $Al_2O_3.SiO_2$ was already available presumably composed of Mullite/SiO_2, the specimen was polished and carbon coated for analysis in the SEM.

(b) Al_2O_3 - Y_2O_3 binary system - A standard of overall composition $3Y_2O_3.5Al_2O_3$ was prepared by milling the oxides for 72 hrs., pressing green compacts of size $\sim$40 x 30 x 5mm^3 and sintering in an open tube furnace. One sample was sintered at 1450°C for 120 hrs. and another at $\sim$ 1750°C for 30 mins. Inspection of XRD spectra led to identification of Yttrogarnet (ASTM Index card 8-178) and Yttrium Aluminate (card 9-310), both of formula $Y_3Al_5O_{12}$, in the 1450°C sintered material. These two phases were also found to be the major content of the 1750°C material, but extra lines, of low intensity, were also present in the XRD pattern. Both specimens were prepared for analysis in the SEM and finely ground grains of the 1450°C material were scattered over a carbon film, mounted on a copper grid, for X-ray analysis and SAD in the TEM.

(c) Al_2O_3 - SiO_2 - Y_2O_3 system - A homogeneous glass of composition 21.5^w% Al_2O_3, 45.0^w% SiO_2, 33.5^w% Y_2O_3, corresponding to the ternary eutectic point, was prepared by melting at 1550°C. XRD provided no evidence for crystalline phase content and so the oxides were considered to be fully reacted. Samples were prepared for X-ray analysis in both the SEM and TEM.

4. X-ray microanalysis and standardisation of EDAX spectra

(a) SEM/EDAX - Each material was examined in the backscattered electron mode to check homogeneity and then, under standard conditions, five analyses of each specimen/phase were obtained with x-ray collection terminated at a full scale reading of 5000 counts. After correction for ZAF the mean analysis and its associated 'standard error' were calculated for each specimen/phase. The data so obtained for the $Al_2O_3.SiO_2$ standard is presented in Table A2, the small standard error indicates the high degree of consistency obtainable from analysis in the SEM, and the slight difference between expected and analysed results is understood by considering the accuracy of background fitting and peak fitting capabilities of the computer.

The x-ray spectrum obtained from $Y_3Al_5O_{12}$ is readily identified[38] and was therefore selected for derivation of the normalisation parameter F;-

Ignoring undetectable oxygen atoms, mean analysis from $Y_3Al_5O_{12}$ after ZAF correction is 55.659^a% Al, 44.341^a% Y.

Therefore, Y/Al = 3/5 =(44.341xF)/55.659 => <u>F = 0.753</u>

Thus the analysed ^{a}% Y after ZAF should be multiplied by the factor 0.753 and the total specimen composition normalised to 100^a% to obtain a calibrated analysis. Application of the F parameter enables identification of a minor phase found in the 1650°C sintered specimen as $Y_2Al_2O_6$, and proves that glass observed in the microstructure is of a composition very close to the lowest melting (1760°C) eutectic in the Y_2O_3 - Al_2O_3 system, as expected by consideration of the phase diagram- see Table A2 and the Al_2O_3 - Y_2O_3 phase diagram of Figure 2.2. Further validation of F = 0.753 applied to the YL line is provided by comparison of the 'analysed' and 'as milled' compositions of the ternary oxide eutectic glass.

(b) <u>TEM/EDAX</u> - Thin crystals of the 1450°C sintered $Y_3Al_5O_{12}$ specimen exhibited SAD patterns characteristic of the cubic YAG phase. EDAX spectra were recorded from five such crystals,under standard conditions, and after background subtraction the intensity of the AlK_α and YL characteristic lines were assessed using a ruler to measure peak height from an extended full scale print-out. The mean peak heights were calculated and a P_{YL} factor derived;-

Mean peak heights from $Y_3Al_5O_{12}$ are: AlK_α 92.6mm,
YL 89.4mm.

Y : Al = 3:5 = $(89.4/P_{YL})$: (92.6/0.57) => <u>P_{YL} = 0.92</u>

Analysis of the ternary oxide eutectic glass and application of the factors P_{AlK_α} = 0.57, P_{SiK_α} = 0.66, P_{YL} = 0.92 led to the composition presented in Table A2 which is in excellent agreement with both the composition measured using SEM/EDAX and with the 'as milled' composition.

TABLE A2 - Analyses obtained from EDAX on 'thick sections' in the SEM and from 'thin sections' in the TEM

	a% Element	Standard	Thick section ZAF + Normalisation	Thin section $P_{Si} = 0.66$ $P_{Al} = 0.57$ $P_Y = 0.92$
(1) $.Al_2O_3.SiO_2$				
	a% Al	66.7	64.7 ± 0.3 *	/
	a% Si	33.3	35.3 ± 0.3 *	/
(2) $Y_3Al_5O_{12}$				
	a% Al	62.5	62.5	62.5
	a% Y	37.5	37.5	37.5
(3) $Y_2Al_2O_6$				
	a% Al	50.0	52.1 ± 0.3	/
	a% Y	50.0	47.9 ± 0.3	/
(4) Al_2O_3 - Y_2O_3 system Eutectic Glass (1760°C)**				
	a% Al	76.9	76.1 ± 0.5	/
	a% Y	23.1	23.9 ± 0.5	/
	(Si, Fe, Cl, Ca, K, S, impurities also present)			
(5) Al_2O_3 - SiO_2 - Y_2O_3 system Eutectic Glass***				
	a% Al	28.7	27.9 ± 0.3	27.1 ± 0.5
	a% Si	51.0	50.7 ± 0.7	51.2 ± 0.7
	a% Y	20.2	21.5 ± 0.5	21.7 ± 0.3

All data from thick sections normalised by applying a factor F=0.753 to the Y content obtained after ZAF correction, as determined by analysis of $Y_3Al_5O_{12}$.

All data from thin sections obtained by applying a P factor to the Y_L line intensity of P_Y=0.92, as determined by analysis of $Y_3Al_5O_{12}$.

* No normalisation applied, since no Y present.

** Eutectic composition 60 w% Al_2O_3, 40 w% Y_2O_3.

*** Eutectic composition 21.5 w% Al_2O_3, 45.0 w% SiO_2, 33.5 w% Y_2O_3.

REFERENCES

[1] R N Katz; 'Progress in Nitrogen Ceramics', ed. F L Riley, Nijhoff (1983), 728.

[2] R J Lumby et al; ibid, 683-694.

[3] J I Mueller; Amer. Ceram. Soc. Bull. 61 (1982), 588-590.

[4] S Robb; Amer. Ceram. Soc. Bull. 62 (1983), 206.

[5] W Bakker and D Kotchick; Ceram. Eng. and Sci. Proc. 13 (1982), 793-809.

[6] D C Larsen et al; reference [1], 695-710.

[7] P Chantikul et al; J. Amer. Ceram. Soc. 64 (1981), 533-543.

[8] W R Cannon and T G Langdon; J. Mat. Sci. 18 (1983), 1-50.

[9] D W Richerson et al; reference [5], 620-629.

[10] K H Jack; reference [1], 45-60.

[11] R W G Wyckoff; 'Crystal Structures', 2, 2nd edn, Wiley, (1964).

[12] H M Jennings; J. Mat. Sci. 18 (1983), 951-967.

[13] G Schwier; reference [1], 163.

[14] M Mori et al; reference [1], 149.

[15] C Greskovich and S Prochazka; J. Amer. Ceram. Soc. 64 (1981), C96.

[16] M Shimada et al; Amer. Ceram. Soc. Bull. 58 (1979), 519.

[17] S Prochazka and W A Rocco; High Temperature-High Pressure 10 (1978), 87.

[18] G G Deely et al; Powder Met. 8 (1961), 145.

[19] S Wild et al; Special Ceramics 5, ed. P Popper, BCRA, (1972), 385-395.

[20] S Wild et al; ibid, 377-384.

[21] P Drew and M H Lewis; J. Mat. Sci. 9 (1974), 261-269.

[22] J A Mangels and G J Tennenhouse; Amer. Ceram. Soc. Bull. 58 (1979), 834.

[23] M Mitomo et al; J. Mat. Sci. 14 (1979), 2309.

[24] P C Martinego et al; Densification of Oxide and Non-Oxide Ceramics, Conference, Japan (1978), 516.

[25] M H Lewis et al; J. Mat. Sci. 15 (1980), 438-442.

[26] K H Jack; Metals Tech. 9 (1982), 297-301.

[27] M H Lewis et al; Deformation of Ceramics II, Plenum Press (1984), 605-616.

[28] R N Katz; reference [1], 7.

[29] H T Larker; reference [1], 717.

[30] D W Richerson and J M Wimmer; J. Amer. Ceram. Soc. 66 (1983), C173.

[31] Y Oyama and O Kamigaito; J.Appl. Phys. Jpn. 10 (1971), 1637.
[32] K H Jack and W I Wilson; Nature 238 (1972), 28.
[33] M H Lewis et al; J. Mat. Sci. 12 (1977), 61-74.
[34] B S B Karunaratne and M H Lewis; J. Mat. Sci. 15 (1980), 449-462.
[35] B S B Karunaratne and M H Lewis; J. Mat. Sci. 15 (1980), 1781-1789.
[36] G E Gazza; J. Amer. Ceram. Soc. 56 (1973), 662.
[37] N E Cother and P Hodgson; Trans. J. Br. Ceram. Soc. 81 (1982), 141-144.
[38] M H Lewis et al; J. Mat. Sci. 15 (1980), 103-113.
[39] W D Kingery; J. Appl. Phys. 30 (1959), 301.
[40] S Hampshire and K H Jack; Special Ceramics 7, ed. D Taylor and P Popper, BCRA, (1981), 37-48.
[41] R A L Drew et al; ibid, 119.
[42] J R G Evans; J. Mat. Sci. Letts. 2 (1982), 19-21.
[43] E M Levin, C R Robbins and H F M^{c}Murdie 'Phase Diagrams for Ceramists, 1969 Supplement' (NBS), ed. M K Reser, Amer. Ceram. Soc. (1969).
[44] M H Lewis and R J Lumby; Powder Met. 26 (1983), 73-81.
[45] J Weiss and W A Kayser; reference [1], 169-184.
[46] A Szweda and E G Butler; 'The Sintering Behaviour of a Range of Sialon Ceramic Alloys', Amer. Ceram. Soc. fall meeting, August 1982.
[47] R A L Drew et al; reference [1], 323-330.
[48] W H Zachariasen; J. Amer. Chem. Soc. 54 (1932), 3841.
[49] R E Loehman; J. Amer. Ceram. Soc. 62 (1980), 491.
[50] J M Stevels; Handbk. Phys. XIII (1962), 510.
[51] S H Risbud; Phys. and Chem. of Glasses 22 (1981), 168.
[52] K R Shillito et al; J. Amer. Ceram. Soc. 61 (1978), 537.
[53] D R Messier and A Broz; J. Amer. Ceram. Soc. 65 (1982), C123.
[54] P E Jankowski and S H Risbud; J. Amer. Ceram. Soc. 65 (1982), C29.
[55] R E Loehman; J. Amer. Ceram. Soc. 62 (1979), 491.
[56] D Turnbull and M H Cohen; 'Modern Aspects of the Vitreous State', ed. J D Mackenzie, Butterworths, 1 (1960), 38-62.
[57] J W Christian; 'The Theory of Transformations in Metals and Alloys', Pt.1, 2nd ed^{n}, Pergamon Press, (1975).
[58] P W M^{c}Millan; 'Glass Ceramics', 2nd ed^{n}, Academic Press, (1979).
[59] W D Kingery, H K Bowen and D R Uhlmann; 'Introduction to Ceramics', 2nd ed^{n}, Wiley (1976).
[60] M J Ramsey; University of Warwick, unpublished work.
[61] W K Tredway; University of Illinois, private communication to C R Pickering.

[62] R E Loehman; J. Non Cryst. Solids 42 (1980), 433-446.
[63] G Thomas and C Ahn; J. Amer. Ceram. Soc. 65 (1982), C185.
[64] R Raj and F F Lange; Acta. Met. 29 (1981), 1993-2000.
[65] C Ahn and G Thomas; J. Amer. Ceram. Soc. 66 (1983), 14-17.
[66] H Hohnke and T Y Tien; reference [1], 106.
[67] K R Lawless; Rep. Prog. Phys. 37 (1973), 231.
[68] J Desmaison et al; reference [1], 443.
[69] M H Lewis and P Barnard; J. Mat. Sci. 15 (1980), 443-448.
[70] D R Clarke; reference [1], 421-426.
[71] G N Babini et al; J. Mat. Sci. 19 (1984), 1029-1042.
[72] F F Lange et al; J. Amer. Ceram. Soc. 60 (1977), 249.
[73] L J Gauckler et al; J. Amer. Ceram. Soc. 63 (1980), 35-37.
[74] M Billy et al; Ceram. Int. 7 (1981), 13.
[75] G N Babini et al; J. Mat. Sci. 19 (1984), 3487-3497.
[76] J Ito and K Johnson; Amer. Mineral. 53 (1968), 1940-1952.
[77] D R Clarke; J. Amer. Ceram. Soc. 66 (1983), 92.
[78] B Chalmers et al; 'Creep in Structural Ceramics' Prog. in Mats. Sci. 21 (1976).
[79] W R Cannon and T G Langdon; J. Mat. Sci. 18 (1983), 1-50.
[80] F F Lange; J. Mat. Sci. 15 (1980), 601-608.
[81] R Roebuck; J. Mat. Sci. 14 (1979), 2837.
[82] G W Hollenberg et al; J. Amer. Ceram. Soc. 54 (1971), 196-199.
[83] H P Klug and L E Alexander; 'X-ray Diffraction Procedures', Wiley (1954).
[84] P Scherrer; Gotlinger Nachrichten 2 (1918), 98.
[85] D K Bowen and C R Hall; 'Microscopy of Materials', Macmillan, (1975).
[86] O Wells; 'Scanning Electron Microscopy', Wiley, (1974).
[87] J C Russ; 'EXAM methods', EDAX Labs. (1972).
[88] B P Beeston et al; in 'Practical Methods in Electron Microscopy' 1, Pt.2, ed. A M Glauert, North Holland (1972).
[89] R D Leapman; in 'Analytical Electron Microscopy', ed. P L Fejes, Cornell University, Ithaca, New York (1978), 203-219.
[90] C Colliex et al; in Ultramicroscopy 1 (1976), 301.
[91] A Makishima et al; J. Amer. Ceram. Soc. 61 (1978), 247-249, (see also [53]).
[92] H A Bowman and R M Schoonover; J. Res. Nat. Bur. Stand. 71C (1967), 179.
[93] N A Pratten; J. Mat. Sci. 16 (1981), 1737-1747.
[94] J E Schoutens; J. Mat. Sci. 19 (1984), 957-964.

[95] P Land et al; J. Amer. Ceram. Soc. 61 (1978), 56.
[96] O L Krivanek et al; J. Amer. Ceram. Soc. 62 (1979), 586.
[97] S M Winder and M H Lewis; J. Mat. Sci. Letts. 4 (1985), 241-243.
[98] Z-K Huang et al; J. Amer. Ceram. Soc. 66 (1983), C96.
[99] G R Heath; PhD thesis, University of Warwick to be submitted.
[100] K H Jack; reference [1], 'Comments', 110.
[101] A Bouarroudj et al; J. Mat. Sci. 20 (1985) in press.
[102] K H Jack; private communication to M H Lewis.
[103] D R Clarke and G Thomas; J. Amer. Ceram. Soc. 60 (1977), 195.
[104] M H Lewis et al; J. Amer. Ceram. Soc. 62 (1979), 278-288.
[105] H D Keith and F J Padden; J. Appl. Phys. 34 (1963), 2409-2421.
[106] S K Glasstone et al; 'The theory of rate processes', M^{C}Graw-Hill, (1941).
[107] G Hetherington et al; Phys. Chem. Glasses 5 (1964), 130.
[108] B S B Karunaratne; PhD thesis, University of Warwick, (1980).
[109] A Crosby and P E Evans; J. Mat. Sci. 8 (1973), 1573-1580.
[110] M H Lewis et al; 'Mechanisms of creep deformation and fracture in single and two-phase Si-Al-O-N ceramics', Swansea Creep Conference (1981).
[111] E G Butler; Lucas-Cookson Syalon Ltd., private communication.
[112] E M Rabinovich; Phys. and Chem. of Glasses 24 (1983), 54.